

March 27, 1985

INFN PI/AE 85/2

DETECTION OF HEAVY FLAVOURS
AND NEW PARTICLES
AT THE TEVATRON COLLIDER

G. Chiarelli

INFN, SEZIONE DI PISA

University of Pisa Thesis, presented under the
sponsorship of Prof. G. Bellettini

PREMISE

This thesis deals with one of the major problems facing the research at the forthcoming Fermilab antiproton-proton Collider, i.e. the study of hadronic production of heavy flavours and of new and old heavy particles coupled to them. Specifically, an attempt is made to understand the physics merits and the feasibility of tagging heavy flavours by revealing secondary vertices with a micro-vertex silicon detector (SVX) embedded in the core of the central tracking system (CTC) of the Collider Detector at Fermilab (CDF). The microvertex response to a number of physically interesting processes generated with ISAJET was simulated, an analysis strategy was adopted and an appropriate software was written to reconstruct secondary vertices. The results show that this approach can be successful and possibly clear the way to important discoveries. This work, which was done in close collaboration with F. Bedeschi, is described in detail in chapters V and VI which contain the original part of the thesis.

In order to set the stage and to illustrate the importance of the problem, a summary is given in Chapter I of the design of the Tevatron I Collider, and the picture of the basic leptons and hadrons and of their interactions is briefly reviewed in Chapter II, as it stands at present after the historical achievements of the CERN SppS Collider. Since CDF wants to explore the unknown and has great hopes for new discoveries, a discussion is also given of what might be there beyond the Standard Model.

The description of the detector in Chapter III is extremely brief. However the CTC is treated more extensively, in as much as this is useful to understand the performances of the vertex detector. The SVX itself is described in detail. Chapter IV contains a discussion of how well a number of physically important parameters can be measured by CDF: the merits of the SVX should be assessed in this frame. Chapter V describes how the operation of the SVX was simulated and how tracks and secondary vertices were reconstructed. Finally the method is applied in Chapter VI to an analysis of a specific process,

$W \rightarrow tb \rightarrow \text{jet-jet}$ that could be made visible in a jet-jet mass distribution if secondary vertices from the top and beauty decay are tagged. Finally, it is shown that the method could provide a decisive handle to discover the Higgs provided $2 m_{b\bar{b}} < M < 80 \text{ GeV}$.

INDEX

	page	
Chapter I - THE FERMILAB COLLIDER PROJECT (TEV I)	1	
I,1 - THE ANTIPROTON SOURCE	"	2
 Chapter II - COLLIDER PHYSICS	 "	 4
II,1 - TESTING THE STANDARD MODEL	"	5
II,1.1 - HARD PARTON INTERACTIONS	"	5
II,1.2 - INTERMEDIATE VECTOR BOSON	"	7
II,1.3 - THE SEARCH FOR THE TOP QUARK	"	9
II,1.4 - THE SEARCH FOR THE NEUTRAL HIGGS	"	12
II,2 - PHYSICS BEYOND THE STANDARD MODEL	"	15
II,2.1 - GRAND UNIFIED THEORIES	"	16
II,2.2 - COMPOSITE MODELS	"	20
II,2.2.1 - TECHNICOLLOUR	"	20
II,2.2.2 - COMPOSITE QUARKS AND LEPTONS	"	22
II,2.3 - SUPERSYMMETRY	"	23
 Chapter III- CDF	 "	 27
III,1 - CALORIMETRY	"	28
III,1.1 - THE CENTRAL AND THE END WALL HADRON CALORIMETRY	"	29
III,1.2 - ENDPLUGS	"	30
III,1.3 - FORWARD CALORIMETER	"	30
III,2 - MUON SYSTEM	"	30
III,2.1 - FORWARD MUONS	"	31
III,2.2 - CENTRAL MUONS	"	31
III,3 - THE TRACKING SYSTEM	"	31
III,3.1 - CENTRAL TRACKING CHAMBER (CTC)	"	32
III,3.2 - THE VTPC	"	33
III,3.3 - THE FORWARD TRACKING	"	34
III,3.4 - THE CDF SILICON VERTEX DETECTOR	"	34
III,4 - THE TRIGGER	"	39
III,5 - THE SMALL ANGLE SILICON DETECTOR	"	40
 Chapter IV- ESTIMATED DETECTOR PERFORMANCES	 "	 42
IV,1 - ELECTRON IDENTIFICATION	"	43
IV,2 - MUON IDENTIFICATION	"	44
IV,3 - JET DETECTION	"	45
IV,4 - MISSING E_T RESOLUTION	"	46
 Chapter V- THE SILICON VERTEX DETECTOR (SVX)	 "	 47
V,1 - HEAVY FLAVOUR TAGGING AT COLLIDERS	"	48
V,2 - THE CDF VERTEX DETECTOR	"	50
V,2.1 - EVENT FILES AND DETECTOR SIMULATION	"	51

V,2.2	- ANALYSIS	"	51
V,2.3	- SECONDARY VERTEX RECONSTRUCTION	"	54
V,2.4	- DISCUSSION OF THE RESULTS	"	55
V,2.5	- VERTEX FINDING EFFICIENCIES	"	57
Chapter VI	- SHARPENING UP THE $W \rightarrow T+B$ SIGNAL	"	59
VI,1	- VERTEX FINDING EFFICIENCIES	"	60
VI,2	- EXPECTED M_{jj} DISTRIBUTIONS	"	62
VI,3	- SEARCHING FOR THE HIGGS BOSON	"	64
REFERENCES		"	66

CHAPTER I

THE FERMILAB COLLIDER PROJECT (TEV I)

The goal of the Tevatron I project is to provide $p\bar{p}$ collisions at a centre of mass energy of 2 TeV with a luminosity of at least $10^{30} \text{ cm}^{-2} \text{ sec}^{-1}$.

The project requires a) an antiproton source and accumulator, b) an adapted Tevatron to function as a storage ring including a modified lattice to provide low-beta interaction points, c) two experimental areas in the B0 and D0 straight sections, d) a modified main ring to allow \bar{p} injection and to clear the body of the main detectors in B0 and D0. We recall only the structure and main parameters of the source, which determine some basic quality factors of the whole program.

I.1 THE ANTIPROTON SOURCE

The \bar{p} source (I,1) consists of a targetting station and of two separate rings (the Debuncher and the Accumulator) connected to the Main Ring by transfer tunnels (fig. 1). The Debuncher provides a large acceptance for \bar{p} 's produced in the target. After precooling in the Debuncher the antiprotons are transferred to the Accumulator where they are stored and cooled in a similar fashion as in the AA at CERN. The use of two independent rings, one for capturing and one for stacking and cooling the antiprotons, allows a design of each providing optimum performances in its specific role.

The \bar{p} 's are produced by the proton beam extracted from the Main Ring at 120 GeV and hitting a production target, and are accepted by the Debuncher at a momentum of ~ 8 GeV within a large momentum bite $\Delta p/p = \pm 3\%$. On the other hand, the transverse beam size σ and the bunch length τ are minimized to achieve a limited bunch size in phase-space. An upper limit to the flux of protons on target is set by the beam density which locally heats the target itself to the melting point. The operating values are $\sigma = 600 \mu\text{m}$, $\tau = 2$ nsec. This allows to use $2 \cdot 10^{11}$ protons per bunch. In the Debuncher the narrow time spread is turned by phase space rotation into a small momentum spread, $\Delta P/P = .2\%$, which is suitable for \bar{p} stochastic cooling and storage. Fig 2 gives a sketch of the Debuncher and of the Accumulator.

The Accumulator is designed to accumulate and cool a flux

of 10^{10} \bar{p} 's per hour during 12 hours. However, \bar{p} 's can be stored for a longer period if so desired. The cooling is performed (as in the CERN AA) by stochastically cooling the \bar{p} stack. Each new pulse is injected into the tail of an existing stack. Antiprotons in the tail are displaced toward a denser region (the core) where a suitably high density of \bar{p} is reached. The effective triangular shape of the "ring" has been chosen to provide regions of different dispersion where the core and the tail of the stack are cooled separately.

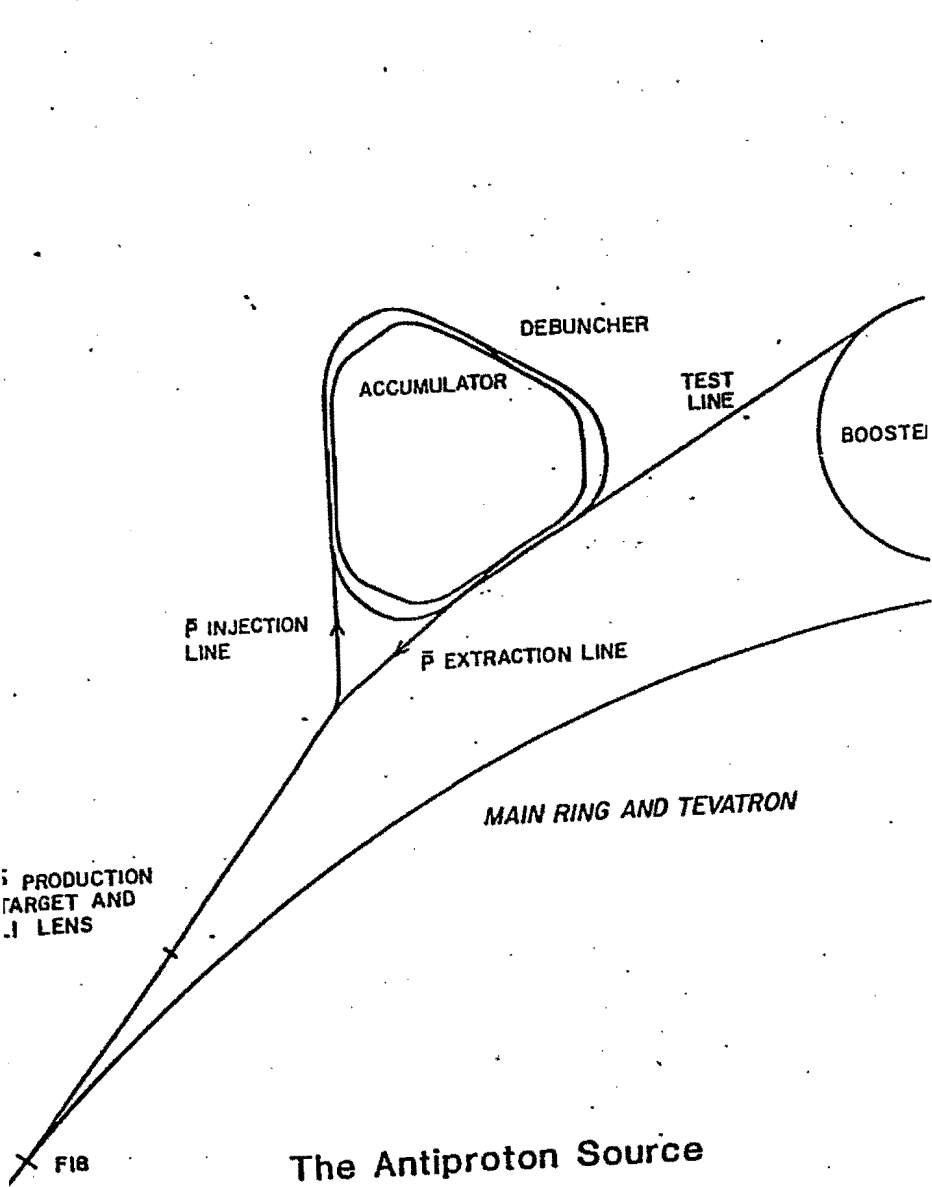
After accumulating and cooling $\sim 5 \cdot 10^{11}$ \bar{p} 's, the Accumulator is ready to feed a beam to the Tevatron. The transfer process begins by moving $\sim 8 \cdot 10^{10}$ \bar{p} 's from the core to the extraction orbit, the bunch is then extracted and injected into the Main Ring. There it is divided into 13 bunches, which are accelerated up to 150 GeV, then again coalesced into a single stack and injected into the Tevatron. The whole cycle can be repeated up to three times to get three bunches of antiprotons. Three opposite bunches of protons are also injected at 150 GeV prior to the \bar{p} 's. The counter-rotating \bar{p} and p bunches are then accelerated to one TeV ($\sqrt{s} = 2$ TeV) and finally the low beta quadrupoles in the interaction region are turned on to squeeze the beams and to reach the desired luminosity. During stable operation this process can be repeated every three hours, if so desired or needed.

The parameters which enter in the luminosity :

$$L = N_p N_{\bar{p}} B f_0 / 4 \pi \sigma^2$$

are N_p ($N_{\bar{p}}$) number of protons (antiprotons) per bunch, B number of bunches, f_0 revolution frequency, σ (gaussian) beam width at the interaction point. The design luminosity of $10^{30} \text{ cm}^{-2} \text{ sec}^{-1}$ is expected to be reached with the following values of the parameters:

$$N_p = N_{\bar{p}} = 6 \cdot 10^{10}, \quad B = 3, \quad f_0 = 48 \text{ Khz}, \quad \sigma = 600 \mu\text{m}.$$



The Antiproton Source
Fig 1

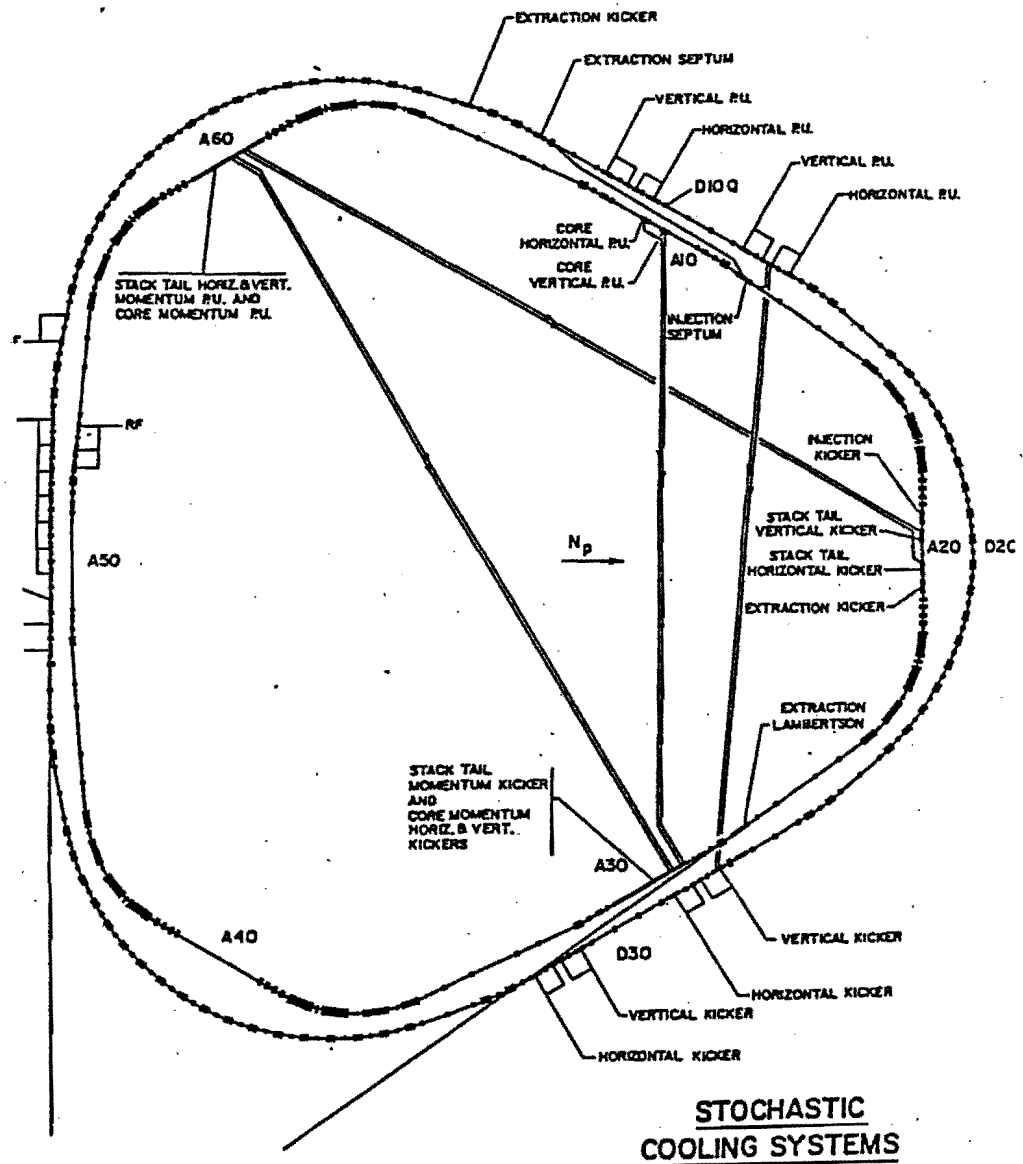


Fig 2

CHAPTER II
COLLIDER PHYSICS

In 1986 the Tevatron Collider will supply $\bar{p}p$ collisions at $\sqrt{s}=2000$ GeV. At the CERN SppS ($\sqrt{s}=546$ GeV in 1983 and $\sqrt{s}=630$ GeV in 1984) the Standard Model of strong and electroweak interactions was tested in the $O(M_W)$ energy region of the interacting partons. What can we expect in the Tevatron energy range, at subenergies $O(300$ GeV)? We divide this discussion into two Sections. First we consider some possible studies to probe the Standard Model deeper. Next we discuss some topics related to what is currently called "Physics beyond the Standard Model".

II.1 TESTING THE STANDARD MODEL

We take the Standard Model to be the following :

- 3 families of elementary quarks and leptons with massless neutrinos,
- $SU(3) \times SU(2) \times U(1)$ gauge theory of strong and Electroweak interactions,
- 1 neutral Higgs Boson.

In part, the research work at the Fermilab Collider can be qualified as a deeper test of the validity of this model. It is natural to distinguish several types of such tests, depending on the specific features of the Standard Model which are addressed.

II.1.1 Hard parton interactions

The dynamics of parton-parton scattering at small distances is well understood in terms of QCD (II,1), the $SU(3)$ part of the Standard Model. Two jet dominance at large P_T has been tested in the first SppS runs at $\sqrt{s}=546$ GeV and one expects this feature to hold even more solidly at 2 TeV. In particular, the QCD predicted growth of the inclusive jet cross-section from $\sqrt{s}=63$ GeV at the ISR to $\sqrt{s}=546$ GeV at the CERN SppS was found to fit qualitatively well the data. This growth is now expected to continue from the SppS to the Fermilab Collider (fig 1).

Given the energy and the luminosity available at FNAL, we expect to be able to measure $d\sigma_j/dp_T$ up to very large transverse momentum, i.e. up to $p_T \lesssim 500$ GeV. This measurement provides an inclusive but direct test of the possible existence of a quark substructure. In the

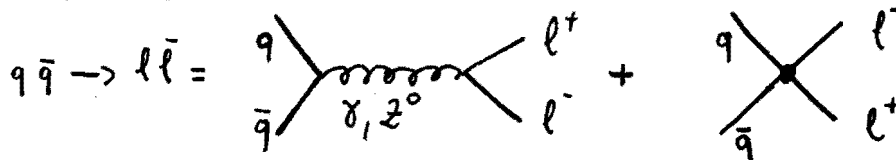
transition region a new parton-parton point interaction would provide a contact term :



as an additional contribution to the QCD amplitudes (II,2). The magnitude of this term would be determined by the compositeness scale Λ_c . Thus a flattening of the jet cross section could be visible at large p_T , if the scale is small enough. By measuring the absence of this flattening one would derive Λ_c , the scale below which the partons appear to be pointlike. An estimate has been made (fig.2) of the limit attainable in large p_T jet studies at Fermilab. Assuming that a deviation from pointlike behaviour would be observable if it corresponds to an increase of rate by about a factor of two over an expected rate of 100 events/year, a scale of 1.5 TeV can be tested at Tevatron I.

The inclusive transverse momentum distribution of single hadrons is understood in terms of perturbative QCD parton-parton interactions plus a non perturbative contribution due to the fragmentation process. One may assume that fragmentation is essentially energy independent, being a scaling function of the relative longitudinal momentum within the jet, x_j , only. Thus the importance of non-perturbative contributions to single hadron at large p_T is expected to decrease with increasing energy and indeed the predicted yield at 90° , at the highest p_T reached at the SppS, fits the experimental data better than at lower energy (fig.3) (II,3). Despite some uncertainties related to the use of different structure functions, these spectra can thus be used to check the Standard Model predictions.

If both leptons and quarks are composite, the contact term will modify also the Drell-Yan cross section (fig 4) which at large lepton-lepton masses is strongly influenced by the Z^0 propagator.



Within the same assumptions on under which conditions the deviation from expectations would be observable, parton compositness can be tested in this process up to $\Lambda_c = 4$ TeV. As far as rates are concerned one should be able to test parton compositness at Tevatron I equally well or even better than at LEP, as indicated by the following table: (II,2)

process	scale limit attainable
$q\bar{q} \rightarrow q\bar{q}$	1.5 Tev
$q\bar{q} \rightarrow e\bar{e}$	4 Tev
$e\bar{e} \rightarrow e\bar{e}$	2 Tev

There are, however, complications at hadron machines from which LEP is free. As far as jets are concerned, the calorimeter energy calibration enters directly at the collider to determine the p_T scale and thus eventually Λ_c . In lepton pair studies, besides the D.Y. mechanism, the pairs can be generated also by other mechanisms which might provide a large physical background. Experience will show how much these limitations will influence the attainable Λ_c limit.

II.1.2 Intermediate Vector Boson

The discovery of W^\pm and Z^0 confirmed one of the fundamental predictions of the Weinberg-Salam model. However there are several other important predictions still to be tested.

The ratio

$$\rho = \frac{M_W^2}{M_Z^2 \cos^2 \theta_W}$$

is predicted to be exactly 1 in the Standard Model. At present the SppS data give $\rho = 0.998 \pm 0.003$ (II,4). This error is determined mainly by statistical uncertainties, given the limited number $O(100)$ of the Z^0, W^\pm collected in each SppS experiment. The IVB detection rate is expected to be ten times faster with CDF and consequently one expects no real limitations from statistics in the future. Indeed the expected cross sections for W^\pm, Z^0 production (II,5), increase by about a factor 5 at Fermilab energy (Tab. 1), and thus CDF will benefit from this growth, as from a higher machine luminosity, to collect a larger sample of IVB's. An

important progress is also to be expected if the W mass can be derived from a peak in the jet-jet mass spectrum rather than from the Jacobian peak in the W decay leptons. There are serious hopes that this will be possible with CDF, as discussed in detail later. It is fair to admit, however, that given the uncertainty in the absolute calibration of the electromagnetic and hadron calorimeters it will not be easy to measure P to better than .1 %.

Both W and Z decay with a very short lifetime ($2 \sim 10^{-23}$ sec) into two jets or two leptons, the hadronic modes being largely preferred. Despite the higher rate, the IVB signal has not yet been seen in hadronic channels, $W \rightarrow q_1 + q_2, Z^0 \rightarrow q\bar{q}$. This is because of the huge background of two jet events generated in parton-parton collisions. Leptonic decays modes provide more stringent signatures. Indeed at the SppS two charged leptons recoiling back to back in azimuth at large P_T provide an extremely clean Z^0 signal. A charged lepton at large P_T and large missing transverse energy (indicated in the following with the symbol : \cancel{P}) -corresponding to the decay neutrino- allowed UA1 and UA2 to discover a fairly clean W signal (II,6). However the identification of the W through its leptonic decay forbids a direct measurement of its mass, because of the unknown longitudinal momentum carried away by the neutrino. While the transverse mass distribution, $M_T^2 = 2 * P_T^e * P_T^{\nu} * (1 - \cos \varphi)$, of the lepton-neutrino system exhibits a jacobian peak at $M_T \sim M_W$, a limit to the sensitivity of this method is set by the fact that only the overall \cancel{P} of the event is measured. This has to be attributed to the neutrino, while being in reality a superposition of several physical and instrumental effects. This introduces a smearing in the peak and limits the accuracy of the result.

The present measures of the IVB masses are (II,7):

$$\begin{aligned} M_W &= 80.9 \pm 3.9 \text{ GeV (UA1); } 83.1 \pm 3.2 \text{ GeV (UA2)} \\ M_Z &= 95.6 \pm 4.4 \text{ GeV (UA1); } 92.7 \pm 3.1 \text{ GeV (UA2)} \end{aligned}$$

The measurement of the Z^0 width is of particular interest as a way to measure the number of existing fermion generations. For $M_Z = 93.8 \text{ GeV}$

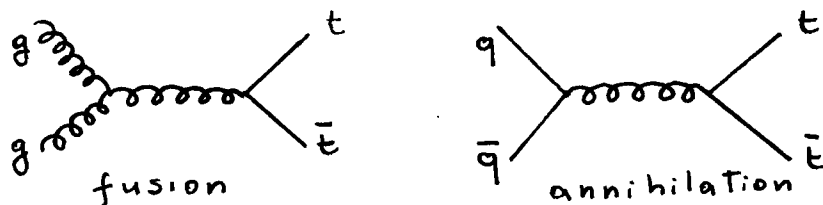
$$\Delta \Gamma_Z = 181 \text{ Mev/type of neutrino.}$$

In practice the mass spectrum of the Z^0 , i.e. the invariant

mass of the decay lepton pair, has a (total) width which is sensitive to the number of generations in as much as the resolution of the apparatus is not too large with respect to the natural width itself. Present UA1 and UA2 data set an upper limit to the number of neutrinos to $N_\nu \lesssim 16$. Again CDF will profit from collecting higher statistics. However, since one would need an accuracy $\Delta M/M = 1-2\%$ in order to get $\Delta N_\nu = .5$, it is likely that the limited calorimeter energy resolution will not allow to improve qualitatively this limit (II,8).

II.1.3 The search for the top quark

Despite of the large physical background of large p_T jets from hard parton scattering, the hadronic decay modes of the W are probably the right place where to look at for a top signal. The top is produced in W decays in association with a b jet. $t\bar{t}$ pairs can also be produced in hard processes which can be calculated perturbatively in QCD, first of all gluon fusion and $\bar{q}q$ annihilation :



The cross section for quark pair annihilation is expected to be 10 nb, which is smaller than for the gluon fusion process. Recently (II,9) the process of gluon fragmentation into two leading heavy flavours was computed perturbatively and found to be even larger than for gluon fusion. This is shown in fig.5.

Higher order QCD processes could be also a copious source of $t\bar{t}$'s. Calculations, however, do not provide more than order of magnitude estimates. The ISR data, indicating a large production of charmed baryons in the forward fragmentation, can be used together with simple scaling arguments to predict large cross section also for $t\bar{t}$ at Tevatron I. Detailed QCD calculations were performed for charm production in hard processes, giving a reasonable agreement with the data at large angles (II,10). However such an agreement between perturbative calculations and large angle

data may look fortuitous since the limited Q^2 region of the ISR makes the application of perturbative QCD not very safe, and moreover not well known parameters (structure functions and fragmentation functions) introduce further uncertainties.

In this situation, one cannot safely predict forward production of heavy flavours at the Tevatron. Lower order QCD calculations should be adequate at large angles and can thus be considered to provide a lower estimate of total heavy quark production. As far as topped mesons in the central region are concerned, production should be correctly estimated by perturbative QCD. The diagram computed by Kane (II,9) should allow to extend these predictions to intermediate transverse momenta. Inclusive top searches may be possible but cannot be looked at with great optimism. If the mass of the top is not too large, then $W \rightarrow tb$ decay has a B.R. which is ~ 2 times the B.R. of $W \rightarrow e\nu$:

$$R = \frac{\Gamma(W \rightarrow tb)}{\Gamma(W \rightarrow e\nu)} = 3 * (1-x) * (1-x/2-x^2/2), \quad x = M_t^2 / M_W^2 :$$

M_t (GeV)	R
30	2.4
40	2.0
50	1.4
60	.9

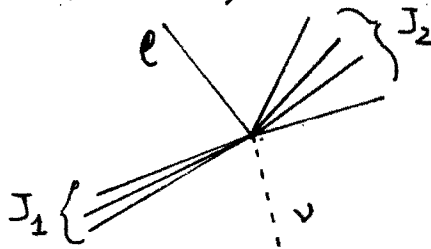
At the Tevatron Collider, this means $\sigma(W \rightarrow tb) \sim 4-6$ nb. Although the top quark fragments in an essentially unknown way, we can still make some general statements on the topology of topped jets. Because of the large quark mass the fragmented hadrons will have relatively large opening angles, giving in the calorimeters a wider pattern than for "light" jets. We recall that for the decay of a body of mass m (II,10)

$$\sum_i |p_T^i| \approx \frac{\pi}{4} m,$$

where the transverse momentum components of all final prongs are added. Assuming the jet multiplicity to be determined by the fragmentation process, and thus for any jet momentum to be independent of the primary quark mass, this mass determines the average opening angle of the jet. Although at very high jet momenta and multiplicity the fragmentation process will eventually mask the primary mass signature

(e.g. at $n=40$ which is the typical multiplicity of a 200 GeV jet one has even for a light jet, $\sum |P_i'| \approx 30$ GeV), in the jet energy range $p \approx 200$ GeV an appreciable difference may be expected, for instance, between the width of t and b jets. Because of its weak and not clear-cut signature this effect has not been used up to now as a tag for top quark. Still it might turn out to be useful in the future in association with other cuts.

The case of a few body decay of the heavy flavour at the parton level is more favourable. In the semileptonic decay of top, $t \rightarrow b l \nu$, the lepton carries a large momentum with a large component transverse to the axis of the associated b jet, in presence of a large missing P_T of the overall event. The average parton separation is much larger than the width of the secondary jet, and this is the base of the idea of looking for an isolated lepton as a tag for top decay (II,11). In the calorimeters one expects the characteristic signal of a lepton (muon or electron) without hadronic fragments nearby. In the transverse plane the expected picture for $W \rightarrow tb$ followed by $t \rightarrow b l \nu$ decay is as follows:



with a well isolated lepton and a "large" and a "small" jet (this was the topology of the events which were exploited by UA1). This effect is qualitatively much smaller in b and c decays, where the low mass limits the mean opening angle of the lepton relative to the jet such that in general the lepton is surrounded by hadronic fragments. In b decays the invariant mass of the lepton-jet system is constrained to be:

$$m^2(e, j) \lesssim m_b^2 - m_c^2$$

$$\sin^2\left(\frac{\theta}{2}\right) \lesssim \frac{m_b^2}{4 p_e p_j}$$

giving for $P_J \sim 10$ GeV, $P_e \sim 20$ GeV $\rightarrow \theta \lesssim 20^\circ$

We thus summarize the significant signatures of the $W \rightarrow t b$ ($t \rightarrow l \nu$) decay as follows:

- a) the transverse momentum of the recoiling jet will have a jacobian peak at $P_T = M_W/2(1-x)$, where $x = M_t^2/M_W^2$,
- b) the event will contain two jets, the more energetic one being in general the primary b-jet from W decay,
- c) large missing P_T ,
- d) a large P_T lepton without nearby hadrons.

The presence of the neutrino in this channel prevents a direct reconstruction of the top mass, but the, "cluster mass", M_c :

$$M_c^2(J_2, e, \nu) = \left\{ \sqrt{|P_{T,e}|^2 + m_e^2} + |P_{T,\nu}| \right\} - \left(\vec{P}_{T,e} + \vec{P}_{T,\nu} \right)^2$$

peaks at $\sim M_t$ (fig 6), and can be used to measure the top mass. Of course in these events one should also have (II,12):

$$M_c(J_1, J_2, e, \nu) \lesssim M_W$$

which is the cluster mass of the W.

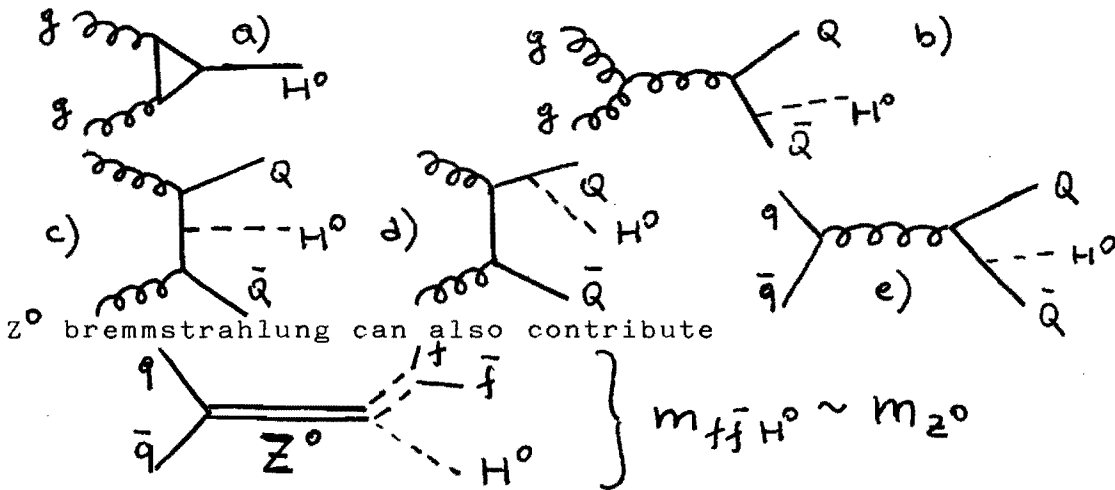
UA1 performed an analysis (II,13) based on the considerations given above and reported the evidence of six candidates (as of 1984) for top production in $W \rightarrow tb$ decay followed by semileptonic t-decay. An indication for the top mass of $30 \lesssim M_t \lesssim 50$ GeV was obtained.

II.1.4 The search for the neutral Higgs

In the Weinberg Salam model, the Higgs boson plays the double role of breaking the symmetry and of giving mass to the fermions through Yukawa coupling. The Higgs is a most elusive particle. Theoretical estimates are loose and do not predict its mass, which is essentially a free parameter of the theory. A lower bound is set by the condition of vacuum stability, and an upper bound by the request of perturbative unitarity (II,14):

$$10 \text{ GeV} \lesssim M_H \lesssim 1 \text{ TeV}$$

The production of Higgs boson at the Tevatron Collider is estimated by computing the following diagrams:



The cross section for process a) is (II,15):

$$\frac{d\sigma}{dy} = \sigma_0 |I|^2 \mathcal{Z} * G(x_1) * G(x_2)$$

$\mathcal{Z} = M_H^2 / s$, x_1, x_2 momentum fractions carried by gluons,

$$\sigma_0 = \frac{G_F \pi}{288\sqrt{2}} \left| \frac{\alpha_s(m_H/2)}{\pi} \right|^2$$

The I factor results from the loop integral and is sensitive to the value of M (fig.7). In practice one takes $I \approx 1$, since the gluon structure function $G(x)$, which enters to the second power in the formula, is already uncertain to a factor of two. For $10 \text{ GeV} \lesssim M_H \lesssim 90 \text{ GeV}$, the cross section is $O(100 \text{ pb})$.

Higgs production and decay is expected to be signalled by two back to back jets, since Higgs particles predominantly decay into the heaviest fermion pair kinematically allowed (fig.8)

$$\Gamma(H_0 \rightarrow f\bar{f}) = \frac{G_F}{4\sqrt{2}\pi} m_f^2 m_H \left(1 - 4 \frac{m_f^2}{m_H^2}\right)^{3/2} \cdot C$$

where C is a colour factor ($C=1$ for leptons, 3 for quarks) If $M_H \gtrsim 2 M_b$ the decay is predominantly into a $b\bar{b}$ pair. One understands that a search for a Higgs signal as a peak in the jet-jet invariant mass spectrum can be facilitated if one has at one's disposal a means to tag beauty jets. This can be provided by secondary vertices in the event, as discussed in detail later.

The production channel ($gg \rightarrow H^0 + X$) was studied also in relation to possible existence of superheavy Higgs particles with $M_H \gtrsim 2 M_W$. The results are not encouraging since signals of one pb or less are expected. This is too low given the Tevatron luminosity at its start, despite of the clean topology of the Higgs decaying into a W pair. There are, however, ambitious plans to increase the Tevatron luminosity. The estimated production cross-section as a function of the Higgs mass (II,16) are as follows :

M_H (GeV)	σ (pb)
200	1.5
300	0.476
400	0.183

The rates for processes b) to e) have also been computed (II,17). The dominant production and decay channels produce four jets in the final state : $pp \rightarrow Q\bar{Q} + H^0, H^0 \rightarrow Q\bar{Q}$. Although some times jets will overlap with each other, the four jets should in general provide a useful event signature. The estimated cross-sections are not small (for example $\sigma = 0(100 \text{ pb})$ for $M_H \sim 20 \text{ GeV}$) (fig.9). The Higgs would predominantly be produced in association with t quarks if $M_t \sim 40 \text{ GeV}$ (the Yukawa coupling enhances this mode despite the unfavourable kinematical factors) or with b quarks (for which the same factors combine, although with different values, to produce a similar cross-section, see fig 10).

Depending on the decay channel, a number of distinct experimental signatures will be available. In a first approach multi jet events will have to be studied. Next, heavy flavour tagging through secondary vertices can be used to improve the signal/background ratio. This can also be done by selecting events in which one (or more) of the quarks decays semileptonically with a lepton at large P. This would, however, lower considerably the signal and also introduce a spread in the relevant jj mass spectrum.

Process e) in which the Higgs is produced by bremsstrahlung of a real Z has an excellent signature. The branching ratio

$R = \Gamma(Z^0 \rightarrow H^0 \mu^+ \mu^-) / \Gamma(Z^0 \rightarrow \mu^+ \mu^-)$ is quite small (II,18, fig.11). For $M_H \lesssim 40 \text{ GeV}$, $R \sim 10^{-3}$ (here we deal with Z^0 on mass shell only). At $\sqrt{s} = 2000 \text{ GeV}$ this gives a total cross section for H^0 production of about 10-30 pb for M_H below 30 GeV. Despite of its smallness this could be a promising

channel, provided that the Higgs boson and the leptons are produced at large P_T , thus favouring detection and discrimination against background. Distinctive signatures of this process would be two large P_T leptons with $m_{\ell\ell}^2 \lesssim M_Z^2$ and two b jets with $M_{jj} = M_H^2$. Again b jets can be tagged by the existence of secondary vertices. This can be a clean signature to disentangle these events from the background of standard QCD scattering and gluon bremsstrahlung. Finally, being the Z on the mass-shell, the overall invariant mass of the jets and the decay leptons altogether is smaller than M_Z .

II.2 PHYSICS BEYOND THE STANDARD MODEL

The Standard Model is in a very good shape. The Z^0 and W^{\pm} have been discovered and also a possible signal of the top has been found. The only missing particle is the Higgs boson, which after all could be discovered in a near future since characteristic signatures are expected from its decay. Still, an intense theoretical work is going on on more general theories. The reason for this is twofold. First the SM has a number of defects that bring most theorists to exclude that it might be the ultimate model. Second, a number of unusual events were reported from the CERN Collider experiments after the 1983 run which seemed to indicate the need for a new phenomenology that could not be accommodated within the SM.

There are three non trivial theoretical problems which are not solved within the SM (II,20):

- a) there are too many free parameters, (i.e. the 17 values of the masses), and this makes the theory ugly,
- b) the Strong and Electroweak interactions are not really unified, their couplings being uncorrelated,
- c) the cancellation of diagrams which destroy the gap between Λ_F (Fermi scale) and Λ_P (Planck scale) is obtained by the fine tuning of several parameters in a very unnatural way.

The new theories try to avoid with a different degree of easiness and success one or more of these defects.

Out of the several indication for new phenomena in the 1983 CERN Collider data (II,21) we will mention the

following ones:

- a) the existence of events with a single (or a few) large P_T jet whose transverse momentum is not balanced by visible particles ("monojets"),
- b) the existence of a few events in which a lepton pair was accompanied by a hard photon, the total mass being the Z^0 mass ("Zen" events e.g. $Z^0 \rightarrow e^+ e^- \gamma$),
- c) the possible existence of a bump in the effective mass of the jet-jet system, at $M_{jj}=160$ GeV.

These various hints, as well as similar ones that it would not be appropriate to discuss at this point, triggered an intensive interpretation work in the frame of various theoretical models. The 1984 Collider data (II,22) do not confirm most of these hints, and therefore it does not seem it to be advisable to base a discussion of the theories beyond the SM on their ability to interpret the above mentioned phenomenology. At the present time, this phenomenology should be rather taken as a useful exercise for learning how these theories could be connected to specific new effects. On the other hand a discussion of the main lines of the new theories is still of interest both as a means to understand high energy phenomena in a deeper and more satisfactory way, and as a preparatory work to guess in advance which new phenomena could be expected at the Fermilab Collider. It should also be considered that some out of the many hints mentioned above might eventually turn out to be firmly established.

We therefore discuss briefly in the following the main lines of three types of new models that have been more extensively considered in the literature :

- Grand Unified Theories (GUT),
- Composite Models,
- Supersymmetric Theories (SUSY).

II.2.1 Grand Unified Theories

In these theories the strength of the strong and electroweak interactions become comparable and the two interactions merge into a unified one at an extremely high energy scale $O(10^{15})$ GeV). Therefore there is no obvious direct contact between these theories and present collider experiments. Earthly windows for GUTS are rather the proton

decay and the existence of magnetic monopoles. Although they are far from the unification energy scale, collider experiments can still tell something important about what has to be unified, since they are in an excellent position to discover whether there are more than three generations of quarks and leptons. This is also a specific type of physics that can be addressed with a detailed study of the vertex structure of the events, as discussed in Chapters V and VI.

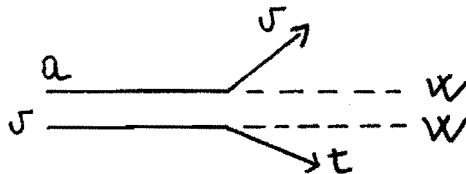
As in the Standard Model, in the GUT's the number of fundamental fermions is an input parameter.

A new sequential heavy lepton heavier than the τ as well as a new heavy quark heavier than the b , are ruled out by the PETRA experiments for $m \leq 23.8$ GeV (II,23). The existing data on the Z^0 width put a very weak constraint on the number of neutrinos, $N_\nu \leq 16$. Elaborations of the UA1 and UA2 data, which exploit the ratio $\sigma(Z)/\sigma(W)$ and get an indication for $N_\nu \leq 3,4$ (II,24) are largely uncertain because of the poor statistics and of systematic uncertainties in the data. We therefore consider the problem of the existence of one or more new generations as an open one, both experimentally and theoretically.

In $\bar{p}p$ collisions, superheavy quarks are produced through the same mechanisms already discussed for the top, i.e. gluon and quark fusion. QCD calculations at 2 TeV show that up to masses of 100 GeV the signal can be as large as about 100 pb. This is shown for two different choices of the structure functions in fig.12.

Given the well known quasi-diagonal structure of the Kobayashi-Maskawa matrix (II,25); one expects the heavy quarks (a, v) of a fourth generation to decay predominantly as :

- 1) $a \rightarrow v + W$
- 2) $v \rightarrow t + W$



where the W can be either real or virtual, depending on the masses. Their fragmentation is expected to proceed via the production of a meson carrying the new flavour, or a slightly degraded one, within a jet of increased transverse

mass and multiplicity. These properties can therefore be exploited as experimental signatures to tag the production process of the new flavour (II,26).

It is interesting to observe that if the new quark has enough available phase space, it can decay into a real W. This would provide a very clean signature for such an event. On the other hand if the 3rd and the 4th generations overlap with $m_{\nu} < m_c$, the dominant ν decay would be $\nu \rightarrow W+c$. This would open up the interesting possibility of such a long ν -lifetime that its decay point would be detectable as a secondary vertex in the detector (fig 13).

As usual, ν decay would proceed through the hadronic channels $\nu \rightarrow q_1 \bar{q}_2 c$ or the semileptonic channels $\nu \rightarrow l \nu c$. The semileptonic channel would provide an important signature through a large P_T lepton, with a tail in the P_T distribution reflecting the mass of the primary quarks (fig 14). On the other hand the B.R. for a specific lepton channel is $\sim 10\%$, no matter whether the W is real or not. In practice one will have to exploit both the hadronic and leptonic channels, the weaker hadronic signature being possibly compensated by an increased statistical significance.

A number of strategies can be adopted in order to tag heavy quark decays into hadronic channels. One of them, the search for secondary vertices associated to heavy flavour decays, was already mentioned several times and will be discussed in more detail later. Other topological signatures are the existence of a lepton at a relatively large angle with respect to the jet axis (in the case of the semileptonic decay) and a broad jet aperture, a parameter sensitive to the mass of the primary quark. This is so both in the case of a decay through virtual or real W. With reference to the case of a real W, another signature is given by the jet-jet invariant mass which is constrained to M_{W} .

In the framework of theories which cancel the ABJ anomalies, the generations of quarks and leptons are interrelated, and one expects a lepton doublet (II,27) to accompany a quark one.

The cross section for L production at a 2 TeV pp Collider was calculated through the processes $W \rightarrow L \nu_L, Z^0 \rightarrow L \bar{L}$

including contributions from real as well as from virtual IVB's (fig 15) (II,28). Since the production rate via the Z^0 channel turns out to be much smaller than via the W^* channel, we will discuss only processes channelling through a charged IVB.

Because of the non negligible mass of the lepton relatively to the W, the angular distribution relative to the W direction is not expected to show an appreciable asymmetry. With reference to W^+ decay one has:

$$\frac{d\sigma}{d\Omega} \propto (1 + \beta_L \cos \hat{\theta}) (1 + \cos \hat{\theta}) \quad \beta_L = p_L / E_L$$

For $M_L^2 / M_W^2 \ll 1$, $\beta_L \rightarrow 1$ and the l is produced in states of positive helicity. However, being negative helicities suppressed to the order M_L^2 / M_W^2 , this suppression does not hold for the superlepton. This shows that the characteristic backward charge asymmetry of the $W \rightarrow l \nu$ decay is quickly lost as soon as $\beta \ll 1$. The convolution over the W production momentum and decay into a stable lepton introduce additional smearing, with eventually a net loss of signature for the event. We mention, however, the confident approach of UA1, who observes that after all the absence of a signature can be taken as a positive signature (II,29).

Suppose that one takes as a goal to detect the L through its leptonic decay into a muon. The dominant source of background are likely to be the more direct decays $W \rightarrow \mu \nu$ and $W \rightarrow \tau \nu$, followed by $\tau \rightarrow \mu \nu \nu$ (II,30). Fig.16 shows the angular distribution of the muons from these two processes as a function of P_T . In as far as this distribution is not uniform, a charge asymmetry will be generated in a given bin of P_T at a given laboratory angle. If a superlepton L is also produced, the muon angular distribution of fig 16 would have to include also the contribution from $L \rightarrow \mu \nu \nu$, with a much smaller additional rate (because of phase-space factors) than that already included in the figure and with an essentially uniform angular distribution. The empirical measurable charge

asymmetry would be therefore further reduced, and this might be taken as an indication of the existence of the L lepton.

There might be a better chance of finding L by exploiting the hadronic decays $L \rightarrow q_1 q_2 \nu$ (II,30), since:

$$R = \frac{\Gamma(L \rightarrow q_2 q_1 \nu)}{\Gamma(L \rightarrow \mu \nu)} \approx 3.$$

The primary neutrino produces a missing P_T signal larger than in semileptonic decays. A cut of \cancel{P} larger than 25 GeV can therefore be applied (fig 17) to discriminate against this background. The two quarks have sizeable momenta, the relative opening angle between the two quarks increases with the mass of the superlepton (fig 18), and this is an additional means which can be usefully exploited. (II,31) \cancel{C} hadronic decays will still be a dangerous source of background for those events (~ 20 % of the total) in which the W production is accompanied by a gluon jet with $P_T \gtrsim 10$ GeV. However it should be possible to eliminate most of these events by suitable cuts, since the \cancel{C} jet has a very low charged multiplicity.

II.2.2 Composite Models

Within this definition, several new theories which extend the SM are grouped. Their common feature is the prediction of compositeness for some of the fundamental fields which appear in the Weinberg-Salam theory. With an increasing distance from orthodoxy, composite Higgs, composite quarks and leptons, and composite gauge bosons have been considered (II,32).

II.2.2.1 Technicolour

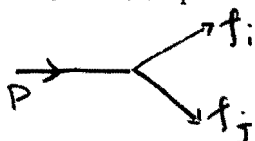
The basic idea of TC is related to the criticism of the Higgs sector of the SM. Actually the Higgs particle plays two uncorrelated roles: it is one of the actors of the spontaneous breaking of symmetry (SBS) and it gives masses to all fermions through Yukawa couplings. A different approach is suggested by another manifestation of spontaneous breaking of symmetry, the superconducting phase transition. In BCS (Barden, Cooper, Schrieffer) theory of the superconducting phase transition, the dynamical origin of

the order parameter is identified with the creation of a pair of electrons (Cooper pairs) as bound state. In a similar way TC as developed by Weinberg and Susskind (II,33), and Farhi and Susskind (II,34) is a theory in which the breaking of symmetry has dynamical origin, and mimicks QCD for the dynamics. An $SU(N) \times SU(3) \times SU(2) \times U(1)$ model is adopted which includes a new T_C interaction and a zoo of new "techniparticles".

In the minimal TC scheme, massless technipions appear and technifermions are coupled to gauge bosons by the conventional electroweak interaction. Their charge is semi-integer and if one chooses $F_P = (G_F \sqrt{2})^{-1/2}$, where F_P is the technipion (P) decay constant, then M_W and M_Z are left unchanged, as well as their ratio (II,35).

Despite of its elegance, minimal TC cannot be the true theory because it does not account the generation of lepton masses. Extended technicolor addresses this problems, but in this attempt the theory becomes extremely complicated. As of today it is not understood if these troubles are intrinsic in the model or not (II,36).

Several predictions -existence of bound states, a technizoo in the 200 GeV - 1 TeV mass range- are proper to any TC models, from the minimal TC to the most intrigued version of it. Technipions are colour singlets with estimated masses $8 \lesssim M_P \lesssim 40$ GeV; moreover colour triplet, octet, technirho, technieta, leptoquarks should exist. The width of TC particles is easily evaluated, provided that their couplings to fermions is known:



$$\Gamma(P \rightarrow f_i f_j) \approx \frac{G_F P}{16\pi} (M_i^2 + M_j^2) \cdot C$$

where G_F is the Fermi constant, p is the momentum of the products in the technipion rest frame, and C is a colour factor ($C=3$ for the decay of a singlet into quarks and 1 otherwise) (II,37).

Techniparticles decay predominantly into the heaviest fermions (fig 19), for example:

- $P^+ \rightarrow \bar{t}b, \bar{c}b, \bar{c}s,$
- $P^0 \rightarrow \bar{b}\bar{b}, \bar{c}\bar{c}, \bar{\nu}\bar{\nu}$
- $P_8^0 \rightarrow t\bar{t}$
- $P_3 \rightarrow t\bar{\nu}, t\nu, b\bar{\nu}$

Where P_3 is a leptoquarks, P_8^0 is the technieta, P^+ and P^0 are a charged and a neutral techipion. Thus search for techniparticles is naturally associated to tagging of heavy flavours. Events in which a pair of TC particles is produced, give in general four heavy quarks in the final state. Cross sections are sizeable. For example (fig.20) $d\sigma/dy (p\bar{p} \rightarrow P^0 + X) \approx 80$ pb for $M_{P^0} \approx 60$ GeV. Technieta production is expected to occur with $\sigma \gtrsim 10$ pb for mass below 160 GeV, and technieta decay into heavy quarks gives a unique signature against background (fig 21) (II,38). In conclusion some of the prediction of TC should be testable at the Tevatron Collider, since our detector has a good jet recognition, a good resolution on jet-jet invariant mass and finally since tagging of heavy flavours can be done with a good efficiency (as discussed later).

II.2.2.2 Composite Quarks and Leptons

The proliferation of quarks and leptons has generated the speculation that they may be composite structures, bound states of more fundamental constituents -the preons - which interact via a new strong gauge force. Like quarks in QCD, preons would be asymptotically free and infrared confined. If a compositeness scale, Λ , exists, at present experimental limit is (II,39) :

$$\Lambda \gtrsim 1 \text{ TeV.}$$

This bound comes essentially from the measurement of the $g-2$ of the muon and from the absence of deviations from QED in Bhabha scattering. A similar bound exists for the quark sector.

Preon models were considered in very recent times in order to explain the $Z^0 \rightarrow e^+ e^- \gamma$ events which occurred with a surprisingly large rate during the 1983 collider run. Several models were proposed to account for these events, like the existence of an excited Z^0 and the radiative decay of the Z^0 into a scalar neutral boson or into an excited lepton (II,40). This latter possibility -existence of composite fermions- was qualitatively compatible with the topologies of other exotic events (e.g. single χ and \cancel{E} , that could have been due to $Z^0 \rightarrow \nu^* \nu \rightarrow \nu \nu \gamma$) and with possible bumps in M_{jj} . If an excited quark q^* exists, then $q \rightarrow qg$ predominantly and q^*

could be seen as a bump in M_{jj} . If $M_{q^*} > M_W$ then a signal in the W -jet invariant mass could show up. Furthermore if $M_{q^*} > M_Z$, the Z^0 decay into a neutrino pair would originate events with one jet and $\bar{\nu}$ (II,41).

This interpretation of the exotic events (at least of those which did not vanish into statistical fluctuations) is not ruled out, although it now appears that the events can be explained by conventional non-exotic mechanisms, like photon bremsstrahlung (Zen events) or gluon bremsstrahlung in Z events (monojets). If exotic events are there and are still confused with background at $S\bar{p}pS$ energies, they might stand up and be firmly established at the energy of Tevatron I.

Probably in CDF the most compelling signature for excited fermions (II,42) will be provided by events involving an IVB or be given by bumps in the jet-jet invariant mass distribution. In Section I of this Chapter we discussed the behaviour of the inclusive jet yield at large P_T as a possible signal for quark compositeness. It is obvious that while this kind of small effect in an inclusive distribution, even with large statistics could provide a rather indirect evidence, a peak in the M_{jj} distribution would be a much less questionable signal.

II.2.3 Supersymmetry

SUSY is a theory (or rather a set of models) in which a symmetry links fermions and bosons, predicting that for each known fermion and boson its bosonic and fermionic SUSY partner should exist. The theoretical interest for SUSY is born out of several of its features which are nice. We recall here two of them: a) several SUSY models are unified theories in which gravitation is included, b) SUSY is able to solve the "hierarchy problem" in a very elegant way. As mentioned before the difference of about 11 orders of magnitude between Λ_F and Λ_P needs cancellation of several diagrams in order to be accommodated. In standard GUT's this is obtained ad hoc by the fine tuning of several parameters. This unnatural way is bypassed by SUSY in which cancellation is exact at all orders by the introduction for each particle of its supersymmetric partner. One appealing feature of SUSY is the symmetry

between the fermionic and the bosonic world, which are strongly correlated with each other (II,43).

The masses of SUSY particles are degenerate with their ordinary partners if SUSY remains unbroken. Mass differences depend on the mechanism of symmetry breaking, and are thus essentially unknown, although a number of limits can be set because of the non-existence of some low energy processes.

The attempts to explain with SUSY the collider exotic events left us with the lesson that more or less all SUSY models can predict new particles below 1 TeV. This apparently implies that in a few years several experiments, including CDF, should be able to give to SUSY models some important pieces of information.

In the SUSY world a new quantum number, R, is conserved. R is 0 for standard particles and +1 for SUSY ones (II,44). Because of R conservation all SUSY particles will eventually decay into the lightest of all of them, which must be stable and weak interacting. This particle is normally taken to be the photino, $\tilde{\gamma}$. The $\tilde{\gamma}$ would leave any detector without interacting and cause a momentum unbalance in the final state whose transverse component may be measurable by the overall P in full analogy with the neutrino case. Whether the gluino, \tilde{g} , is lighter than the squark \tilde{q} cannot be determined by the theory. For our discussion we assume the gluino to be lighter than the \tilde{q} . Thus \tilde{g} would predominantly decay into $q\bar{q}\tilde{\gamma}$ and \tilde{q} into $q\tilde{g}$ or $q\tilde{\gamma}$. The sleptons \tilde{l} would decay into $l\tilde{\gamma}$.

The signature of missing energy (carried away by neutrinos) is common to all events involving the semileptonic decay of heavy quarks. Indeed, this is an important signature when searching for new heavy quarks. In the search for SUSY particles, heavy flavour events would act in general as serious sources of background (II,44) (Tab.2).

Although LEP is probably an ideal place to look for SUSY processes, $\bar{p}p$ colliders are competitive. This is due to the large available energy range that allows for instance to search for SUSY particles in the decay of charged vector bosons. In fig.22 we show the cross section for gluino pairs production at Tevatron I. Two processes are likely to be best studied (II,45):

- a) $\bar{p}p \rightarrow \tilde{g}\tilde{g} \rightarrow 4 \text{ jet} + \cancel{E}$
- b) $\bar{p}p \rightarrow \tilde{q}\tilde{q} \rightarrow \bar{q}q\tilde{\gamma}\tilde{\gamma}$ b.1
- $\rightarrow qq\tilde{\gamma}\tilde{\gamma}$ b.2

Process a) has two hard jets in the final state and in general no prompt lepton and some missing P_T . Obvious source of background is the semileptonic decay of heavy quarks in which the lepton is missed. An accurate measurement of \cancel{E} and a very good recognition of leptons close or inside a jet would be useful, still the lack of distinctive signature of the event is a serious problem.

Similar considerations for signatures and backgrounds hold for processes b.1) and b.2). Actually these processes seem to have an even smaller chance to be detected. Process b.1) has a very small cross section and b.2) has a rather confused final state with several jets and \cancel{E} . In an effort to explain the Collider monojets, it was argued that three of out of the four final state jets would often be very weak and escape detection (II,46). In this case monojets would be observed. For these events a possible source of background are the $W \rightarrow Z + \nu$ events in which a gluon bremsstrahlung jet with $P_T > 10$ GeV is also produced and observed as a monojet, since it is relatively easy for the hadrons from Z decay not to give a sizeable jet. Similarly $Z^0 + g$ with $Z^0 \rightarrow \nu\bar{\nu}$ would be a dangerous background.

Gauginos ($\tilde{W}, \tilde{H}^0, \tilde{Z}^0$) can be produced in the decay of standard IVB if masses allow (II,47):

$$\begin{aligned}
 W^\pm &\rightarrow \tilde{W}^\pm + \tilde{Z}^0 \\
 &\rightarrow \tilde{W}^\pm + \tilde{\gamma} \\
 &\rightarrow \tilde{W}^\pm + H^0
 \end{aligned}$$

In these processes several final states are possible, depending on which fermion is produced in association with the W^\pm , and on the various SUSY decay channels. Background would come primarily from $W+g$ events, with $W \rightarrow l + \nu$ and the lepton escaping detection. In tab 3 we compare signatures and backgrounds for various SUSY processes.

As a final comment on the chance of observing SUSY particles we observe that the following detection features will be important:

- a) good jet recognition and reconstruction,

- b) good missing P_T resolution,
- c) good lepton identification,
- d) reconstruction of secondary vertices.

Even allowing that CDF will be excellent from all these points of view, the above considerations force us to conclude that life will be hard for the SUSY searchers (II,48)

Tab.1

cross sections for W^+ and Z^0

(in nb)

\sqrt{S} (GeV)	$\sigma(W)$	$\sigma(W \rightarrow e\nu)$	$\sigma(Z^0)$	$\sigma(Z^0 \rightarrow e^+e^-)$
540	$4.2^{+1.3}_{-0.6}$.374	$1.3^{+.4}_{-.2}$.042
2000	$20.0^{+6.}_{-4.}$	1.78	$6.2^{+1.9}_{-1.2}$.198
10000	$130.^{+70}_{-55}$	11.6	$46.^{+24}_{-20}$	1.47

$M_W = 83$ GeV

$M_Z = 94$ GeV

Overview of possible SUSY signature in $p\bar{p}$ collisions

SUSY process	Signature
$p\bar{p} \rightarrow \tilde{g}\tilde{g}$	$(q\bar{q}\tilde{\gamma})$ on each side; so very small p_T imbalance and (1 broad jet or 2 jets) on each side
$p\bar{p} \rightarrow \tilde{g}\tilde{\gamma}$	Large missing energy and (1 broad jet or 2 jets: $\tilde{g} \rightarrow q\bar{q}\tilde{\gamma}$) on the other side
$p\bar{p} \rightarrow \tilde{q}\tilde{q}$	$(q\tilde{g} = qq_1\tilde{q}_2\tilde{\gamma}, \text{ or } q\tilde{\gamma})$ on each side so: a small p_T imbalance and (1 "broad" jet = 3 jets, or 1 jet) on each side
$p\bar{p} \rightarrow \tilde{q}\tilde{\gamma}$	$(q\tilde{g}\tilde{\gamma} = qq_1\tilde{q}_2\tilde{\gamma}\tilde{\gamma} \text{ or } q\tilde{\gamma}\tilde{\gamma})$ so (some p_T imbalance and a jet) or a good p_T imbalance and a "broad" jet ~ 3 jets
$p\bar{p} \rightarrow W^\pm \rightarrow \tilde{e}\tilde{\nu}$	$= (e\tilde{\gamma}, \nu\tilde{\gamma})$ or $(e\tilde{\gamma}, \nu\ell^+\ell^-\tilde{\gamma})$ or $(e\tilde{\gamma}, q\bar{q}\tilde{\gamma})$, so a large missing energy on one side and an energetic lepton on the other side (e^\pm produced would be SYMMETRIC) or an e on one side and 2 leptons + some missing energy on the other side or an e on one side and a broad jet on the other side and some amount of missing p_T
$p\bar{p} \rightarrow W^\pm \rightarrow \tilde{W}^\pm\tilde{\gamma}$ $\quad \quad \quad \downarrow \tilde{q}\tilde{q}$	$(q_1q_2\tilde{q}_3\tilde{\gamma}\tilde{q}, \tilde{\gamma})$ or $(q\tilde{\gamma}\tilde{q}, \tilde{\gamma})$, so large missing energy and a very broad jet = 4 quark jets on the other side or some missing p_T and a broad jet = 2 quark jets
$p\bar{p} \rightarrow W^\pm \rightarrow \tilde{W}^\pm\tilde{\gamma}$ $\quad \quad \quad \downarrow \ell\nu\tilde{\gamma}$ or $q\tilde{q}\tilde{\gamma}$	Missing energy + 1 lepton Missing energy + (1 "broad" jet = 2 quark jets) on the other side
$p\bar{p} \rightarrow W^\pm \rightarrow \tilde{\ell}\tilde{\nu}$	$= \ell\tilde{\gamma}\tilde{\nu}$: missing energy + 1 lepton (or completely different picture if $\tilde{\nu}$ decays in charged mode)

Tab 2a

Non-SUSY competing processes in $p\bar{p}$ collisions

Process	Signature
$p\bar{p} \rightarrow q\bar{q}$ $\quad \quad \quad gg$	1 jet on each side
$p\bar{p} \rightarrow Q\bar{Q}$ $\quad \quad \quad \downarrow q_1q_2\tilde{q}_3$ $\quad \quad \quad \downarrow q_1\ell^+\nu$	(1 "broad" jet or 3 quark jets) or (1 quark jet + 1 lepton + small missing energy) } on each side
$p\bar{p} \rightarrow L^+L^-$ $\quad \quad \quad \downarrow \nu\ell\nu_L$ $\quad \quad \quad \downarrow q_1\tilde{q}_2\nu_L$	(Missing + 1 lepton) or (Missing + 1 "broad" jet = 2 quark jets) } on each side
$p\bar{p} \rightarrow W^\pm (g \text{ or } q)$ $\quad \quad \quad \downarrow \text{energetic } \nu +$ $\quad \quad \quad \downarrow \text{slow lepton}$	1 jet on one side + [missing energy and maybe (if detected) a lepton] on the other side
$p\bar{p} \rightarrow W^\pm$ $\quad \quad \quad \downarrow \ell^+\nu$	Missing p_T + lepton
$p\bar{p} \rightarrow W^\pm$ $\quad \quad \quad \downarrow L\nu$ $\quad \quad \quad \downarrow \ell\nu\tilde{\nu}$ $\quad \quad \quad \downarrow q\bar{q}\nu$	Small missing p_T + one energetic lepton or Missing p_T + 1 "broad" jet or 2 quark jets

Tab 2b

Comparison between SUSY and non-SUSY competing processes in $p\bar{p}$ collisions

Kind of signature	Processes having the same signature	
	Process	Final state
1 jet on each side	$p\bar{p} \rightarrow q\bar{q} \rightarrow$	q or g on each side
	$\quad gg$	
	$\rightarrow Q\bar{Q} \rightarrow$	$(q_1 q_2 \bar{q}_3)$ or $(q_1 \ell^\pm \nu)$ on each side
	$\rightarrow L^* L^{-*} \rightarrow$	$(q_1 \bar{q}_2 \nu_L)$ on each side
	$\rightarrow \tilde{g}\tilde{g}^* \rightarrow$	$(q_1 \bar{q}_2 \tilde{\gamma})$ on each side
	$\rightarrow \bar{q}\bar{q} \rightarrow$	$(q_1 q_2 \bar{q}_3 \tilde{\gamma})$ or $(q_1 \tilde{\gamma})$ on each side
Missing p_T + 1 "jet" on the other side	$p\bar{p} \rightarrow W^\pm g \rightarrow \nu + \text{slow } \ell^\pm + g \rightarrow$	Missing + g + (ℓ^\pm)
	$p\bar{p} \rightarrow W^\pm \rightarrow L\nu^* \rightarrow$	Missing + $(q_1 \bar{q}_2 \nu_L)$
	$p\bar{p} \rightarrow \tilde{g}\tilde{\gamma}^* \rightarrow$	Missing + $(q_1 q_2 \tilde{\gamma})$
	$p\bar{p} \rightarrow \bar{q}\tilde{\gamma} \rightarrow$	Missing + $[(q_1 q_2 \bar{q}_3 \tilde{\gamma}) \text{ or } (q\tilde{\gamma})]$
	$p\bar{p} \rightarrow \tilde{W}^\pm \tilde{\gamma}$	Missing + $(q_1 q_2 \bar{q}_3 \tilde{\gamma})$
	$\quad \downarrow \bar{q}\bar{q}^*$ $\quad \downarrow W^\pm \gamma^* \rightarrow$	or $(q\tilde{\gamma}\bar{q})$ Missing + $(q_1 \bar{q}\bar{q}_2 \tilde{\gamma})$
Missing on 1 side +	$p\bar{p} \rightarrow W^\pm \rightarrow L^\pm \nu^* \rightarrow$ $\quad \rightarrow \ell^\pm \nu \bar{\nu}$	Missing + 1 lepton
1 lepton on the other side	$p\bar{p} \rightarrow W^\pm \rightarrow \bar{e}^\pm \bar{\nu}_e \rightarrow$	Missing + $(e^\pm \tilde{\gamma})$ (if $\bar{\nu}$ does not decay in charged mode)
	$p\bar{p} \rightarrow W^\pm \rightarrow \tilde{W}^\pm \tilde{\gamma}^*$	Missing + $(\ell^\pm \nu \tilde{\gamma})$
	$\quad \downarrow "W^\pm" \tilde{\gamma}$ $\quad \downarrow \ell^\pm \nu$	

*We denote with an asterisk the processes which have just an identical signature in terms of missing p_T , jetty structure and lepton content and by "W $^\pm$ " a virtual W.

Tab 3

FIGURE CAPTIONS (Chap. 2)

- 1) $d\sigma/dp_T$ for inclusive jet and π^0 production at $\sqrt{s} = 2$ TeV.
- 2) $d\sigma/dp_T$ for jet production for various choices of the compositness scale.
- 3) $d\sigma/dp_T$ for jets measured at the $S\bar{p}pS$ Collider and the ISR (II,32).
- 4) $p\bar{p} \rightarrow \mu^+\mu^-$ at $\sqrt{s}=2$ TeV as function of $\tau = m_{\mu\mu}^2/s$ for various choices of the compositness scale.
- 5) Rapidity distribution for heavy quark production.
- 6) Cluster mass distribution for top ($m_t = 35$ GeV) (II,14).
- 7) $|I|^2$ as a function of the top mass.
- 8) H^0 branching ratios as a function of the H^0 mass.
- 9) Cross section for Higgs production in $p\bar{p} \rightarrow Q\bar{Q}+H^0$ as a function of the Higgs mass (II,8).
- 10) Cross section for production of the Higgs in the reaction $p\bar{p} \rightarrow Q\bar{Q}H^0+X$ as a function of the quark mass. full circles are for $Q=b$ and the continuous line $Q=t$.
- 11) $R = \Gamma(Z^0 \rightarrow H^0 \mu^+\mu^-) / \Gamma(Z^0 \rightarrow \mu^+\mu^-)$ as a function of the ratio M_H/M_Z .
- 12) Cross section for production of heavy quarks pairs by gluon and quark fusion as a function of the quark mass, for two different choices of structure functions (DO = Duke-Owens, RE = Owens and Reya).
- 13) ν lifetime as a function of M_ν for two different choices of the mixing angle between ν and charm.
- 14) $d\sigma/dp_T$ of leptons from various sources.
- 15) a) Cross section for heavy lepton production through a charged IVB,
b) Cross section for heavy lepton pair production through a neutral IVB,
In both figures the cross section is shown as a function of the mass of the superlepton, for various energies (0.54, 2, 20 TeV) and for Duke-Owens and Owens-Reya structure functions.
- 16) Angular distribution of muons from $W \rightarrow \mu\nu$ and $W \rightarrow \tau\nu$, $\tau \rightarrow \mu\nu\nu$ decay vs. the p_T of the muon, at $\sqrt{s}=540$ GeV.
- 17) Inclusive jet cross-section $d\sigma/dp_T^{miss}$ at $\sqrt{s}=540$ GeV from QCD jets and W decay.
- 18) Opening angle between the two jets of the hadronic decay of a superlepton for two different masses, at

$\sqrt{s}=540$ GeV.

- 19) Production cross section of the technipion as a function of mass, for various energies (2, 10, 20, 40, 70, 100 TeV).
- 20) Branching ratios for techipion decay as a function of its mass.
- 21) Cross section for technieta production for various energies, as a function of the P_8^0 mass.
- 22) Cross section for gluino production as a function of its mass, at $\sqrt{s}= 0.06, 0.54, 0.8, 2, 10, 40$ TeV.

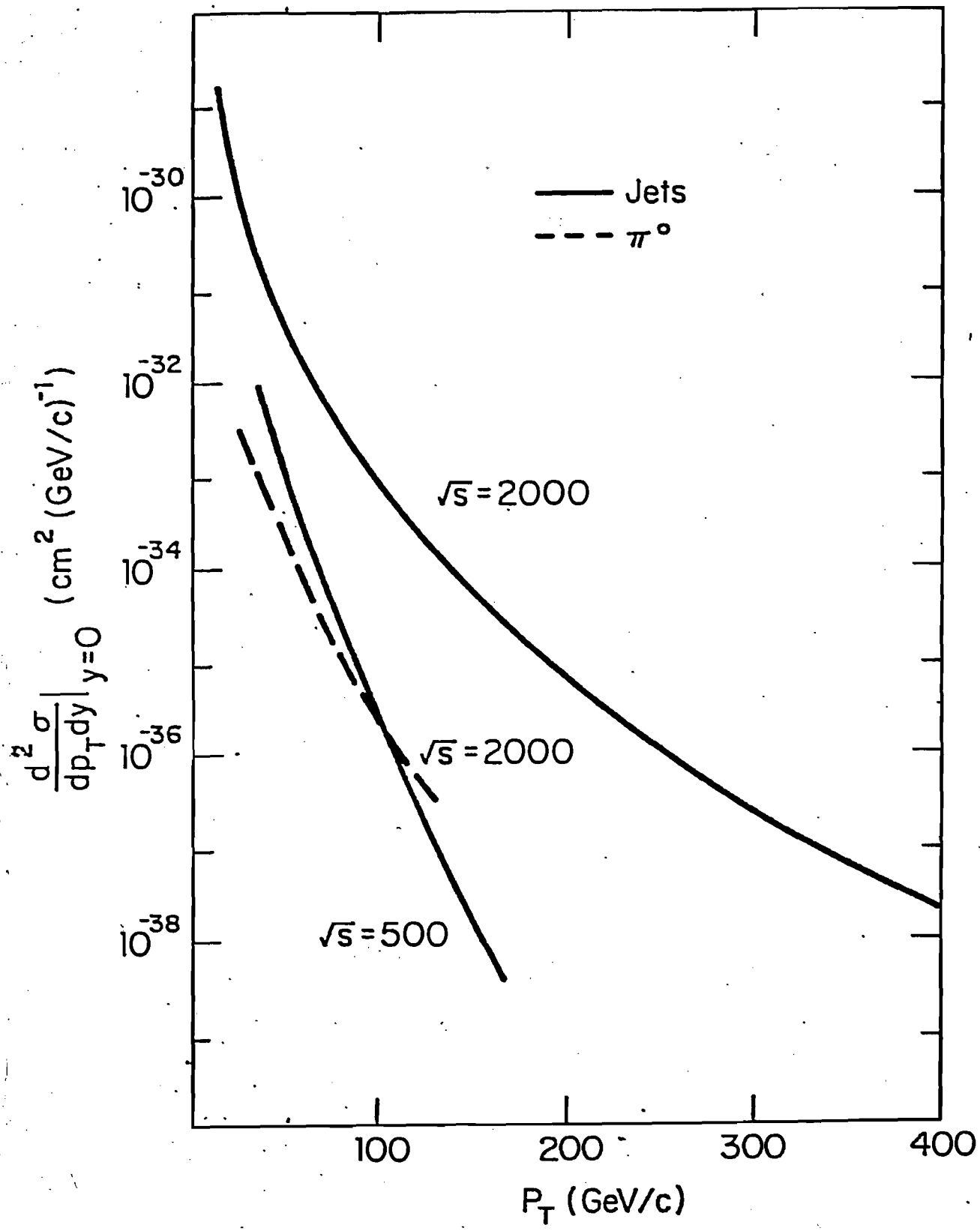


Fig 1

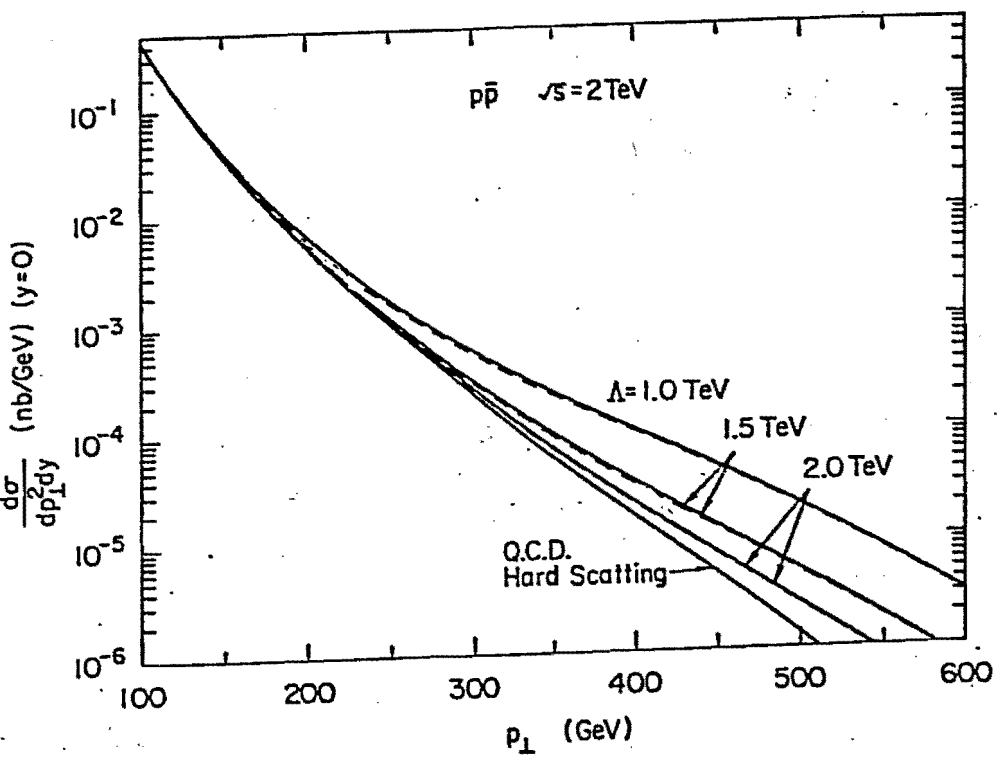


Fig 2

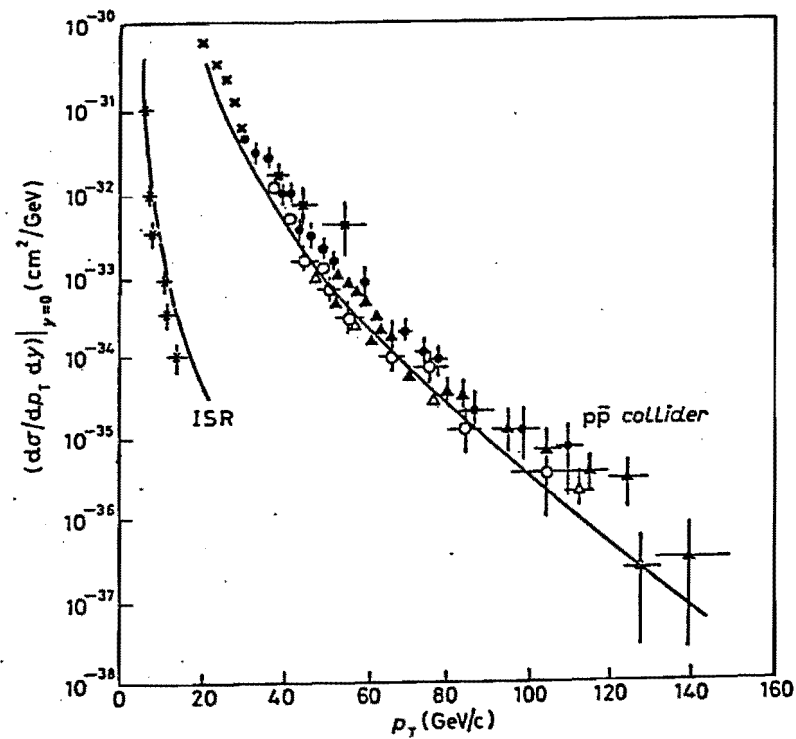


Fig 3

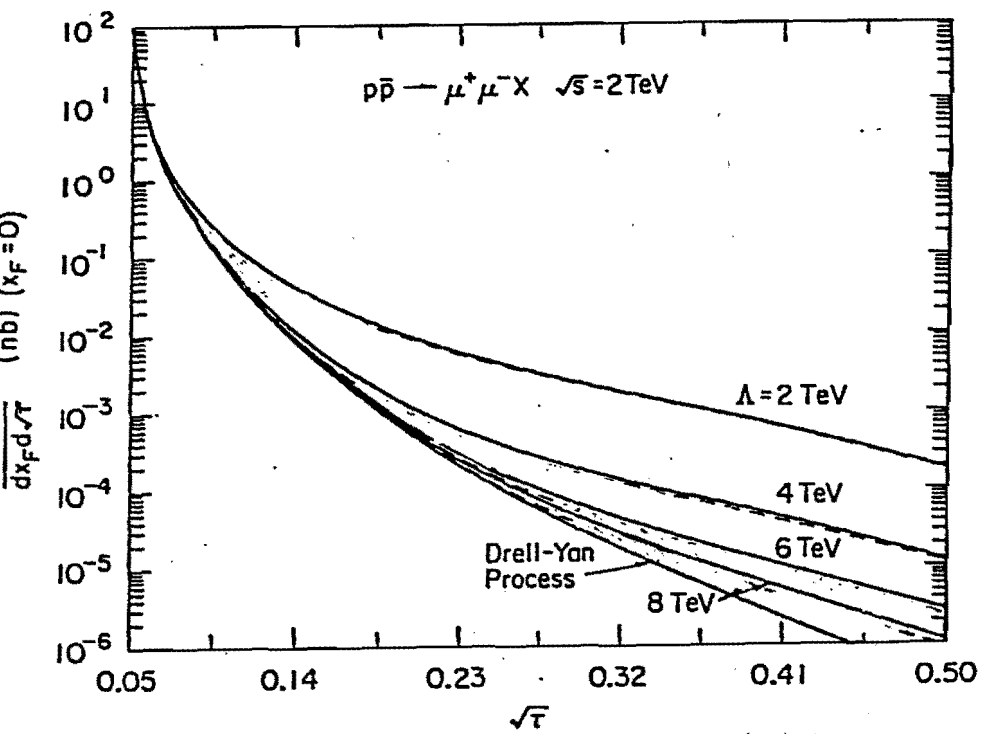


Fig 4

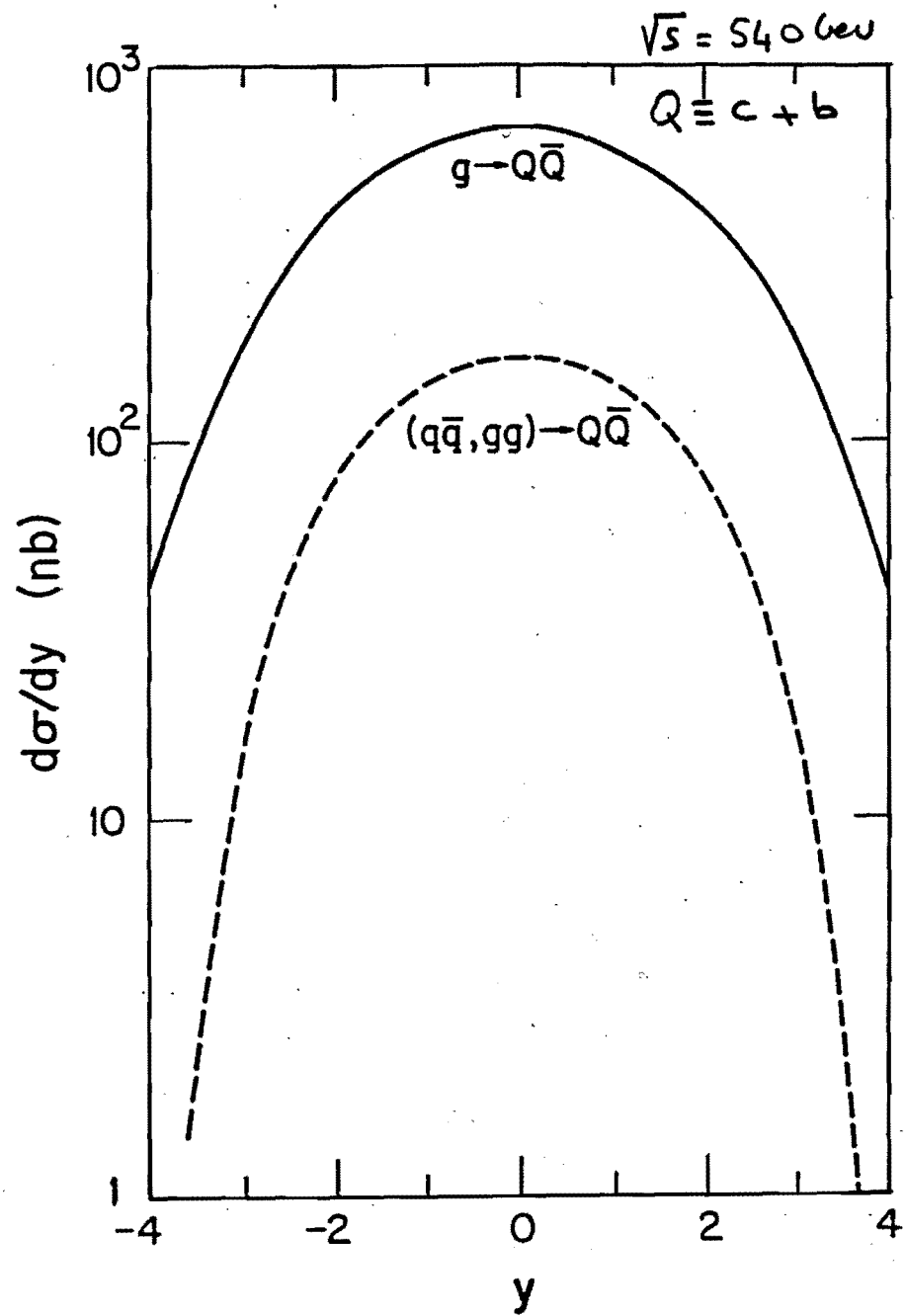


Fig. 5

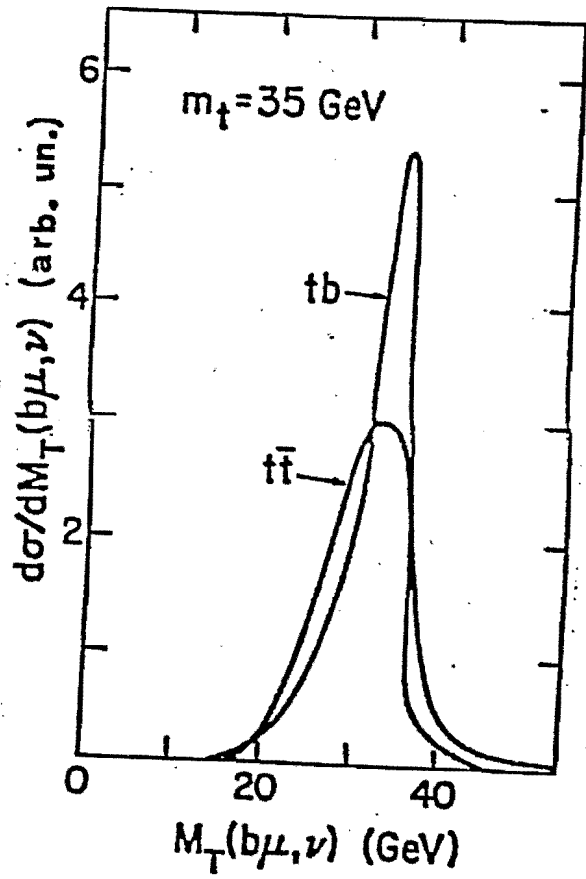


Fig 6

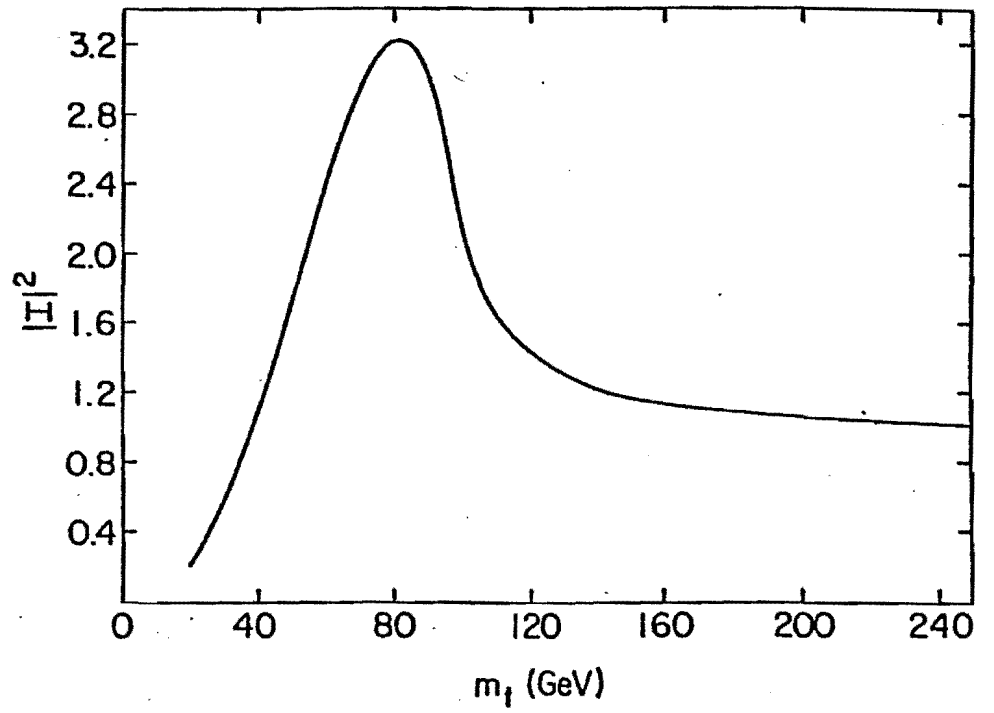


Fig 7

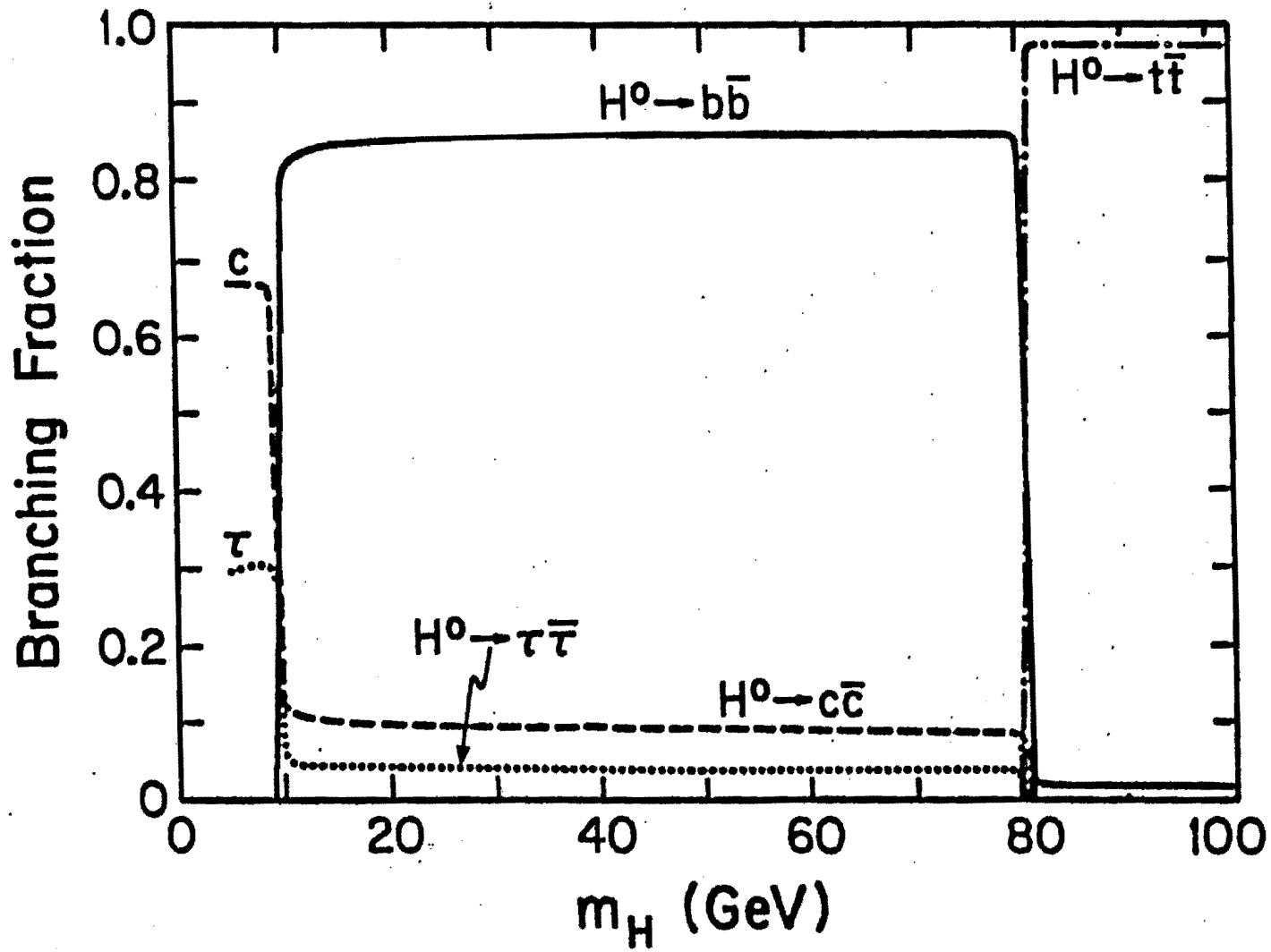


Fig 8

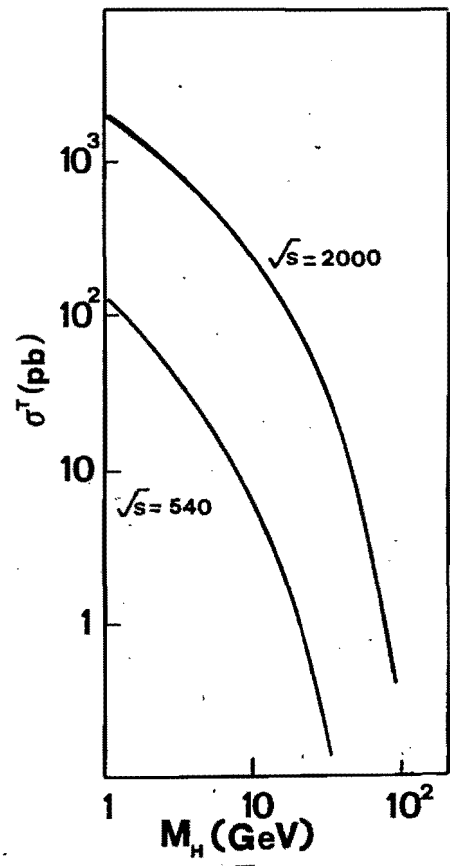


Fig 9

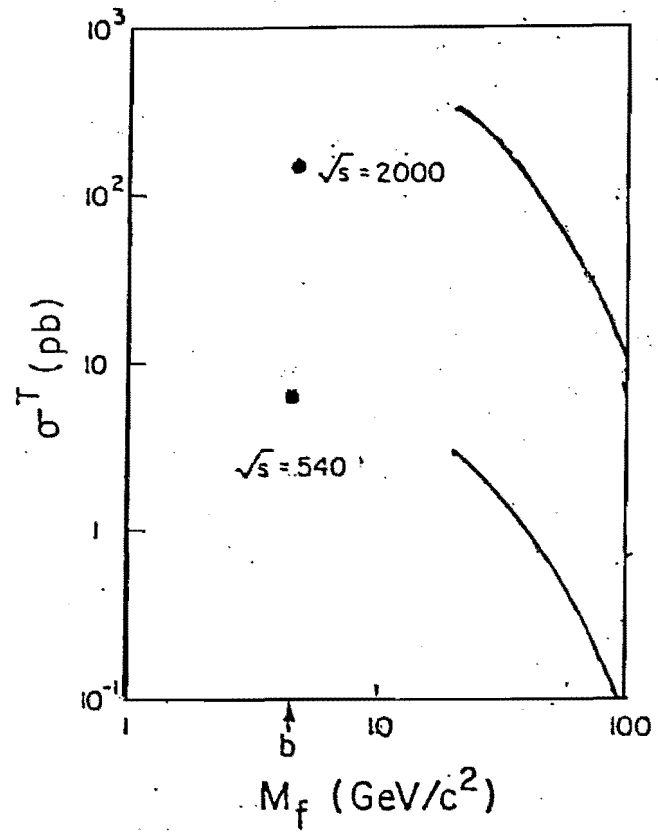


Fig 10

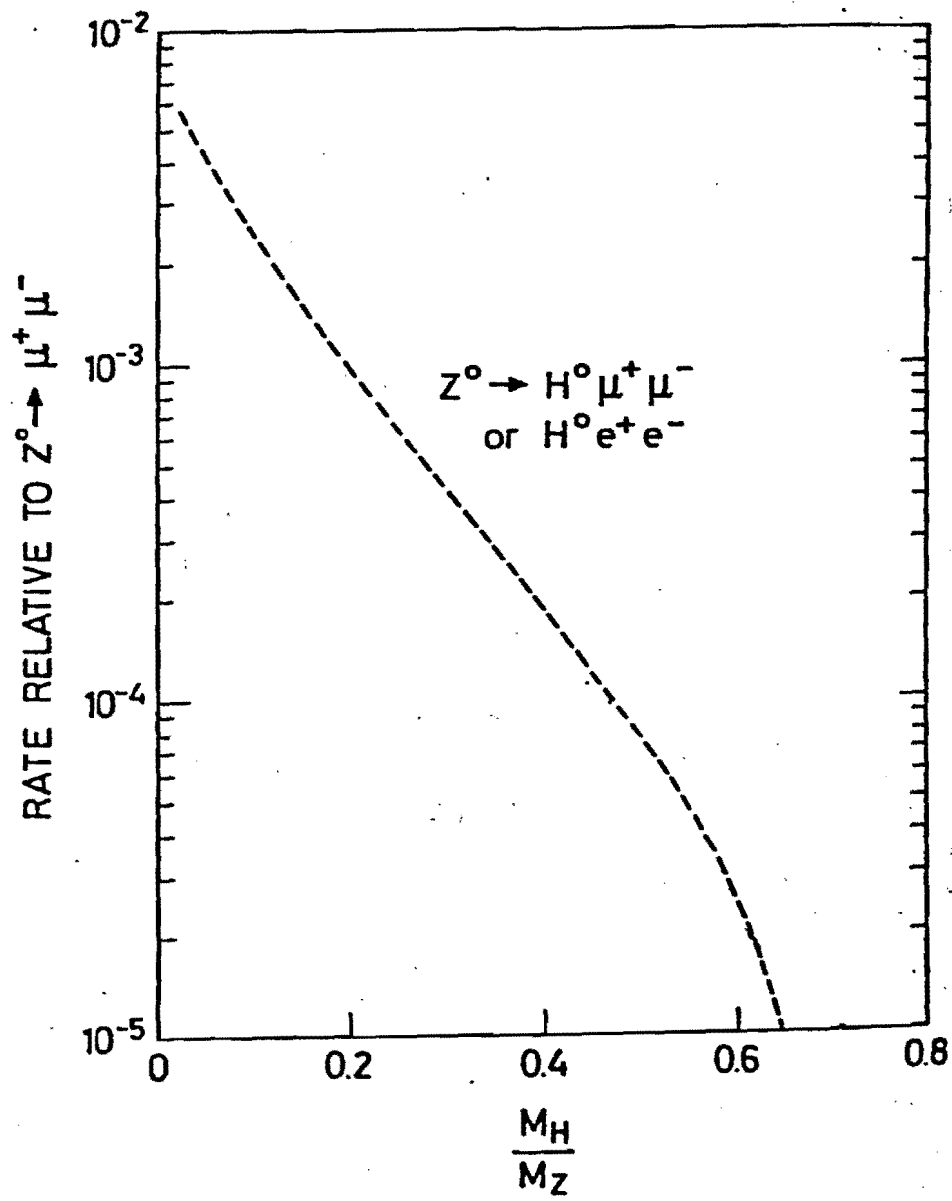


Fig 11

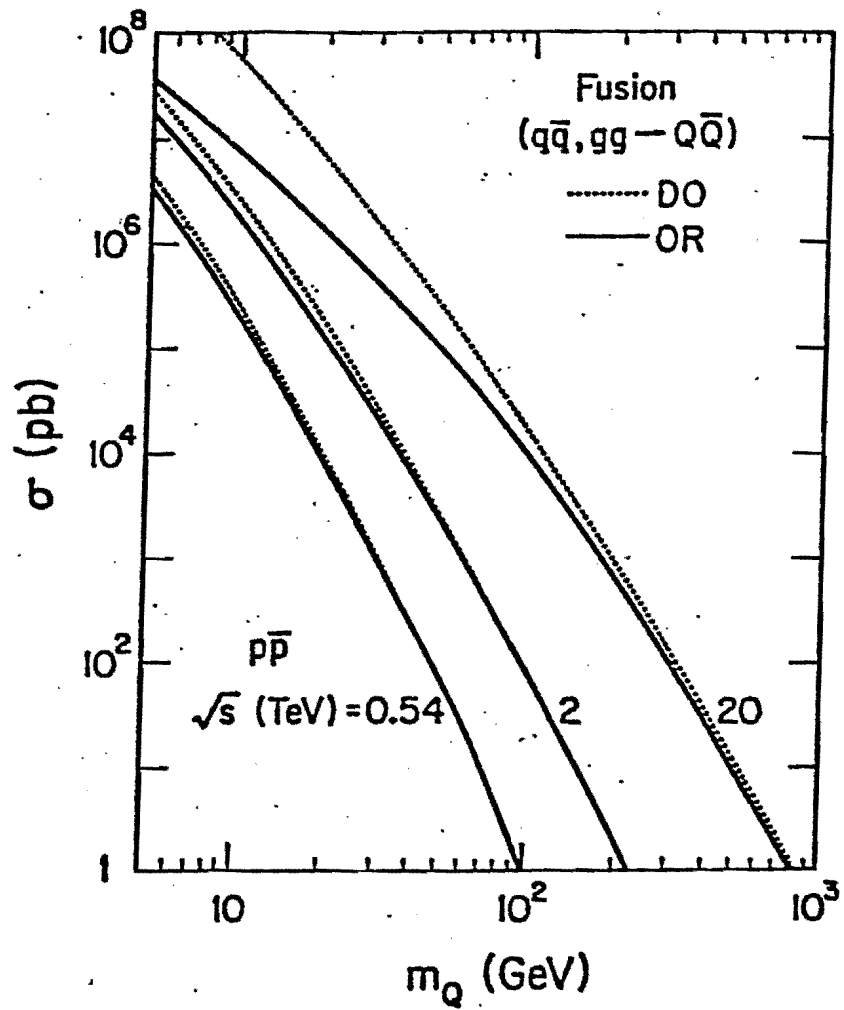


Fig 12

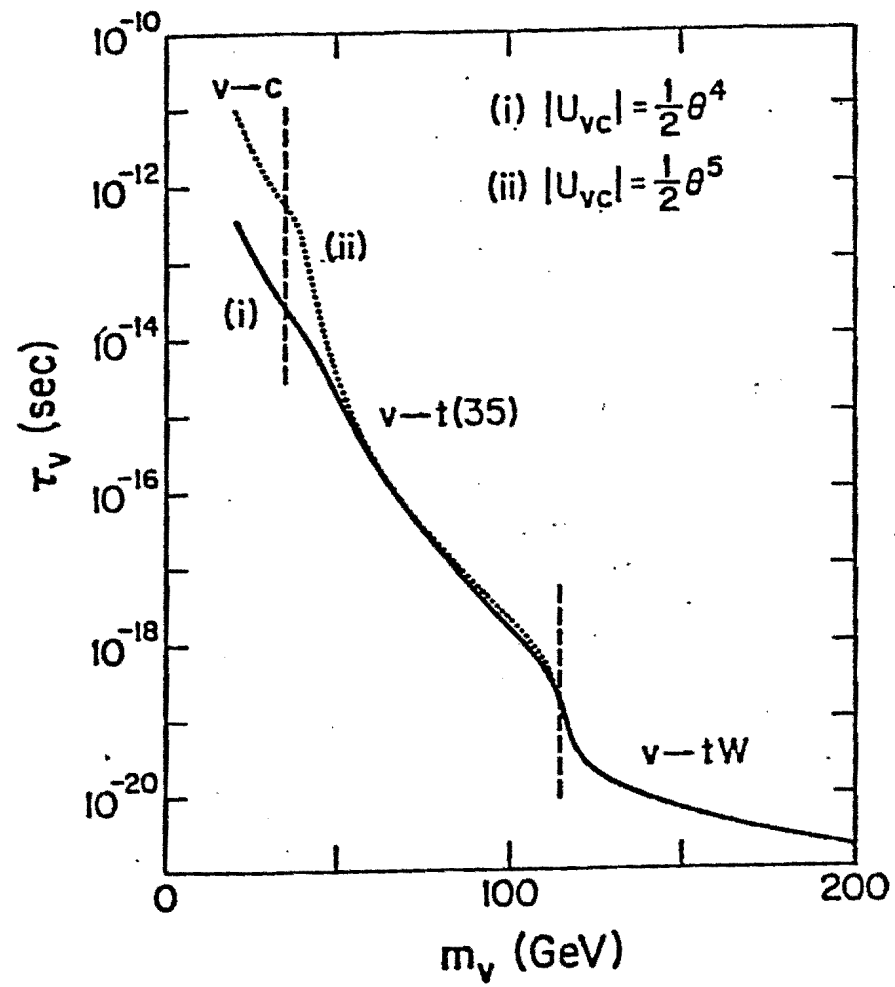


Fig 13

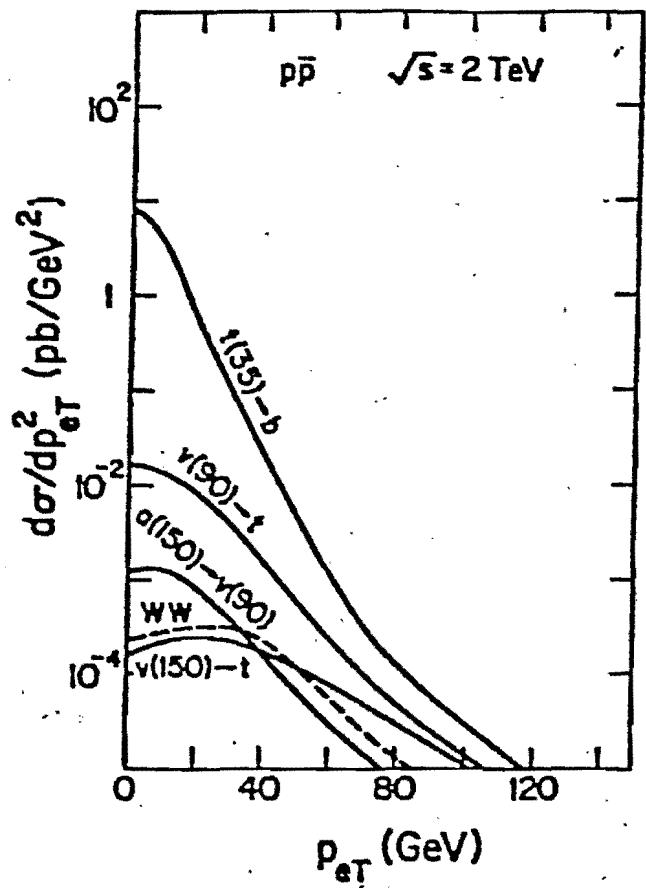


Fig 14

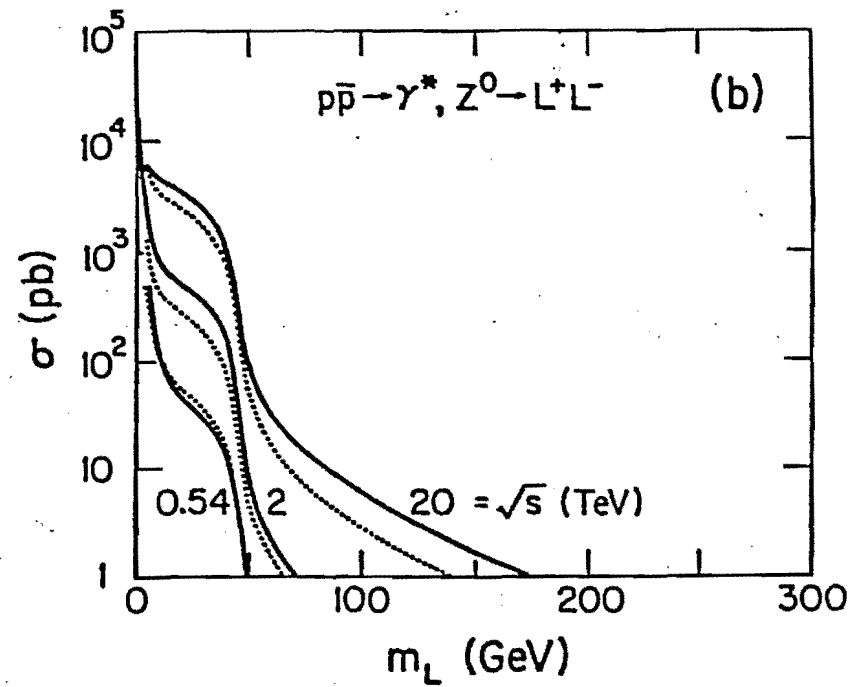
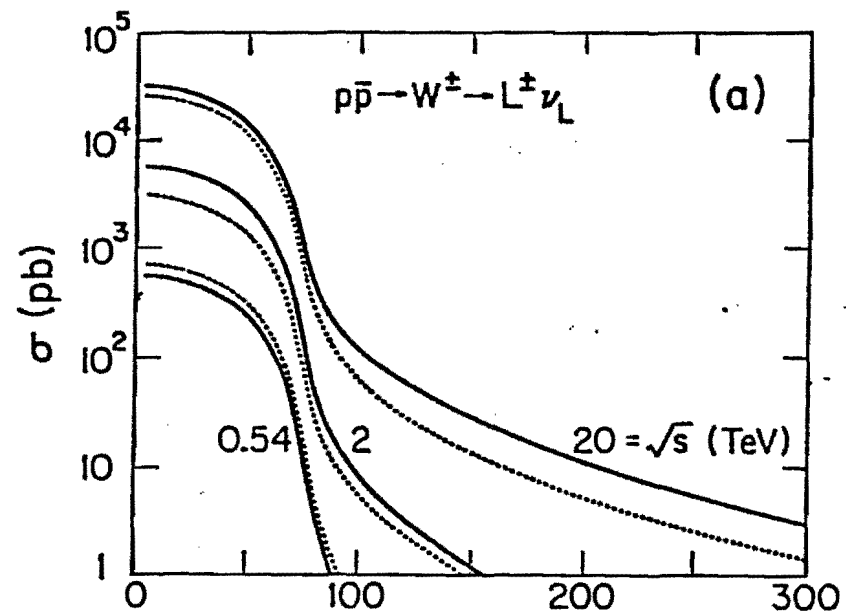


Fig 15

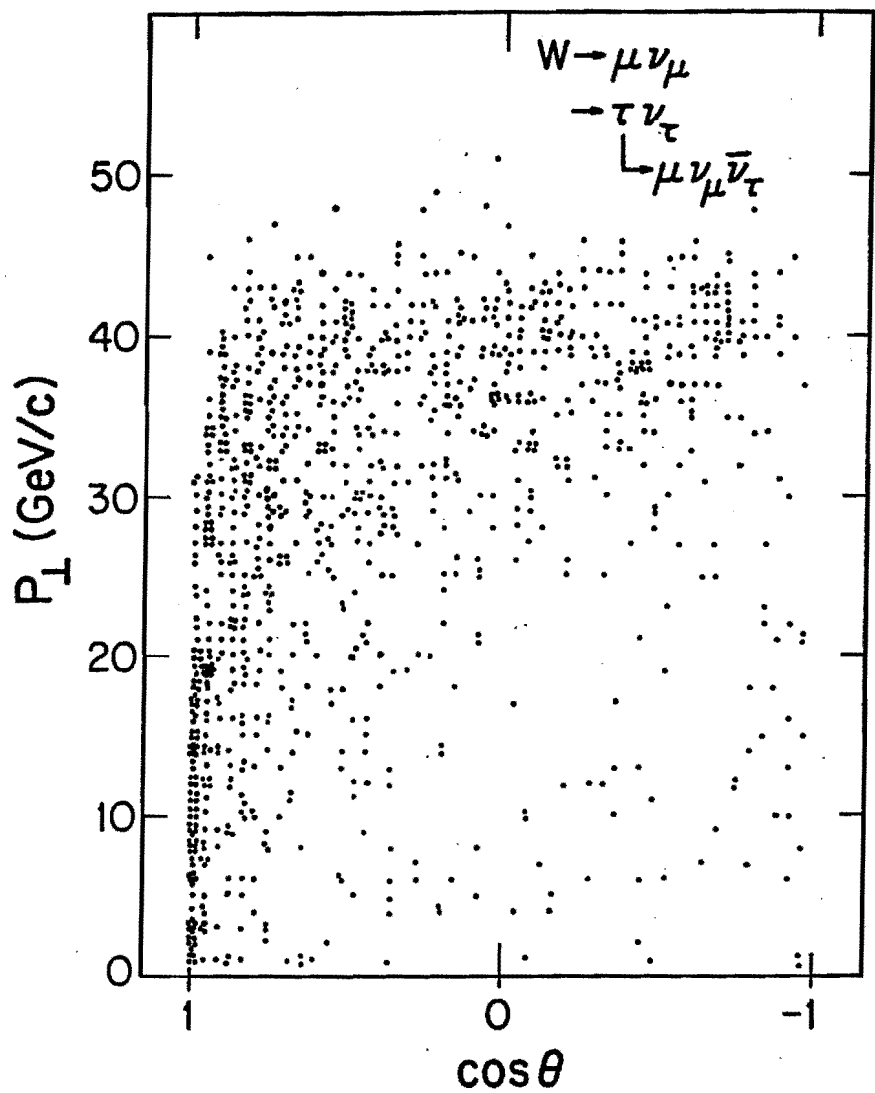


Fig 16

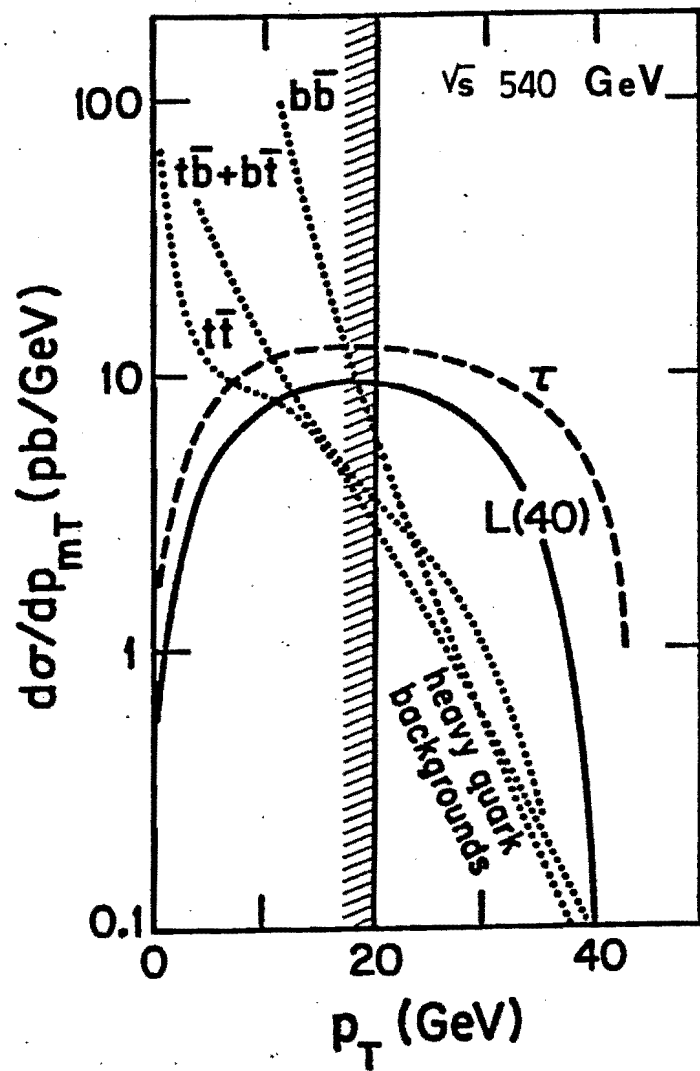


Fig 17

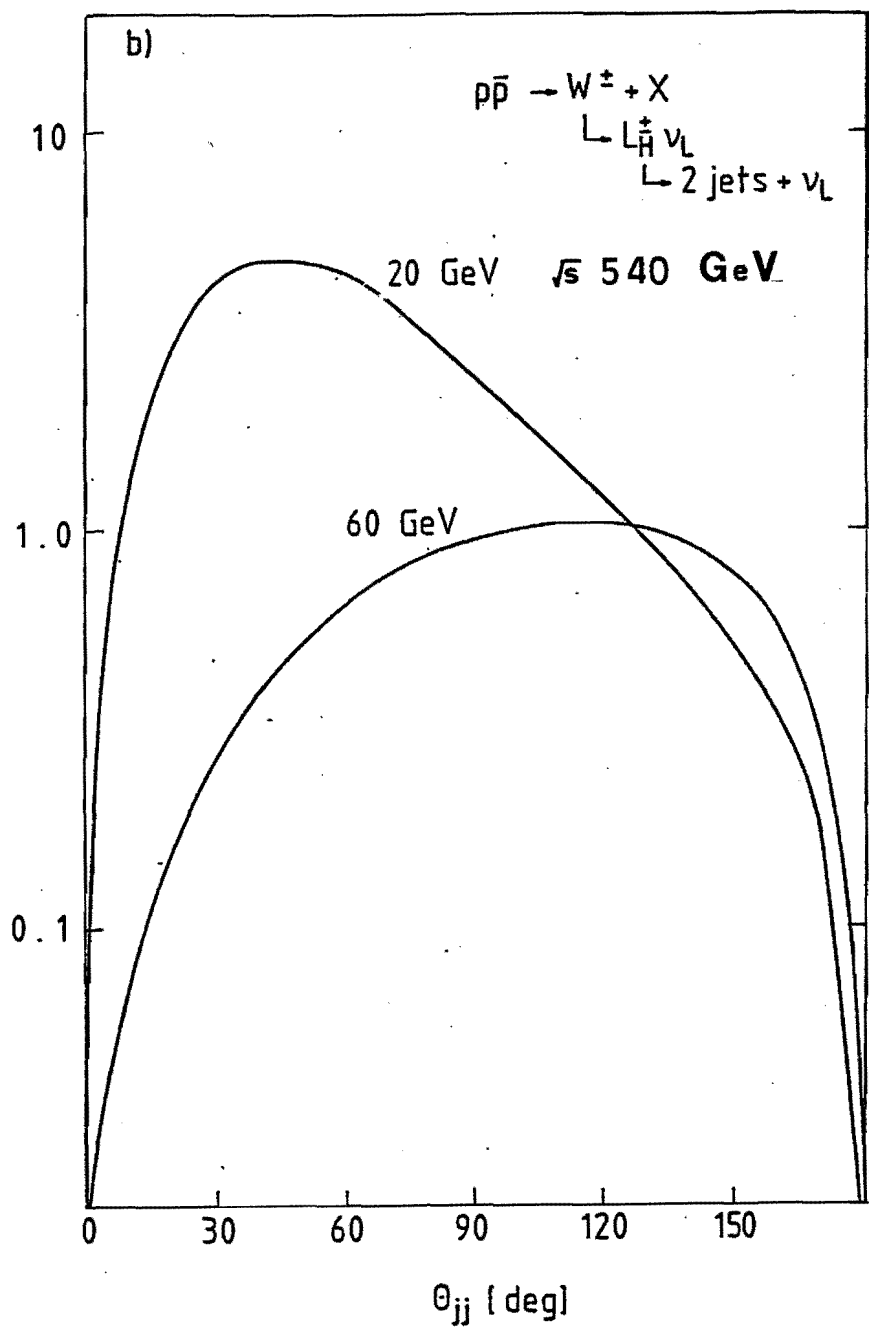


Fig 18

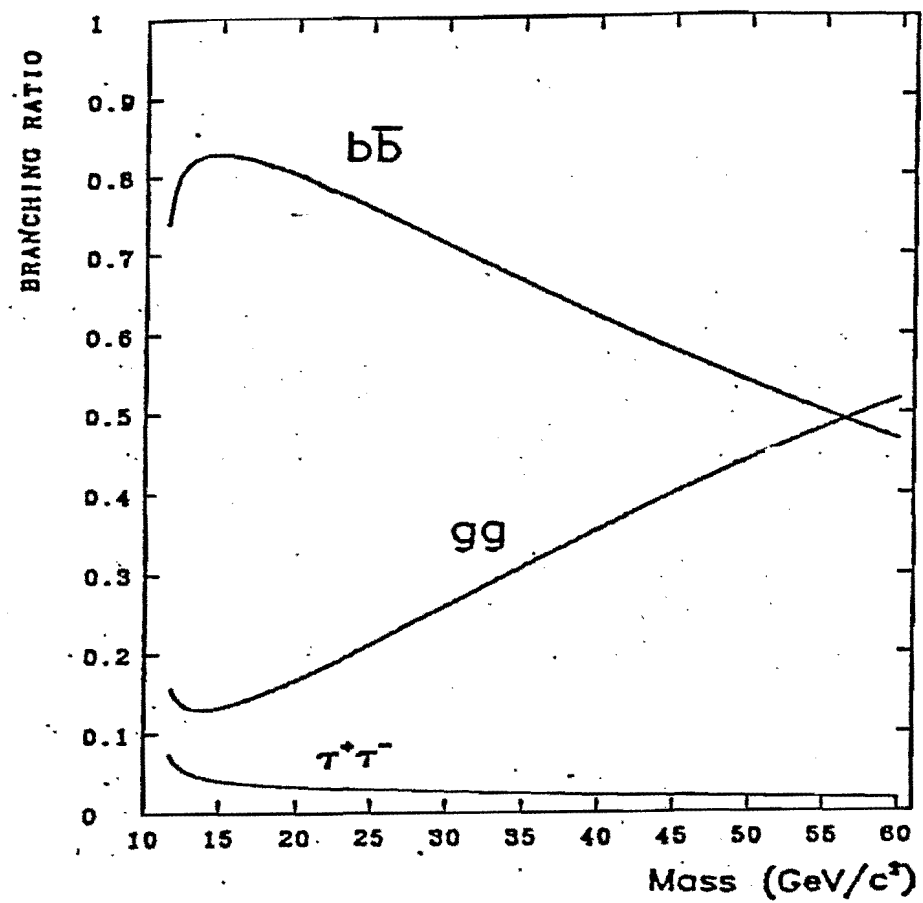


Fig 19

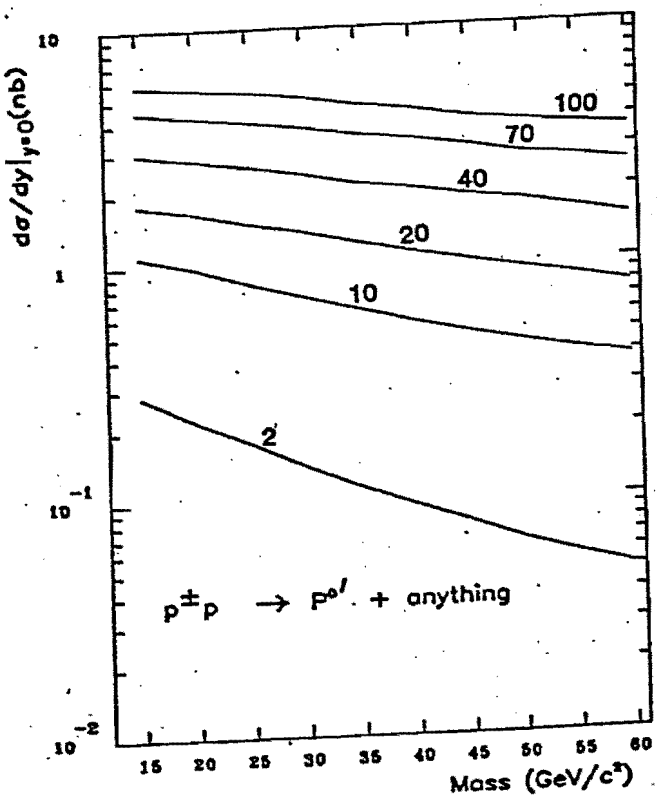


Fig 20

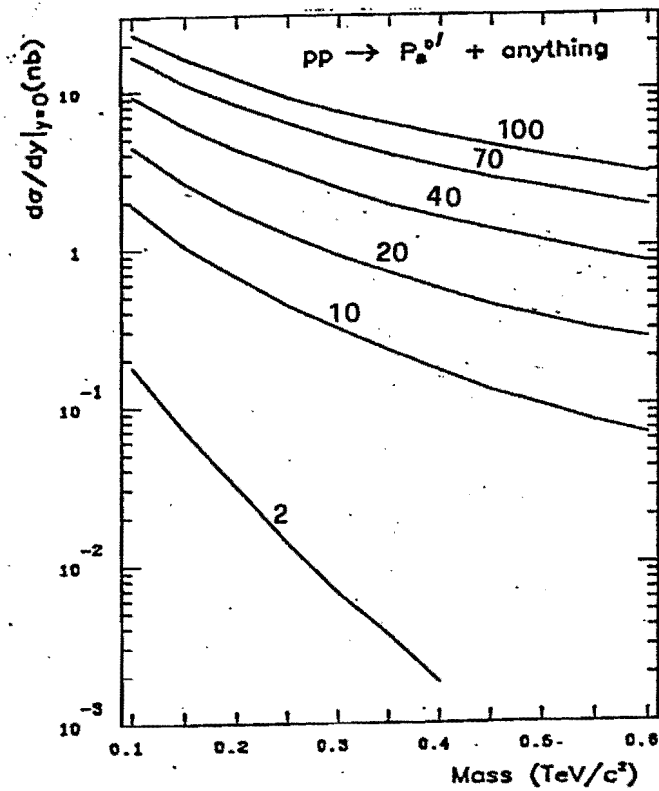


Fig 21

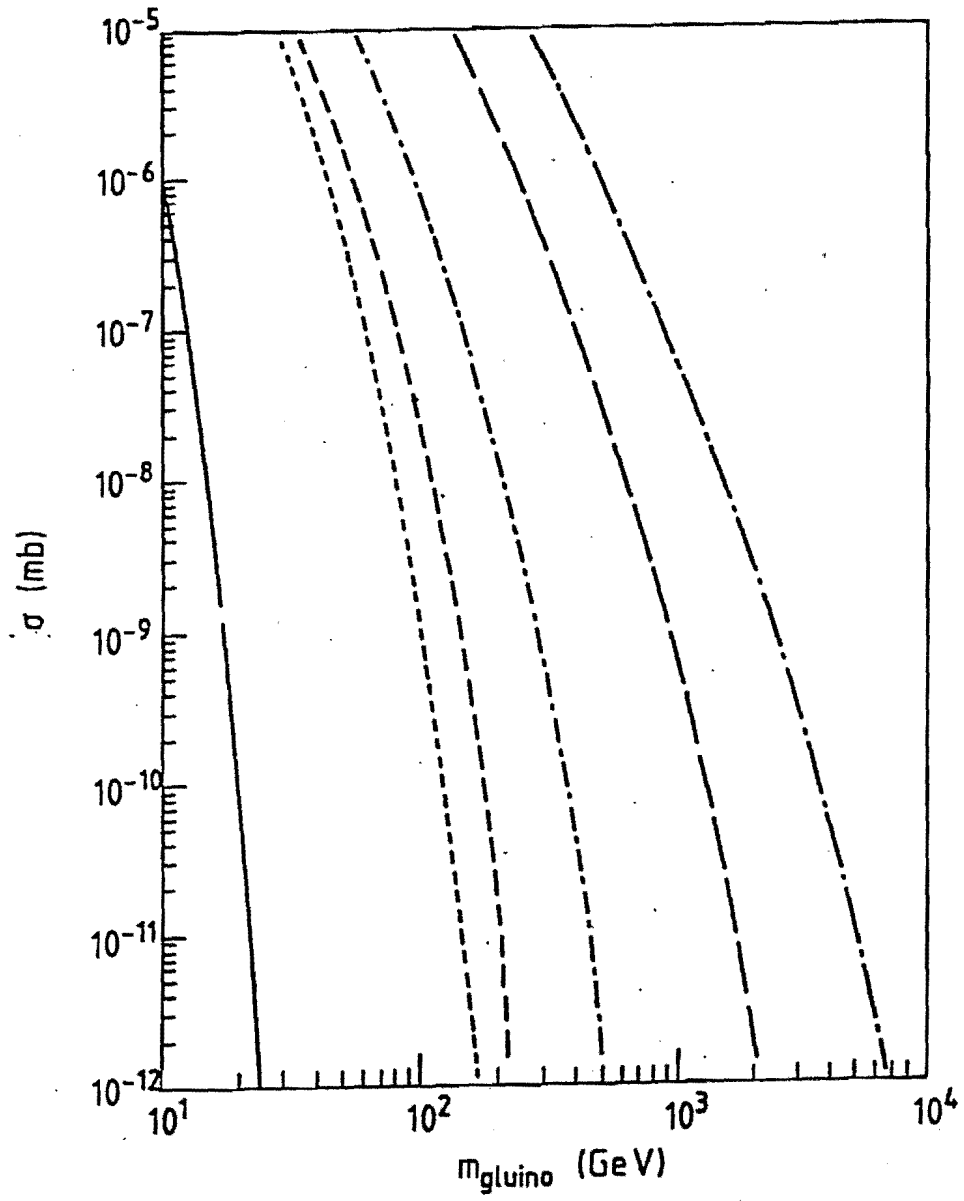


Fig 22

CHAPTER III

CDF

An overview of CDF is shown in fig.1 The main detector was designed such as:

- a) to cover the largest possible solid angle with suitable calorimetry to isolate hadronic jets in as much as they are separated in the event itself,
- b) to identify electron and (eventually) muons at all angles.

The complete CDF comprises a central detector, two forward spectrometers, and very small angle silicon detectors.

The central detector of CDF employs a large axial magnetic field. Such a field (15 KGauss) is provided by a superconducting solenoid magnet, which is ~ 3 m in diameter and ~ 3 m long. The flux return path is provided by the yoke of the magnet together with the endwall and the endplug calorimeters. The Central Detector is composed of three main sections (fig 2)

- a) a large cylindrical tracking system surrounding the interaction region, operating in a solenoidal magnetic field of 1.5 T to analyze the momentum of charged particles,
- b) A 4 calorimeter surrounding the tracking system down to a 2° hole
- c) outer muon chambers embedded on the rear of the central calorimeter modules at 45° .

A sketch of the forward spectrometers at $2^\circ \leq \theta \leq 10^\circ$ is shown in fig.3. Charged particles are traced through a telescope of "bicycle wheel" chambers. Electromagnetic and hadron calorimeters cover the angles between $\sim 2^\circ$ and $\sim 10^\circ$. Behind the calorimeters, two sets of magnetized toroids interleaved with drift chambers filter the muons and measure their momentum.

III.1 CALORIMETRY

The CDF calorimetry was studied to fit the expected topology of events generated in parton-parton collisions and their jetty flow of energy. The angular coverage has been made as hermetic as possible in order to allow a good measurement of the missing transverse energy which is the characteristic signal of ν 's. The calorimeters leave room

to an inner tracking system which also covers essentially 4π steradians. There are 4 calorimetric regions:

- a) central calorimeter $44^\circ \leq \theta \leq 90^\circ$,
- b) endwalls $30^\circ \leq \theta \leq 52^\circ$,
- c) endplugs $10^\circ \leq \theta \leq 30^\circ$,
- d) forward/backward $2^\circ \leq \theta \leq 10^\circ$,

The calorimeter system is separated in two regions: a front part where most of the e.m. energy is contained (using lead as a converter), followed by a rear part where most of the remaining energy for hadrons is contained (using iron as a converter). The sensitive medium is scintillator in a) and b), and gas tubes operating in proportional mode in c) and d). All the calorimeters are arranged in projective towers. The tower size is such that jets are expected to be contained within a few towers at any angle.

Gas calorimetry has been adopted at angles $\theta \leq 30^\circ$ where jets get narrower and in general a high density of energetic tracks is expected, and thus finer granularity is needed. In addition at these angles scintillator would deteriorate fast because of radiation damage. Scintillator was used at large angles to achieve a better energy resolution and to provide a more selective fast trigger.

III.1.1 The Central and End Wall Hadron Calorimeter

The central calorimeter is a set of 48 barrels comprising 24 modules in azimuth and two modules along z (tab.1.a). The modules are arranged in four half-arches which surround the coil and do not participate in the magnetic circuit. Each module is divided into towers projecting to the detector center with a granularity $\Delta\psi = 15^\circ$, $\Delta\eta = .11$. In the rear hadron sector, each tower is a sandwich of 2.5 cm iron slabs and 1.0 cm scintillator sheets. The towers in the front e.m. sector are sandwiches of 3.2 mm Pb-sheets and 6.3 mm scintillator sheets. A proportional wire chamber located at $\sim 5.7 X^\circ$ inside the e.m. sector measures the position and samples the energy of the electromagnetic showers at shower maximum. In fig.4 the result of the energy resolution for both e.m. and hadron calorimeter are shown as measured on a test beam (III,1).

The end wall calorimeter at $30^\circ \leq \theta \leq 52^\circ$ extends the tower structure of the barrel over this region. The iron of the

endwalls is a part of the return path of magnetic field. This calorimeter is only hadronic and employs the same techniques as the central hadron calorimeter, i.e. scintillator sandwiched between iron plates. Although the iron is 5 cm thick, the expected performances in energy and position resolution are not very different from those of the central calorimeter (Tab. 1.b).

III.1.2 Endplugs

These calorimeters are arranged in pyramidal towers (fig 5) with the interaction vertex at the apex, with $\Delta\psi=5$, $\Delta\eta=.1$, and cover the range $10^\circ \leq \theta \leq 30^\circ$.

The energy measurement is done with proportional wire chambers sandwiched between 4 mm thick lead plates in the e.m. sector and between 5 cm thick iron plates in the hadron sector. In both e.m. and hadron sectors, the tower geometry is realized by suitable patterns of pads cut on printed circuit boards. Pads are ganged together as to provide three independent longitudinal readouts in the e.m. sector and for two more in the hadron sector. In Tab.2 we summarize the expected energy resolution and accuracy in measuring position and direction of the energy flow of this calorimeter.

III.1.3 Forward Calorimeter

The region from $\theta = 10^\circ$ down to the $\sim 2^\circ$ hole is covered by a fine-grained gas calorimeter, whose design and performances are similar to those described for the Endplugs.

Until today only the E.M. section has been tested with the beam, and an energy resolution $\sigma(E)/(E) = 34\%/(E)^{1/2}$ has been obtained (III,2).

III.2 MUON SYSTEM

As its start the muon coverage of CDF will not be complete. Muon identification is planned in the forward region at $5^\circ \leq \theta \leq 10^\circ$ and in the central region at $45^\circ \leq \theta \leq 90^\circ$.

III.2.1 Forward Muons

At small angles two sets of magnetized solid iron toroids will be used to measure muon momenta. These toroids are 5.5 m in diameter at 11.6 m from the intersection, covering the range $5^\circ \leq \theta \leq 10^\circ$. Drift chambers are located in front, between and behind the toroids. The muon momentum resolution is $\sim 20\%$, and is dominated by multiple scattering in the iron.

An additional set of two toroids is being designed to extend the coverage to larger angles. It consists of two 1 m thick elements which are magnetized to 18 KGauss, and interleaved with drift chambers. They are about 8.8 m in diameter and are located at about 4.6 m from the crossing point, covering the angular range $10^\circ \leq \theta \leq 30^\circ$.

III.2.2 Central Muons

At intermediate angles ($30^\circ \leq \theta \leq 45^\circ$) muons are not really identified in the first generation of CDF. However, since the muon momentum is analyzed in the central tracking systems, muons will look different from most hadrons since they will show a mismatch between momentum and energy released in the calorimeter. An additional tracking outside the calorimeters and suitable additional iron structures are under study to improve muon identification in this angular range.

At $45^\circ \leq \theta \leq 90^\circ$, a telescope of four large-gap drift chambers is enclosed in the shells of the central wedges on the rear of the hadron calorimeter. The drift tube wires are parallel to the solenoid axis, while the z coordinate is measured by charge division.

This muon chambers-CTC-hadron calorimeter system has an excellent rejection against cosmic ray background. Hadron rejection would improve if the calorimeters were made thicker, as is being planned in the second generation of CDF. The rejection power of the present design (at the trigger level) is given in Tab.3.

III.3 THE TRACKING SYSTEM

The tracking system of CDF is composed of several

detectors which operate inside a solenoidal magnetic field of 15 KGauss. Ordered from the outside to the inside, these detectors are (III,3):

a) a double layer of limited streamer tubes, used mainly for triggering purposes

b) a central tracking chamber covering $13^\circ \leq \theta \leq 90^\circ$ at radial distance $32 \leq R \leq 140$ cm,

c) a set of time projection chambers covering $5^\circ \leq \theta \leq 90^\circ$ at $12 \leq R \leq 30$ cm,

d) four layers of silicon vertex detector at $5^\circ \leq \theta \leq 90^\circ$ at $2.9 \leq R \leq 12$ cm.

Outside the field, at the exit of the central CDF detector, a telescope of radial drift chambers covers the angles $2^\circ \leq \theta \leq 10^\circ$.

III.3.1 Central Tracking Chamber (CTC)

The CTC is a cylindrical axial wire drift chamber with 84 layers arranged in 9 superlayers. Five of the superlayers contain 12 layers each of axial wires and are interleaved by four alternating layers of stereo wires (3). Each stereo layer contains 6 sense wires. Fig.6a shows one of the chamber endplates and illustrates the tilting of the wire sets relative to the cylinder radius. Fig 6.b shows the detail of the axial superlayers. Due to the tilting of the cells the drift direction is approximately in the phi direction when the magnetic field is 15 KG thus sharpening the time-distance relationship. Also, because of the tilting the right-left ambiguity is easily resolved because the ghost track is rotated respect to the true track by about 70° .

The expected $R-\varphi$ resolution is $\sim 200 \mu\text{m}$ for a single wire, as confirmed by a cosmic ray test performed with a small prototype where an efficiency of above 99 % per wire was also found (III,4). The expected momentum resolution at 90° is $\Delta p_T / p_T^2 \approx 10^{-3} \text{ GeV}$.

Stereo wires measure the longitudinal coordinate. The expected z resolution is : $\sigma_z = .2\text{mm}/\sin(3^\circ) = 4 \text{ mm}$.

Charge division is implemented on the innermost axial super layer to aid the pattern recognition. This is particularly important for tracks which leave the detector before the first stereo super layer. The outer double layer

of limited streamer drift tubes just inside the coil provides another three dimensional space point for particles in the range $45^\circ \leq \theta \leq 90^\circ$. The resolution of these tubes is about .1 % of the wire length (about 3 mm).

The two track separation as determined by the multiple-hit electronics is ~ 5 mm, a number which has been confirmed by the cosmic rays test, where a resolution of 3 mm in the average was obtained. To some extent double hits can be resolved by analysis of the flash ADC data or at least using a constraint on the drift times. Ultimately, the two track separation should be $\sim 1-2$ mm.

The Central Tracking Chamber can be used to form a prompt trigger for high p_T tracks. For this purpose only axial wires and the drift tubes are used. A prompt trigger is possible using a coincidence of radially aligned sense wires. Because of the wire geometry, for tracks with $p_T \geq 5$ GeV/c there is at least 1 sense wire per superlayer which is less than 4 mm away from the track, thus at less than 80 nsec in time from the beam-beam crossing signal (fig 7).

Such a trigger has been studied in detail (III,5) and work is in progress for its implementation.

III.3.2 The VTPC

A set of 6 small Vertex Time Projection Chambers are positioned around the beampipe covering the region $5^\circ \leq \theta \leq 90^\circ$. The two central ones leave room for the Silicon Vertex Detector (fig 8)

The VTPC's provide 3-dimensional information on the general event topology and in particular signal the occurrence of multiple events. This is an important function since with $L = 10^{30} \text{ cm}^{-2} \text{ sec}^{-1}$ the probability for an interaction to be double is $P_2 \sim 20\%$. If the two vertices are required to be at a relative distance of not more than 1 cm (a resolution which can be easily obtained with the VTPC's), this probability decreases to $\sim 1\%$. In the off-line analysis, the VTPC will improve the lepton signature and momentum resolution at $5^\circ \lesssim \theta \lesssim 35^\circ$ where the CTC resolution is poorer.

Each VTPC has an octagonal shape and is divided into two drift regions, 15 cm long each. The HV electrode is at the

center. On the two sides a grid shapes the electric field. Behind the grid, a plane of sense wires is oriented in the ψ direction. The sense wire plane is split into eight sectors. Finally three rings of pads are printed on the end plates. From outside to inside, the rings contain 88, 64, 40 pads respectively. In the two central VTPC only two rings of pads will be located, to leave room for the SVX.

The R-z coordinate of a track is measured by the drift time to one of the sense wires of the octants. The annular rings pads are used to measure R- ψ by measuring the ratio of the charges induced in neighboring pads. The resolution in z is 200-300 μm depending on the drift distance, and the resolution in R- ψ is 250 μm (for single tracks).

III.3.3 The Forward Tracking

In the forward region, $2^\circ \leq \theta \leq 10^\circ$, the direction of the outgoing charged particles is measured by a radial drift chamber (RDC) (fig.9). The RDC is divided in 72 azimuthal cells. The geometry provides smaller drift spacing for smaller angles, which is a useful feature in a region where track density will be large.

A prototype of this chamber has been built and tested with cosmic rays. A resolution of $\sim 170 \mu\text{m}$ was obtained (III,6). With such an accuracy the coupling of the transverse momentum to the longitudinal solenoid field would allow to determine the charge sign for electrons up to $P_T \approx 20 \text{ GeV}$, down to 5° (III,7).

Left right ambiguities are solved by slanting the cells along z, thus each track crosses at least 2 cells. A fraction of the sense wires (a dozen at the start of CDF) will be instrumented with charge division readout. At the plane of these wires a resolution of $\sim 1 \text{ mm}$ will be obtained.

III.3.4 The CDF Silicon Vertex Detector

The reconstruction of vertices a few hundred microns away from the primary one is possible if a resolution in impact parameter of the order (or better) than 100 μm is reached.

Experience gained with the tracking systems operating at e^+e^- machines (DESY, PEP etc.) showed that the large central tracking chambers, whose main goal is to reconstruct the momentum of each track and the overall topology of the event, have a more modest resolution in impact parameter ($\sim 150 \mu\text{m}$). Small size high resolution devices very close to the interaction region (to keep the extrapolation error at a minimum) are the only way out in order to reach the required resolution.

In the following we briefly discuss two kinds of vertex detectors which have been developed for colliding beam experiments: high pressure drift chambers and silicon detectors. The first ones have been already employed and are also planned in a number of new experiments. The second ones are the solution adopted for CDF, that is comparatively more promising as well as more difficult.

a). High pressure drift chambers

High pressure vertex detectors are gas detectors located just outside the beam pipe around the interaction region (it is possible to use the beam-pipe as inner seal for the gas vessel to avoid an additional layer of scattering material). They generally operate with a pressure of more than 1 atm for an improved space and dE/dx resolution (III,8). Ultimate resolution of this type of chambers is (III,9) :

$$\sigma_1 \sim 30 \mu\text{m}, \quad \sigma_2 \text{ (2 track separation)} \sim 200 \mu\text{m}$$

This result, which is rather encouraging, was however obtained in a small, and well controlled prototype (III,9).

There are several problems for the operation of such chambers, because their resolution is strongly dependent on the stability and the uniformity of the electric field and of the gas pressure (the drift velocity is determined by the ratio electric field/pressure). A possible systematic tilting of the electric field is particularly dangerous, since changes in drift velocity and drift angle are induced. The mechanical stability of the detector is also a crucial point. Inevitably, electrostatic forces and gravity displace the wires by some amount, and the phenomenon can be very significant at the wire center. This displacement can be balanced by a suitable wire stress, but this requires thicker and more solid endplates, thus introducing heavy

material on particle trajectories at some angles. Since the exact position of each wire must be known within a few microns in order to benefit of the intrinsic resolution of the chamber, the end plates should be rigid and accommodate reliable fiducial marks. Finally, since the pressure stability depends on the stability of the temperature a careful cooling of the electronics is needed. This is not a trivial problem, given that these devices are bound to operate in a hardly accessible, and very compact region of the apparatus.

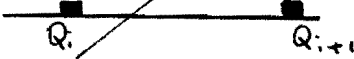
b) Silicon detectors

The basic idea of a silicon detector is to collect the charges generated by the energy loss of particles traversing the crystal. It has been found that 3.62 eV are needed on the average to generate an electron-hole pair in silicon and this charge can be integrally collected by applying an electric field to the semiconductor. In the case of Si at room temperature, however, a rectifying diode structure with a non-injecting rear contact must be used to avoid a large steady current which could mask the small induced signals. These devices were developed in the sixties and seventies mainly for application in nuclear physics experiments. In the second half of the seventies they were found to match well the request of high precision detectors to measure the very short lifetimes of charm and beauty particles.

Fast improvements in the techniques and better electronics (cheap and low noise preamplifiers) make it possible today to build silicon detectors with better than 10 μ m space resolution (III,10). In these detectors such an extreme resolution is reached when they operate as MWPC. This mode requires a very large number of readouts. Comparable resolution can also be reached exploiting a charge division technique, thus reducing the number of required electronics channels. Fig 10 illustrates the various modes of operation.

Capacitive or resistive couplings between adjacent electrodes can be obtained through deposition of thin metallic or amorphous layers on the surface of the semiconductor, or exploiting the behaviour of the intrinsic conductivity of the semiconductor itself. For example, assuming a uniform resistivity of the bulk material and

considering the ohmic contact, when the detector is operated with a bias slightly under the nominal depletion voltage, a thin surface layer of silicon between the strips remains undepleted and exhibits the proper resistivity of the crystal. Under such conditions it is possible to get a resistivity layer between the strips and the carriers cloud Q collected in the interstrip region is split between the two adjacent electrodes, namely i and $i+1$. Each electrode collects a charge inversely proportional to the distance from the track traversing the wafer and thus a point on the wafer itself is identified by the position (x_i, x_{i+1}) and the collected charges (Q_i, Q_{i+1}) of the fired electrodes:



The diagram shows a horizontal line representing a wafer. Two small black squares representing electrodes are placed on the line. The left electrode is labeled Q_i and the right electrode is labeled Q_{i+1} . An arrow points from the text (x_i, x_{i+1}) in the paragraph above to a point on the wafer between the two electrodes.

$$x = x_i + g \frac{Q_{i+1}}{Q_i + Q_{i+1}},$$

where g is the gap between two electrodes.

Detectors working in charge partition mode were successfully used in fixed target experiments at CERN and (to a lesser extent) at FNAL to identify B and D decay vertices (III,11).

There are several problems related to their use in colliding beam experiments.

We recall several of them:

- a) one should keep the multiple scattering to a minimum to do not to deteriorate the performance of the following tracking system,
- b) mechanical stability and positioning of the detector should be very accurate,
- c) a very large number of electronics channels is required.

Multiple scattering can be limited using very thin silicons and very light supporting frames. The CDF design utilizes silicons for a total amount of less than 1 % of radiation length. Despite of the very small weight of the silicons, the material of the frame could introduce too much multiple scattering. The use of special light materials (Rohacell, Kevlar) is planned for the SVX frames in CDF.

A third problem is related to the granularity needed for a good two-track separation and a good resolution. One must compromise between physics which would like an infinite two track separation and a resolution of a few microns and reason, which indicate that the system will become

unmanageable if the channels are too many.

We expect our choice to match both requirements. We should get a resolution of $\sim 25 \mu\text{m}$ and a two track separation of 200-300 μm (depending on the granularity of the layer, employing a total of about 16500 channels. So far a resolution of 22 μm was obtained with read-out strips 300 μm apart (fig.11)(III,12).

In tab 4 we show a comparison between silicon detectors and wire chambers. In tab 5 we show the choice made by a number of collider experiments.

The choice of the silicon was not univocal, and indeed it cannot be such at the present state-of-the-art. However we understand that the technology of the silicon detectors is in fast progress, as well as the associated electronics. Detectors with a finer granularity and a better spatial resolution than in our design are possible, and several projects are studying the possibility to incorporate on the same wafer the strips and the preamplifier of each channel. With this technology a larger number of channels could be handled, and a readout in r-z could possibly also be implemented, as well a finer granularity in the R- ψ coordinate.

The CDF vertex detector has been planned to measure impact parameters of charged tracks with a resolution of better than 100 μm , to perform the search for secondary vertices. It is composed of four layers of silicon strips arranged around the beam pipe (fig 12), inside the VTPC's. The detector can be split in two main part to allow an easier access to the wafers and the readout electronics. The total length of the detector is 67 cm. This is sufficient to match the length of the interaction region ($\sigma_z \sim 20 \text{ cm}$).

Each layer is shaped in a multisided polygon, first two layers (fig 12.a, 12.b) being octagonal and the others being dodecagonal. On each side of the polygons, twelve 5-cm long crystals are aligned in the z-direction.

The high resolution electrodes of six consecutive crystals are ganged together providing a 33 cm long cell. This microstrips, as discussed in detail in Chapter V, give the information in the R- ψ coordinate, which is needed to

measure the impact parameter of the tracks. On the rear electrodes, the crystal is split into approximate θ pads.

The geometrical parameters of the SVX are:

Lay.	cov (η)	r (cm)	thick. (μm)	z str. (#)	pitch (μm)
1	-3,3	2.94	200	112	200
2	-2.7,2.7	4.865	250	148	250
3	-2.4,2.4	6.79	250	140	250
4	-2.1,2.1	8.715	250	180	250

III.4 THE TRIGGER

The problem of CDF trigger is to pick up a few interesting events in a new energy domain, with an interaction rate of ~ 50 KHZ and a typical multiplicity of 50 charged particles per event.

The rate of interesting events is in general expected to be very low (often the more so the more interesting the events are) such that collecting all of them would be easy. However, since the data acquisition systems can afford a maximum rate of a few Hz, the trigger must be able to beat the background down to this rate without appreciable discrimination against interesting events.

The Trigger is designed as a three-level system. At each higher level more information is available and more checks are made. On each level the event can be rejected or passed to the higher level. We show in Tab 6 the expected rates and the selection performed by each level.

The level 1 trigger logic is interrogated on every beam-beam crossing.

Fast signals from the calorimeter towers and from the central and forward muon detectors are used to provide a rejection factor of about 90 % over the total cross-section and bring down the rate to the level of 5 kHz.

The level 1 decision is made before the next beam crossing (3.5 μ sec in a six-bunch scheme) so as not to intriduce any dead time.

Level 2 trigger is a topological trigger, i.e. at this stage the existence of clusters in the E.M./Hadron calorimeters is determined as well as the missing transverse energy. Large P_T tracks defined by CTC roads can be associated with calorimeter information to provide signals

for candidate electrons and muons. In general this multiple information enables the implementation of a set of trigger criteria based on the number and P_T of the jets, the presence of leptons, and the P_T unbalance of the event.

The level 2 trigger logic will reject most of the events in less than 7 μ sec. Since the rate from level 1 is ~ 5 kHz, the dead time introduced by level 2 is of the order of 3.5%.

If an event passes the level 2 selection, then the digitization process will be initiated and a complete event will be built and delivered to the level 3 system.

The level 3 system will be implemented as an array of processors having a total equivalent computing power of 20-50 VAX 11/780's, and will be capable of accepting an input rate of 100 ev/sec, selecting events based on a partial reconstruction.

The final output rate of events from level 3 must be of the order of 1 Hz, and all of them will be logged on tape.

III.5 THE SMALL ANGLE SILICON DETECTOR

In the very forward region several insertions of silicon detectors will be located inside the beam pipe (fig 13). The detectors of these insertions realize two magnetic spectrometers exploiting the bending magnets and the quadrupoles of the machine, and also include two hodoscope systems in front of the spectrometers.

These detectors will allow to measure:

- a) the elastic scattering differential cross section,
- b) the total cross section and the machine luminosity,
- c) the differential cross section for single proton diffraction: $p\bar{p} \rightarrow \bar{p} M$

The design of the crystals of each insertion was optimized to allow the silicons to operate as close as possible to the beam (fig 14) (III,13).

On the antiproton side, the momentum resolution will be $\Delta P/P = .1-.3$ %, with a corresponding resolution on diffracted mass $\Delta M/M \lesssim 10$ % for $M \gtrsim 200$ GeV.

On the proton side, the momentum of the recoiling proton, will be measured using the quadrupoles of the machine, and the resolution will be 10 times worse than that of the antiproton side.

Fig 15 shows the behaviour of $\Delta M/M$ as a function of M . These spectrometers offer unique physics opportunities for CDF, as discussed in III,13.

FIGURE CAPTIONS (Chap. 3)

- 1) CDF overview.
- 2) Layout of the central detector of CDF.
- 3) Layout of the forward spectrometer.
- 4) a) Energy resolution of the e.m. central calorimeter.
b) Energy resolution of the hadron calorimeter.
Both figures are preliminary results from the test beam. In fig. 4.b the resolution of the single hadron calorimeter (" uncorrected ") and final resolution after taking into account the energy released in the e.m. calorimeter (" corrected ") are shown.
- 5) Endplug projective geometry.
- 6) a) Endplate of the Central Tracking Chamber.
b) Magnified view of the axial wires superlayers.
- 7) Pictorial view of a high p_T muon traversing the CTC.
- 8) Isometric view of a VTPC module.
- 9) Overview of the Radial Drift Chamber.
- 10) Silicon detectors :
 - a) operating as a MWPC,
 - b) operating in capacitive charge division,
 - c) operating in resistive charge division.
- 11) Resolution of a silicon detector operating in resistive charge division (III,11)
- 12) Layout of the CDF silicon detector:
 - a) open view,
 - b) cross-section
- 13) Layout of the small angle spectrometers.
- 14) Silicon crystals of the insertions S4 and S5.
- 15) $\Delta M/M$ for diffractive events, as a function of M.

TABLE 1 A
CENTRAL CALORIMETER
ELECTROMAGNETIC

	SCINTILLATOR		WIRE CHAMBERS
GRANULARITY	ANGULAR COVERAGE	LAYERS	chamb locat
	$ \eta \leq 1.1$	33	$\approx 5.7 \times^\circ$
$\Delta \eta \approx 11, \Delta \varphi \approx 15^\circ$	$36 \leq \theta \leq 144$	$(19.8 \times^\circ)$	
	$0 \leq \varphi \leq 2\pi$		

	SCINTILLATOR		WIRE CHAMBERS
$\frac{\sigma(E)}{E}$	$15\% / \sqrt{E}$		
σ_y	$7 \text{ cm} / \sqrt{E}$		$\pm 3 \text{ mm}^*$
σ_z	$7 \text{ cm} / \sqrt{E}$		$\pm 5 \text{ mm}$
			$\pm 3 \text{ mm}$

Hadron rejection: $\geq 10^3$

2 γ separation $\approx 5 \text{ cm}$

HADRON

	ANGULAR COVERAGE	LAYERS
GRANULARITY	$ \eta \leq 1.0$	34
$\eta \approx 11, \Delta \varphi \approx 15^\circ$	$40^\circ \leq \theta \leq 140^\circ$	$(5 \wedge \text{ abs})$
	$0 \leq \varphi \leq 2\pi$	
$\frac{\sigma(E)}{E}$	$(5.5+62)\% / \sqrt{E}$	
σ_y	$\approx 5.4 \text{ cm}$	

* beam test results

TABLE 1 B

END WALL HADRON CALORIMETER

GRANULARITY	ANGULAR COVERAGE	LAYERS
$\Delta\eta \approx .15, \Delta\varphi \approx 15^\circ$	$.8 \lesssim \eta \lesssim 1.3$	15 (.75 m Fe)
	$30^\circ \lesssim \theta \lesssim 150^\circ$	(4.4 Δ abs)
	$0 \leq \varphi \leq 2\pi$	
	SCINTILLATOR	
$\frac{\sigma(E)}{E}$ σ_γ	100% / $\sqrt{E} (*)$	
	≈ 7 cm	

TABLE 2

END PLUG CALORIMETER

ELECTROMAGNETIC

GRANULARITY	ANGULAR COVERAGE	LAYERS	CHAMB. POSIT.
$\Delta\eta \approx .11, \Delta\varphi \approx 5^\circ$	$1.1 \leq \eta \leq 2.3$ $11^\circ \leq \theta \leq 37^\circ$ $0 \leq \varphi \leq 2\pi$	30 (21.0 X ^o)	6. X ^o $1.1 \leq \eta \leq 1.7$ $2^\circ \leq \theta \leq 37^\circ$

HADRON

GRANULARITY	ANGULAR COVERAGE	LAYERS
$\Delta\eta \approx .10, \Delta\varphi \approx 5$	$1.3 \leq \eta \leq 2.4$ $10^\circ \leq \theta \leq 30^\circ$ $0 \leq \varphi \leq 2\pi$	20 (1 m Fe) (6 \wedge abs)

$\frac{\sigma(E)}{E}$	Electromagnetic	Hadron
$\sigma_\varphi \sim \sigma_\eta$	$\approx 30\% / \sqrt{E}$ * $= 3 \text{ mm}$	$100\% / \sqrt{E}$ $1 \div 1.5 \text{ cm}$

Hadron rejection (e.m. calorimeter): $\geq 10^3$

* test beam results

TABLE 3

Fractions of fake muons

P_{\perp} (GeV)	DECAY + PENETRATION
10	$(6.6 + 1.6) 10^{-3} = 8.2 10^{-3} = 1/120$
20	$(3.3 + 1.6) 10^{-3} = 5. 10^{-3} = 1/200$
30	$(2.2 + 1.6) 10^{-3} = 3.8 10^{-3} = 1/260$
50	$(1.3 + 1.6) 10^{-3} = 2.9 10^{-3} = 1/350$

TABLE 4

	wire chambers	silicon detectors
δx	$\approx 30 \mu m$	$\approx 5 \div 20 \mu m$
2-track res.	$\approx 200 \mu m$	$\approx 50 \div 150 \mu m$
Multiple scattering contribution		
(X/X^0)	$\approx .5 \%$	$\approx 1-2 \%$

TABLE 5

experiment	vertex detector
UA1	Wire Chamber
UA2	Wire Chamber
CDF	Si
DO	Wire Chamber
ALEPH	Si
DELPHI	Si
OPAL	Si
SLD	Si

Wire Chamber = High pressure drift chamber; Si = Silicon
detector

TABLE 6

LEVEL	INFORMATION	DECISION TIME	INPUT RATE	DEAD TIME
I	beam crossing			
	beam-beam counters			
	barrel counters	3.5 μ sec	50 KHz	0 %
	number of calorimeter			
	tower over threshold			
	total E_{\perp}			
II	a) energy clusters	7 μ sec	5 KHz	3.5 %
	b) track matching	20 μ sec	1.5 KHz	3.0 %
III	Full readout	1 msec	100 Hz	10%

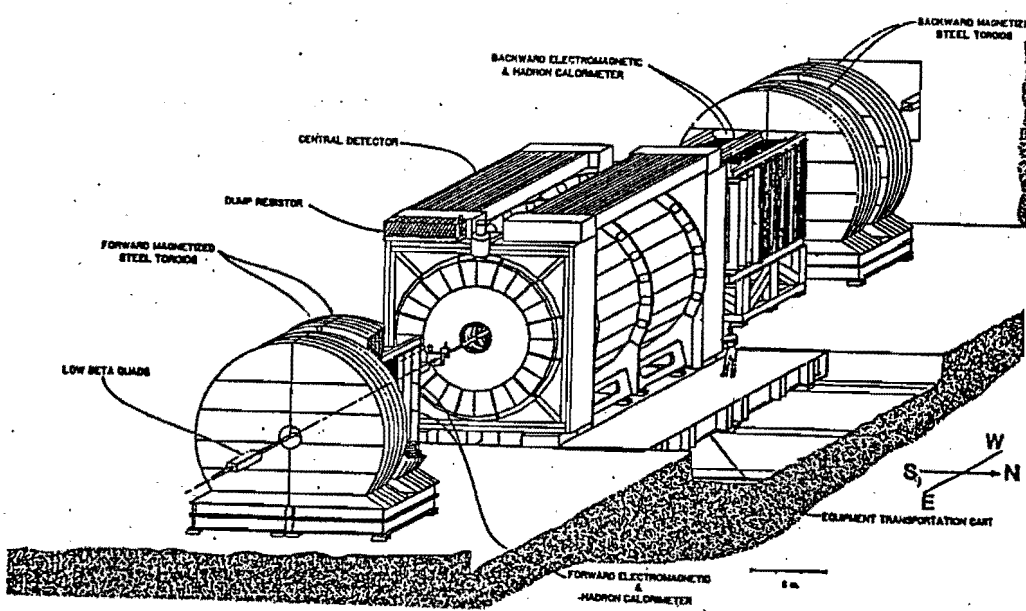


Fig 1

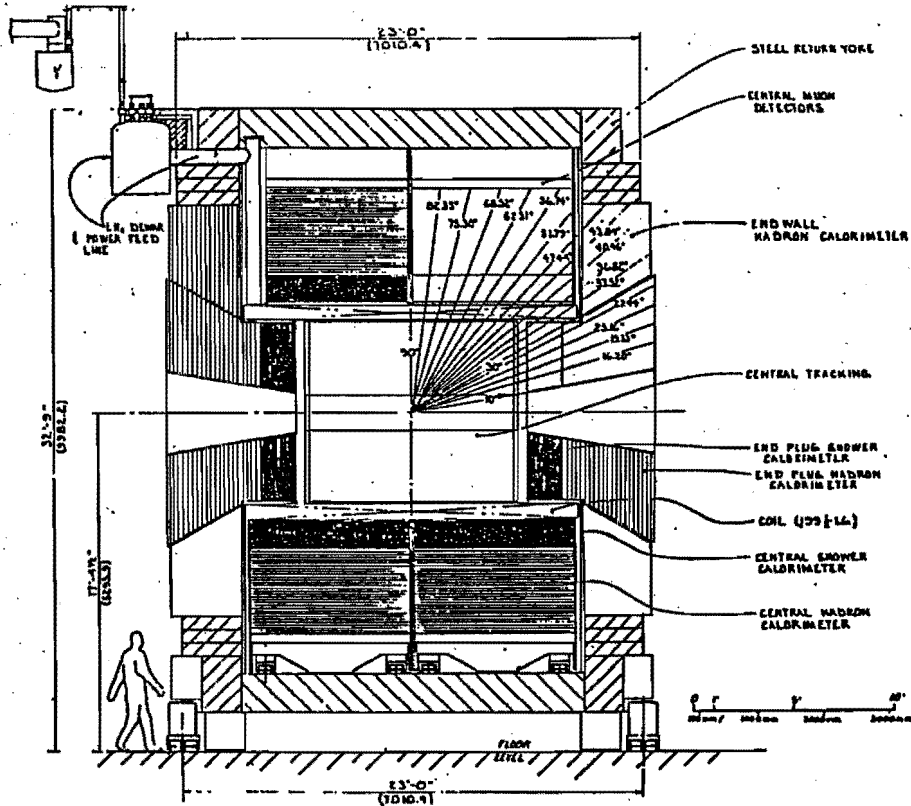


Fig 2

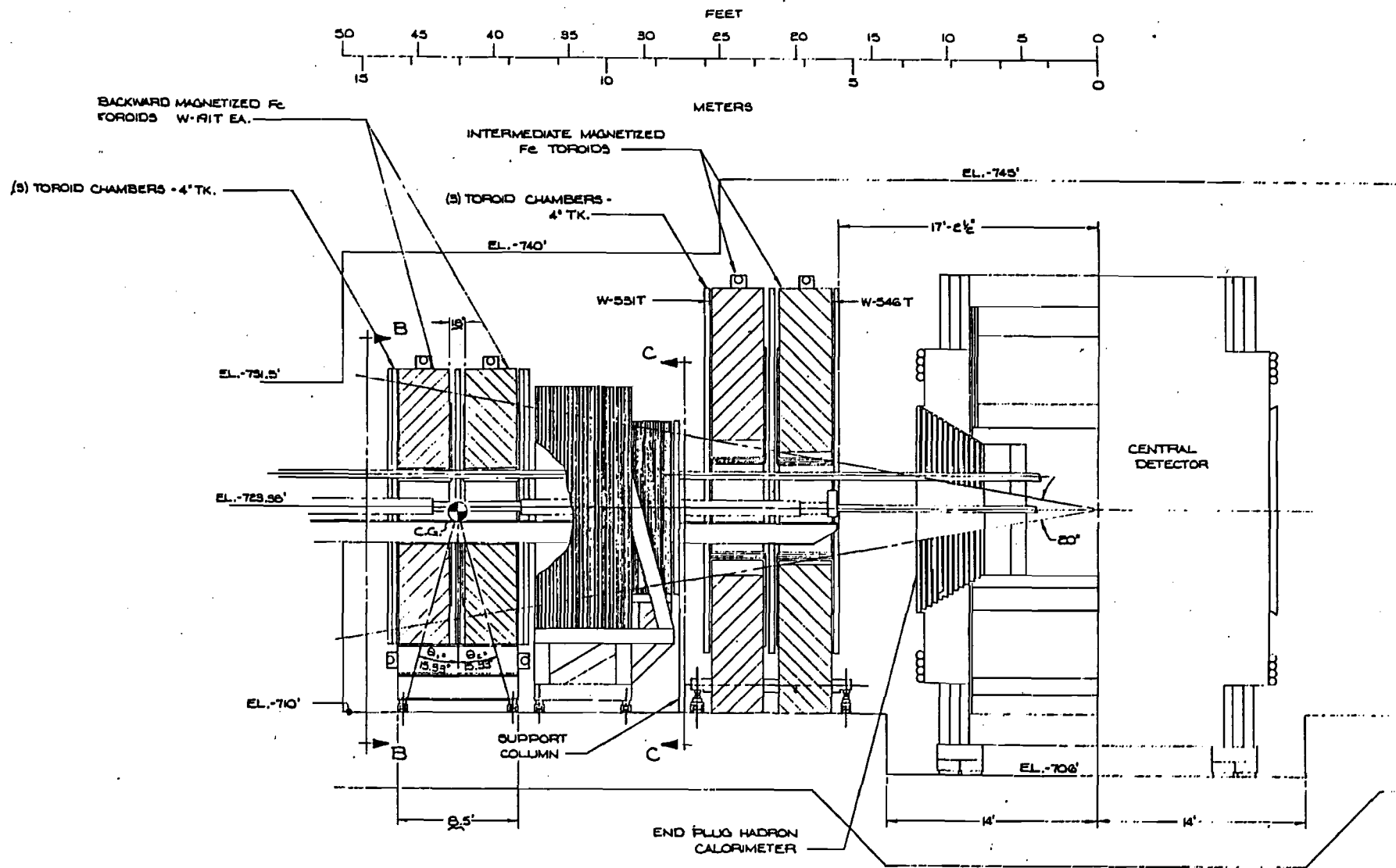
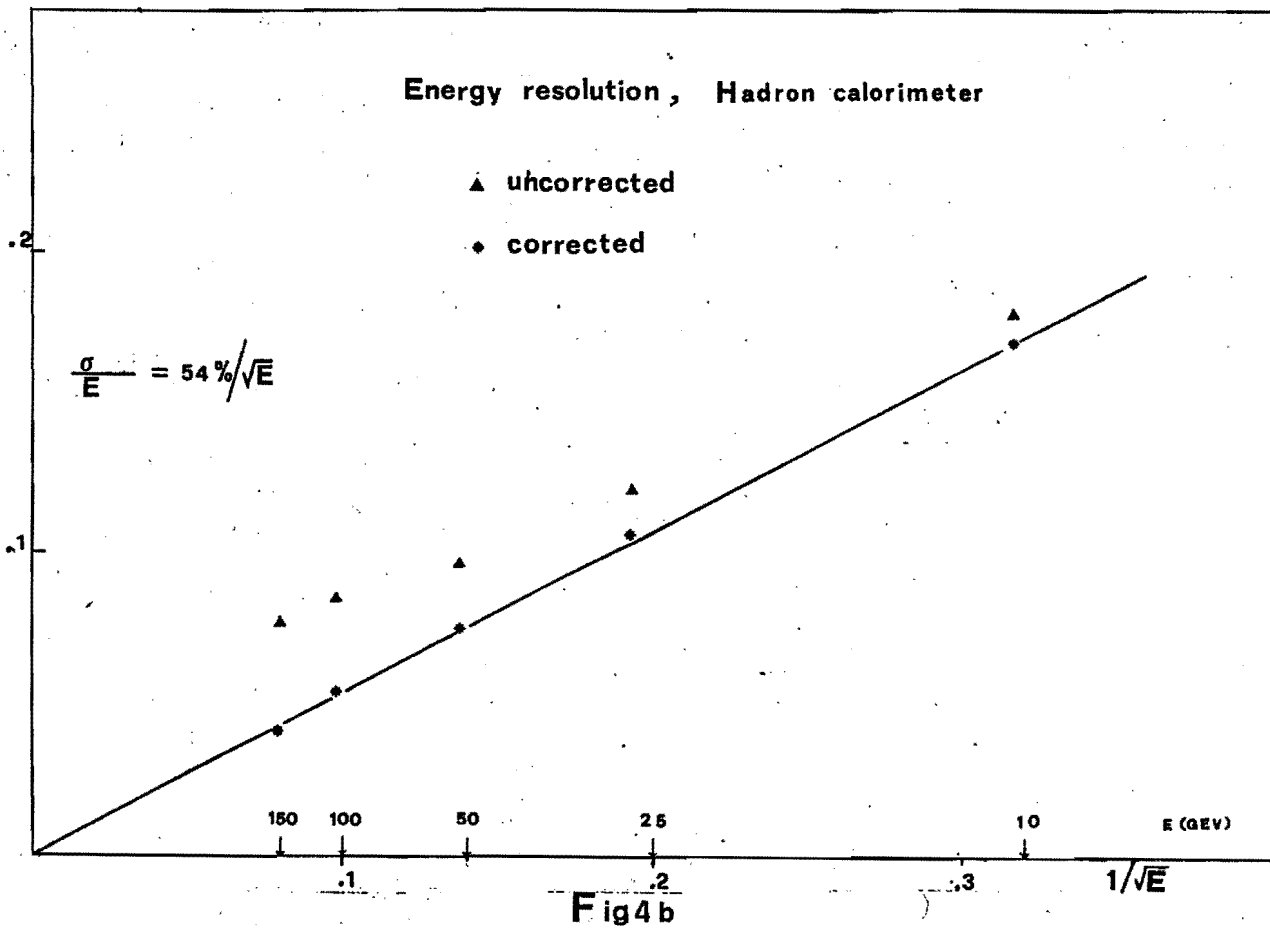
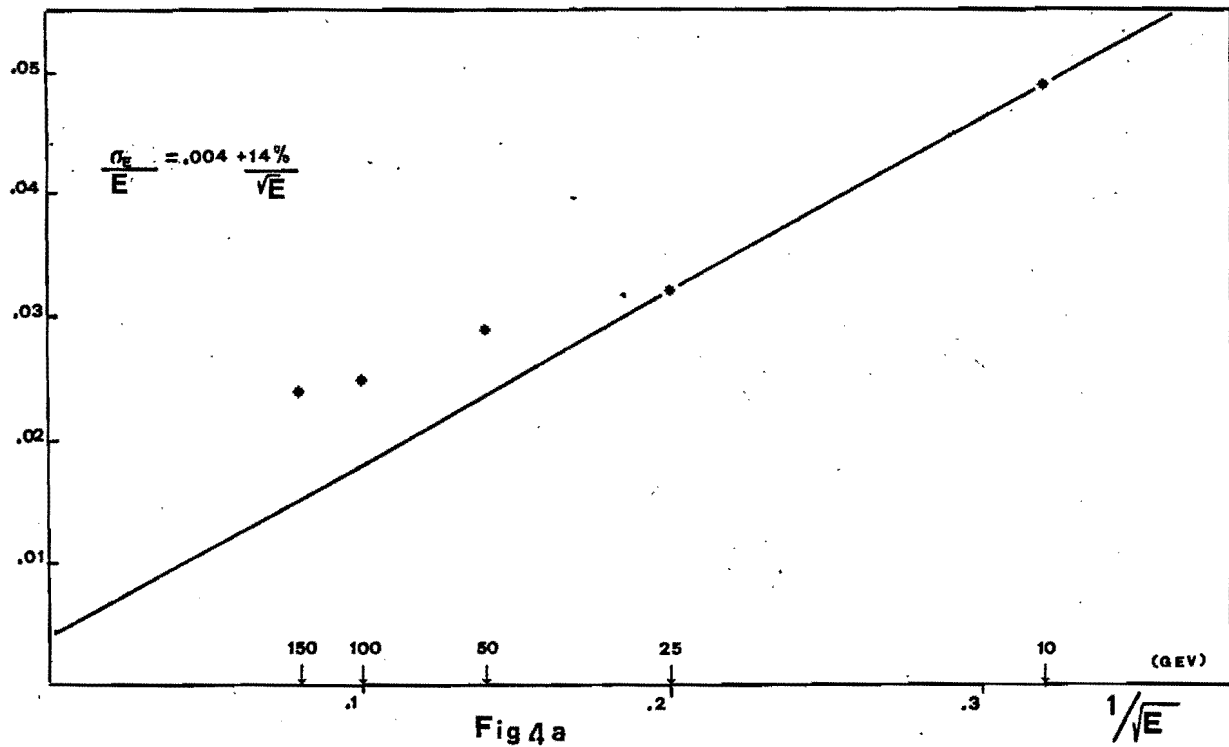


Fig 3



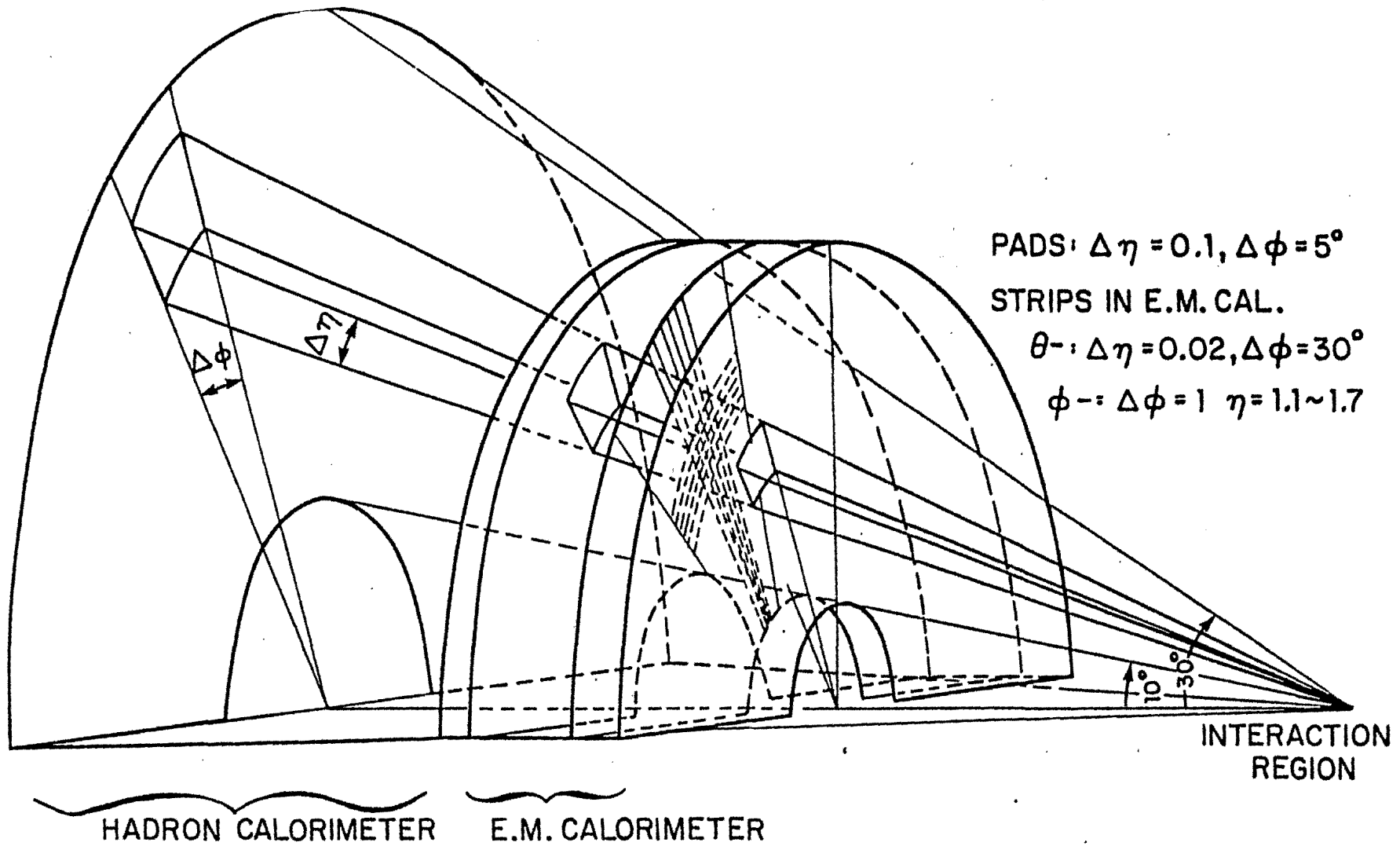


Fig 5

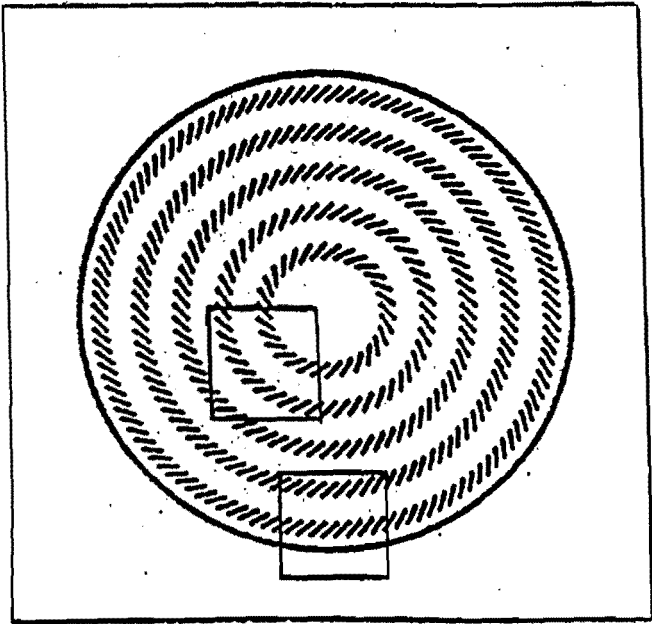


Fig 6 a

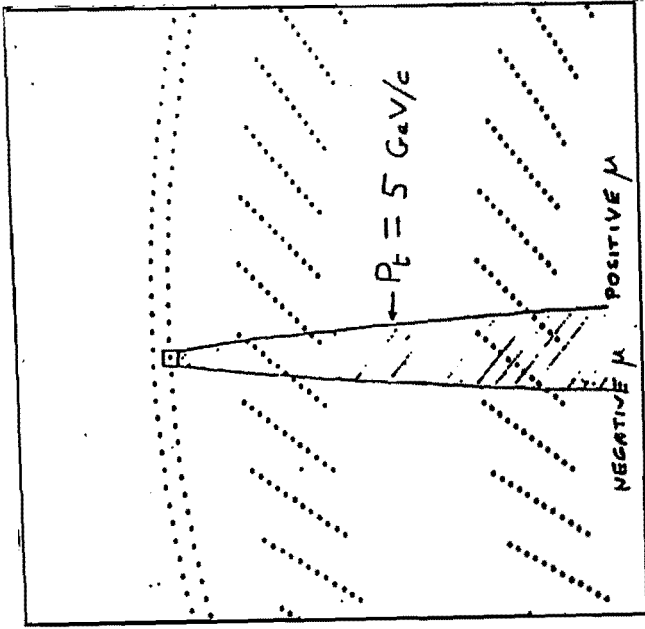
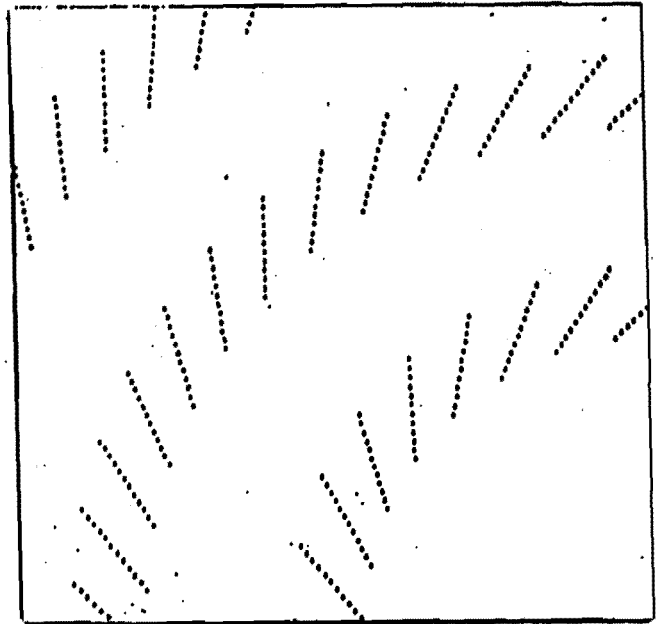
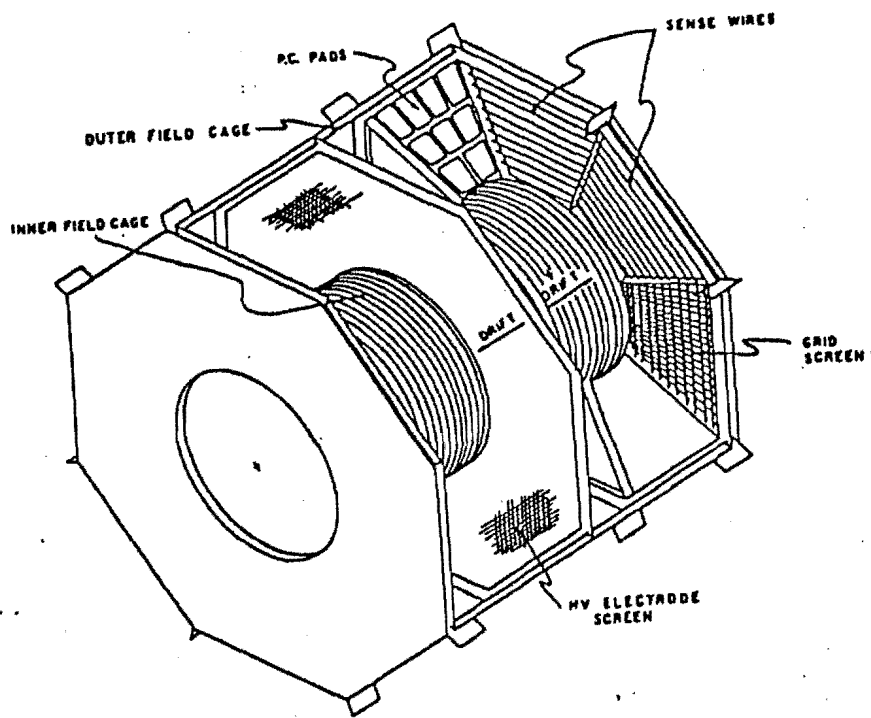


Fig 7



6 b



VTPC Module

Fig 8

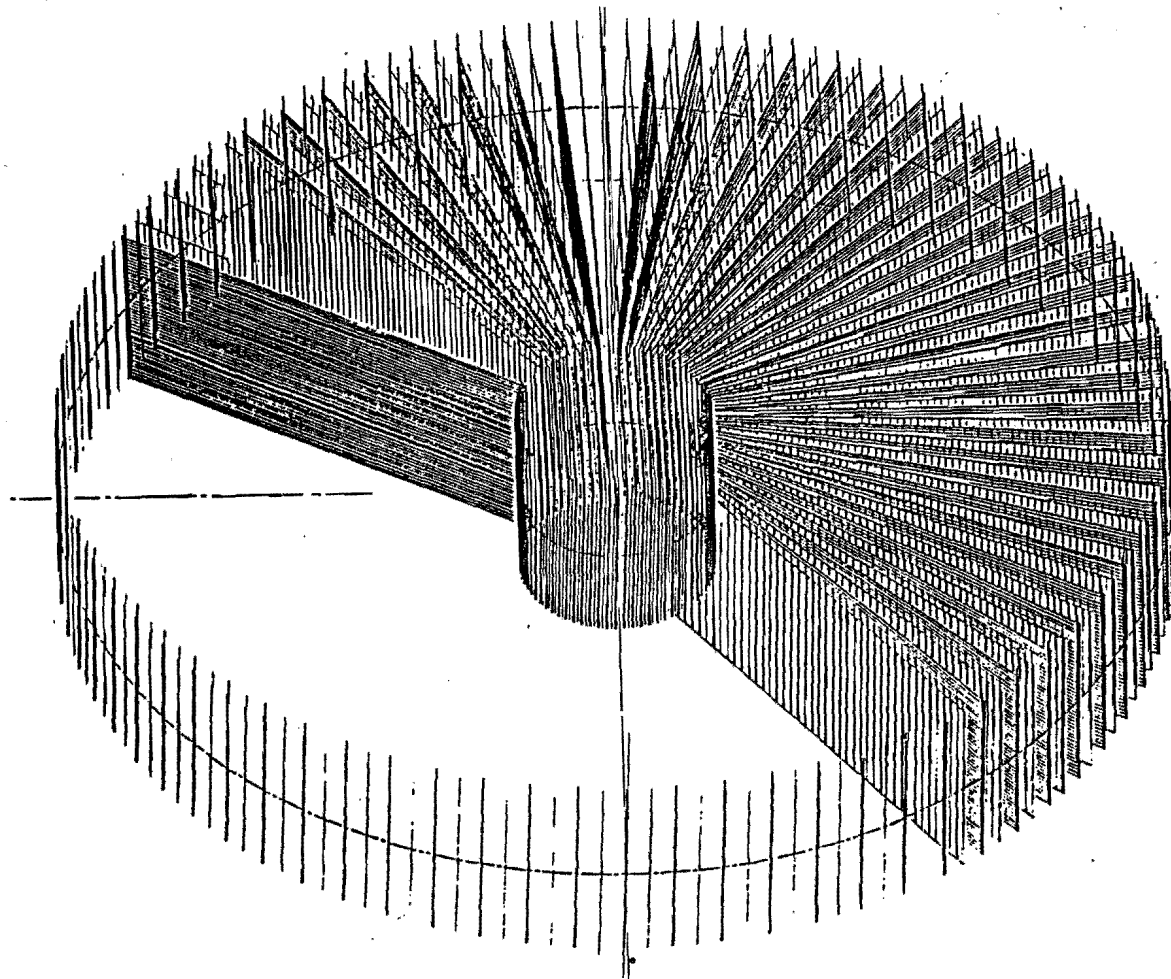
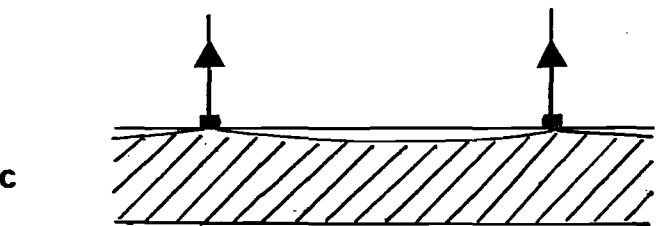
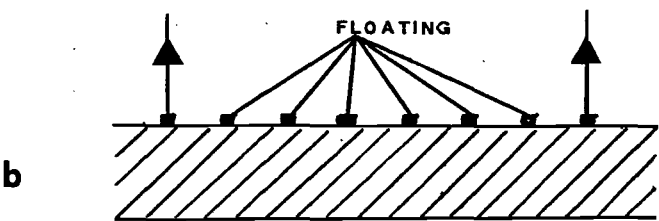
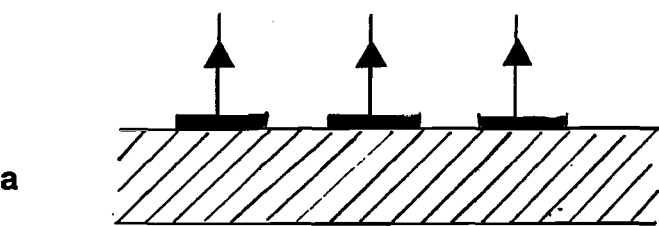


Fig 9



→ PREAMPLIFIER

▨ DEPLETED REGION

Fig 10

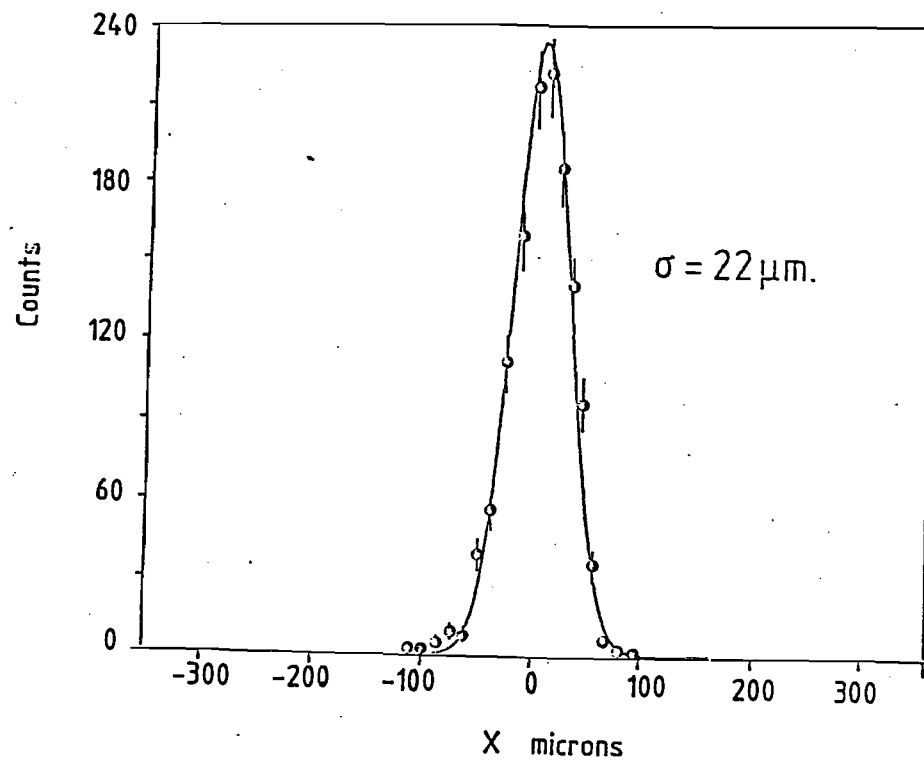


Fig 11

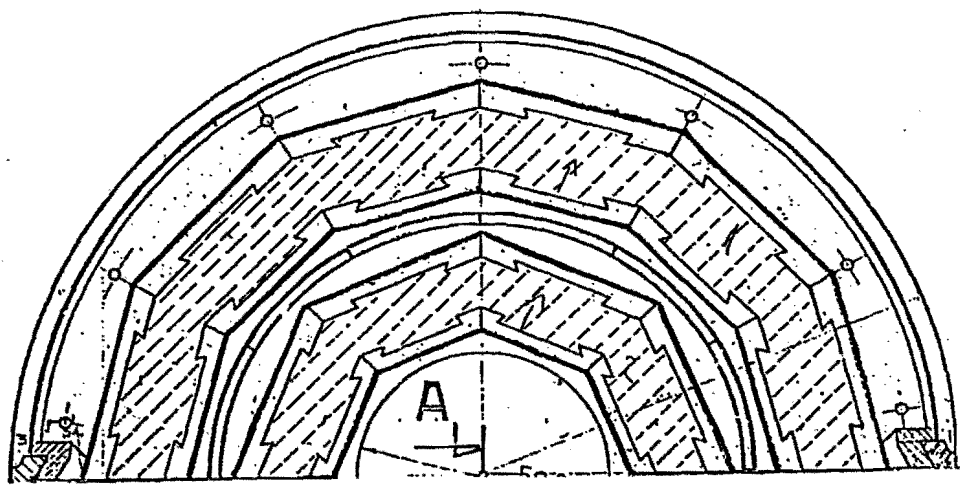
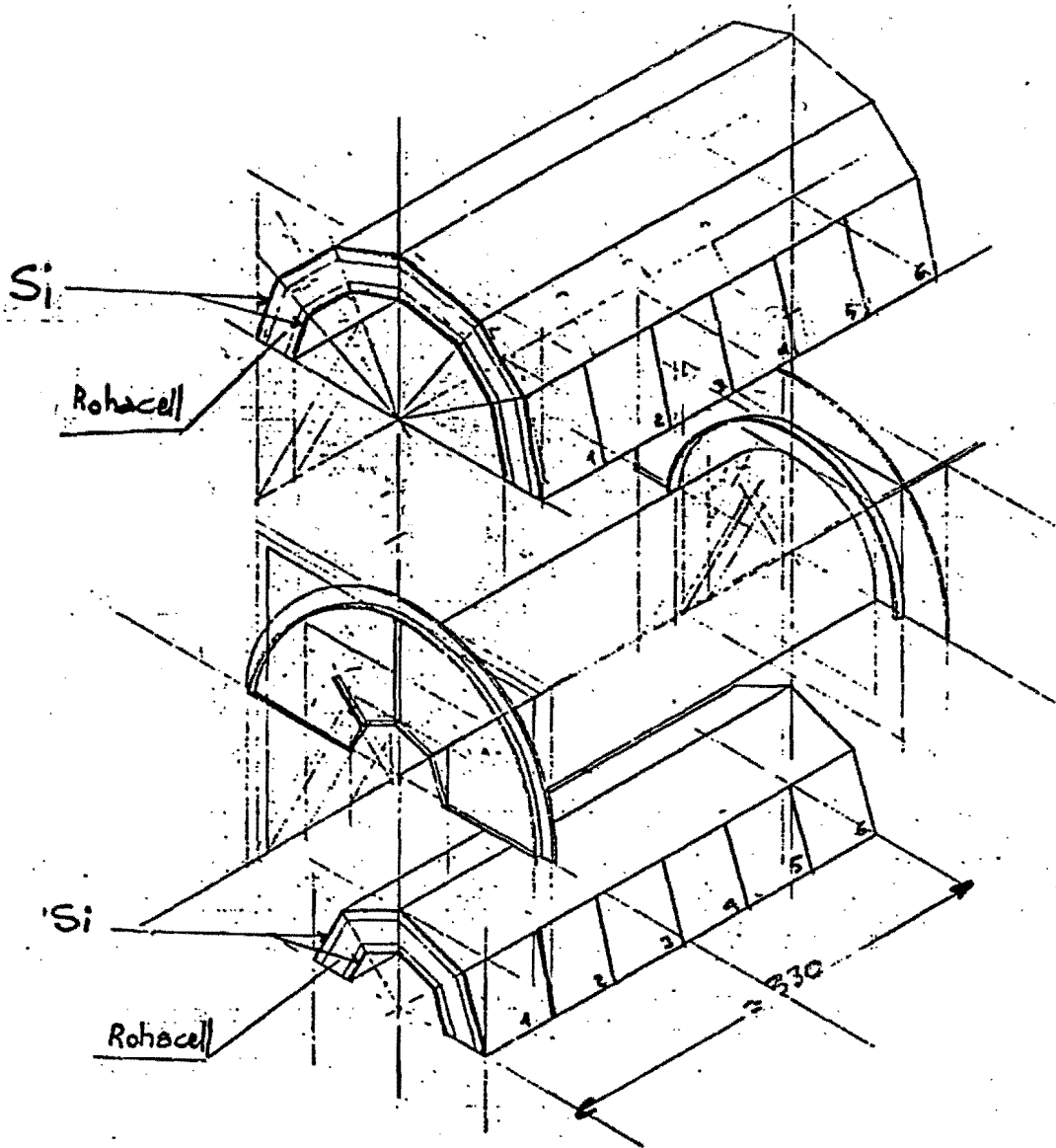


Fig 12

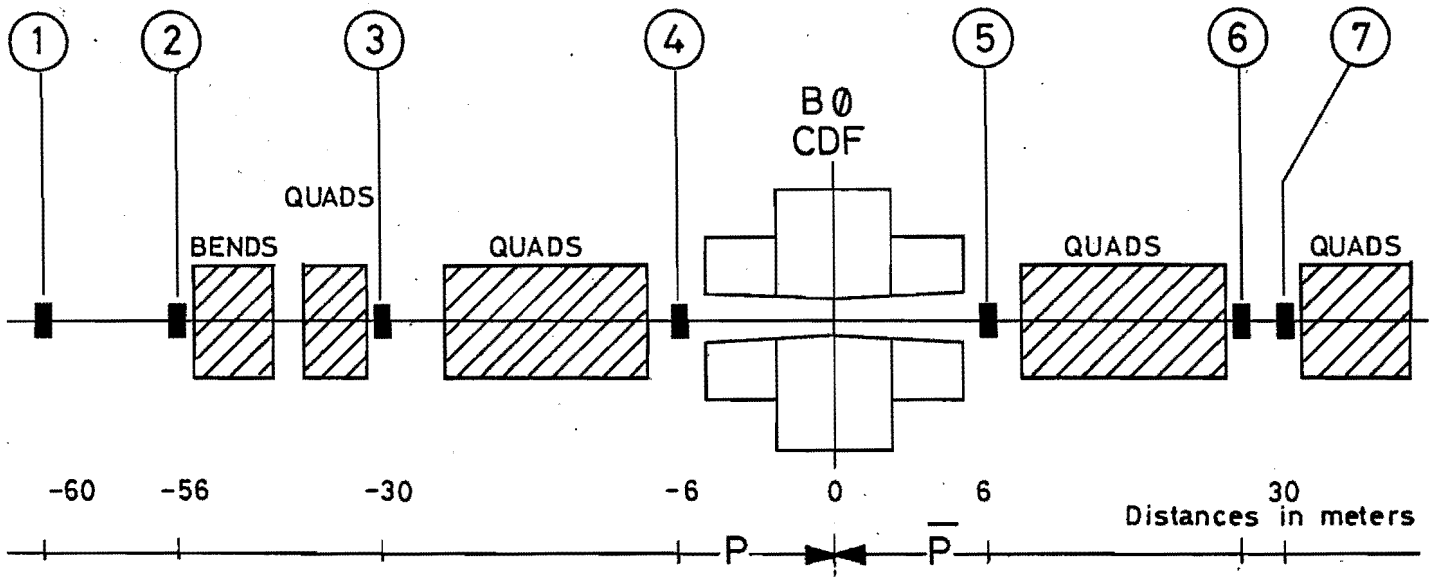
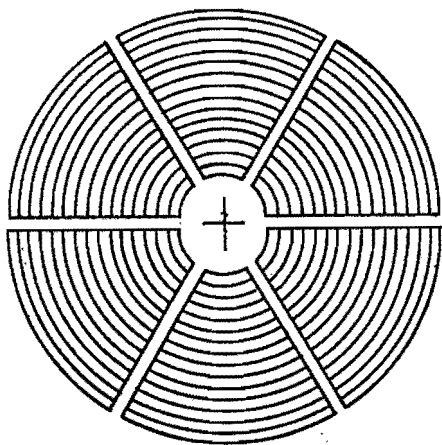
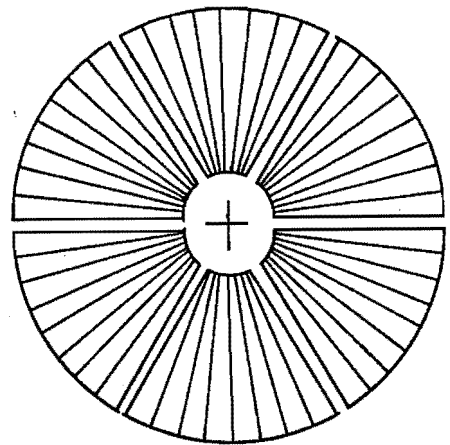


Fig. 13

S_4 S_5 "petals"



FRONT



REAR

Fig.14

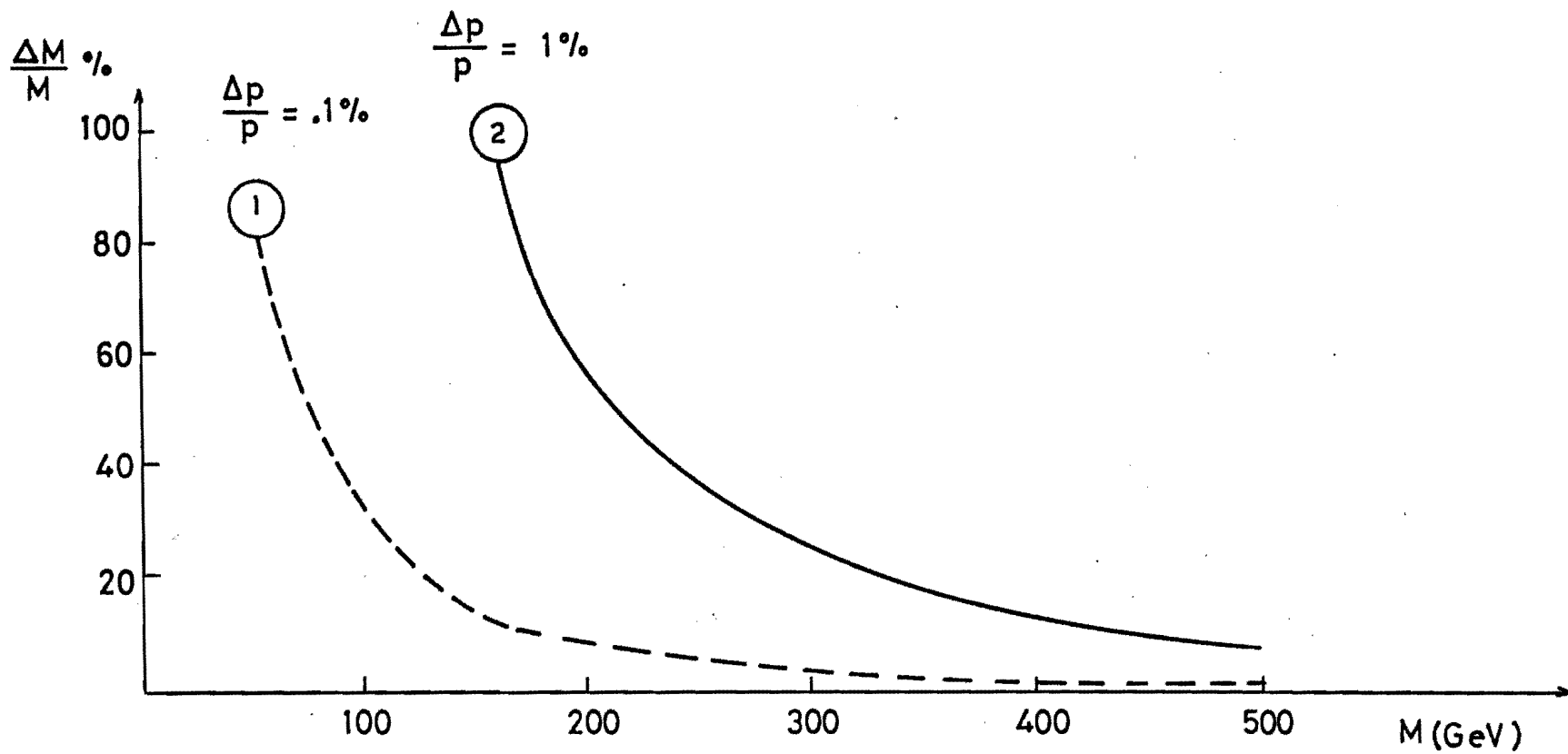


Fig.15

CHAPTER IV

ESTIMATED DETECTOR PERFORMANCES

In Chapter II we discussed a number of important measurements to be performed with CDF, including the search for new possible phenomena in the new energy domain of Tevatron I. It is important to assess the capability of CDF to detect jets and leptons and measure their parameters since jets and leptons play an essential role in all these phenomena. We briefly report in this Chapter the results of a number of detector simulation studies to determine the CDF capability to tag electrons and muons and measure their energy and to reconstruct energy and direction of jets, and to measure missing transverse energy.

Another important quality factor of CDF, its ability to tag the heavy jet flavour, will be dealt with in the next Chapter.

IV.1 ELECTRON IDENTIFICATION

The identification of electrons relies on the combined information of the tracking system and of the electromagnetic and hadron calorimeters. A large P_T candidate electron will be signalled by a) a stiff charged track pointing to the tower, b) an energetic cluster in the E.M. sector of a calorimeter tower, and c) little energy deposited in the hadronic sector. To reject single charged hadrons the following requests are made:

- a) the energy deposited in the e.m. shower counters must be consistent with the momentum measured by the CTC, viz. $E/p \approx 1$. This can be done to within the detector energy and momentum resolutions, $\sigma(E) = 15\% \cdot \sqrt{E}$ and $\sigma(p_T)/p_T = 10^{-3} \cdot p_T$,
- b) an early development of the shower, i.e. large signals in the wire chambers located at $5.7 X^0$,
- c) little energy penetrating the hadron calorimeter.

Using cuts a) and b) a rejection of $\sim 5 \cdot 10^3$ was obtained against pions at 30 GeV (fig 1) on the test beam (IV,1). In the experiment a number of effects like the presence of the coil, a non-perpendicular impact direction of the track in the calorimeter, etc. will degrade somewhat this performance. However a preliminary analysis of the test beam data (1984), with a fake coil in front of the shower counters, confirms that a rejection power of $\sim 10^3$ can be obtained for 30 GeV pions.

The identification of electrons close to large hadronic

clusters of is a more difficult problem. The size of the hadron tower ($\Delta\varphi = 15^\circ$, $\Delta\eta = 0.11$) (fig.2) gives an estimate of how the electrons must be far from the edge of a jet in order to be separable.

IV.2 MUON IDENTIFICATION

Muons are recognized as charged particles traversing with minimum ionization the whole calorimeter and leaving a signal in the outer muon chambers. A candidate muon must satisfy the following requests:

- a) a signal corresponding to a minimum ionizing particle in the calorimeter,
- b) a match between the track reconstructed in the outer μ chambers and the position of the track inside the calorimeter. This position is determined within the size of tower pads at $\theta \leq 40$. At large angles one can do better than the tower size in one direction by studying the relative pulse height of the two photomultipliers viewing the same tower,
- c) a match between the track reconstructed in the outer chambers and the track reconstructed in the CTC.

Because of the finite thickness of the calorimeters, pions have a finite probability of crossing them without interacting ("punch-throughs"). This phenomenon constitutes one of the main sources of background. The other main source is π, κ decay in flight: $\pi \rightarrow \mu \nu$, $\kappa \rightarrow \mu \nu$ which generate unbeatable muons unless a "kink" is discovered off-line in the reconstructed trajectory. In the present CDF the two sources of background are comparable, as seen in the following table:

P_T (GeV)	decay+penetration	(probability)
10	$(6.6 + 1.6) 10^{-3}$	$= 8.2 \cdot 10^{-3} = 1/120$
20	$(3.3 + 1.6) 10^{-3}$	$= 5. \cdot 10^{-3} = 1/200$
30	$(2.2 + 1.6) 10^{-3}$	$= 3.8 \cdot 10^{-3} = 1/260$
50	$(1.3 + 1.6) 10^{-3}$	$= 2.9 \cdot 10^{-3} = 1/350$

Although these factors are insufficient for a measurement of inclusive production of direct muons, they still represent a useful handle to exploit the muon signature in special events. It should be observed that most of these muons are isolated while the expected rate of isolated large P_T charged hadrons is about 1/4 of the inclusive large P_T

hadron rate.

The detection of muons inside a jet is also possible if detailed information is collected on the development of the muon + shower system (IV,2). The possibility of doing this in CDF in the region covered by gas calorimeters is at present under study.

The triggering rate on single muons at large P_T may also be a problem. With a μ/π ratio of $2 \cdot 10^{-4}$ at 90° , the triggering rate would be dominated by background for any P_T cut. Again, one will exploit the level II trigger to collect events showing also additional significant signatures on top of a candidate muon. This will allow to reduce the trigger rate to acceptable values.

IV.3 JET DETECTION

The identification of energy clusters inside the calorimeters is performed by the level II trigger. Several studies were made to understand the capability of our calorimeter to reconstruct the energy and direction of jets.

For these studies the CDF Monte Carlo was used (IV,3). In this package the detector geometry including cracks, non uniformities etc., as well as the most important physical effects (de/dx, multiple scattering, in flight decays, conversions, punchthroughs, spread of the interaction region) are simulated. Also, the shower development and the different response of the calorimeters to e.m. and hadronic showers, as measured at the test beam, are considered.

Fig 3 shows the fraction of detected/generated energy as a function of η . Some loss of response in the cracks at $10^\circ, 38^\circ$ (e.m.), 30° (had.) and 90° is clearly visible (fig 3.a 20 GeV e^- , fig 3.b 20 GeV π). In fig 4 the response to 20 GeV electrons as a function of theta is plotted. Again one can notice modest effects due to the cracks between towers. An average resolution $\sigma(E)/(E) = 15\%/(E)^{1/2}$ is obtained.

The resolution in jet-jet invariant mass was computed to be $\sim 10\%$ for masses of about 80 GeV (fig 5) and 4.9% for $M=500$ GeV. The energy dependence of the resolution is due in part to the energy dependence of the errors made in the cluster search, like wrong assignments of beam particles to a jet, or conversely loss of low P_T tracks belonging to a

jet. Both of these sources of errors are more effective at 80 GeV than at 500 GeV. This effect is clearly seen in fig. 5.b, where the jet-jet mass resolution corresponding to a perfect clustering has a f.w.h.m. of 14 %, while the curve for the same M, but including the effects of a real clustering has a f.w.h.m. of 18 %.

In both cases the assumed energy resolution of the calorimeter system was $\sigma(E) = 55\% \cdot (E)^{1/2}$. As a comparison, we mention here that a detailed study of the performances of an Argon-Uranium calorimeter, gave a resolution for $M_{jj} = 80$ GeV better than in CDF only by a factor 1.3 (IV,4). At 500 GeV, where the intrinsic energy resolution of the calorimeters is more important, the resolution in M_{jj} is about 2.4 times better than CDF, i.e. $\Delta M/M = 2\%$. At present several cluster algorithms are carefully studied to exploit at best both the projective geometry and the information carried by the energy released in the various tower elements. Preliminary results (IV,5) are rather encouraging, showing that it should be possible to reconstruct multijet events in a large fraction of cases (Tab.1).

IV.4 MISSING E_T RESOLUTION

Missing transverse energy is a distinct signature of many important processes expected in both the SM and in the New Physics (cfr. Chapt.II). It is important therefore that missing E_T be measured with high precision by CDF.

Effects which contribute to deteriorate the \cancel{E} resolution are:

- a) cracks in the apparatus,
- b) the 2° holes,
- c) intrinsic calorimeter resolution.
- d) muons

In fig 6 we show the \cancel{E} resolution expected for CDF as a function of the size of the small angle hole. Effects a), c) and d) were properly taken into account. In fig 7 the different contributions are plotted separately. For $\cancel{E} \approx 25$ GeV the curve shows that the missing E_T is essentially due to μ 's and ν 's escaping from the calorimeter. Below 15 GeV the intrinsic resolution of the calorimeters is the main source of error on \cancel{E} . The intrinsic resolution is also

important for $15 \lesssim E_T \lesssim 25$ GeV.

A visual scan of the events with $E_T \geq 15$ GeV showed that several of them have charged tracks pointing to a crack or clearly containing identifiable muons. For these events an easy and effective offline corrections is possible (IV,6) We conclude that in average we expect in CDF a missing E_T resolution $\sigma(E_T) = .85 * (E_T^{1.5})$. Our simulation leads us to predict that the 2° holes do not affect too much the resolution.

Tab 1

% of reconstructed clusters

		rec	0	1	2	3	4	5
		gen						
P_T 20÷40 GeV	2		2	3	85	9	1	
	3		2	2	35	57	4	
P_T 40÷80 GeV	2		1	0	80	18	1	
	3		1	0	19	67	12	1
	4		1	0	4	33	51	11

FIGURE CAPTIONS (Chap. 4)

- 1) Probability for pions of 10 and 30 GeV to be misidentified as electrons, for a 5 % and a 10 % of electron inefficiency as a function of the cut on the early development of the shower.
- 2) Granularity of the hadron calorimeter.
- 3) Reconstructed/generated energy as a function of η :
 - a) 20 GeV e^-
 - b) 20 GeV π^-
- 4) Energy resolution of the calorimeter as a function of η .
- 5) Resolution in invariant mass of two jets, for $M_{jj} = 80$ GeV.
- 6) E_T missing resolution as a function of the hole in the apparatus, for 15 GeV (a) and 50 GeV (b) jet events.
- 7) E_T missing distribution for CDF (upper curve). The lower curve shows the contribution from μ, ν only.

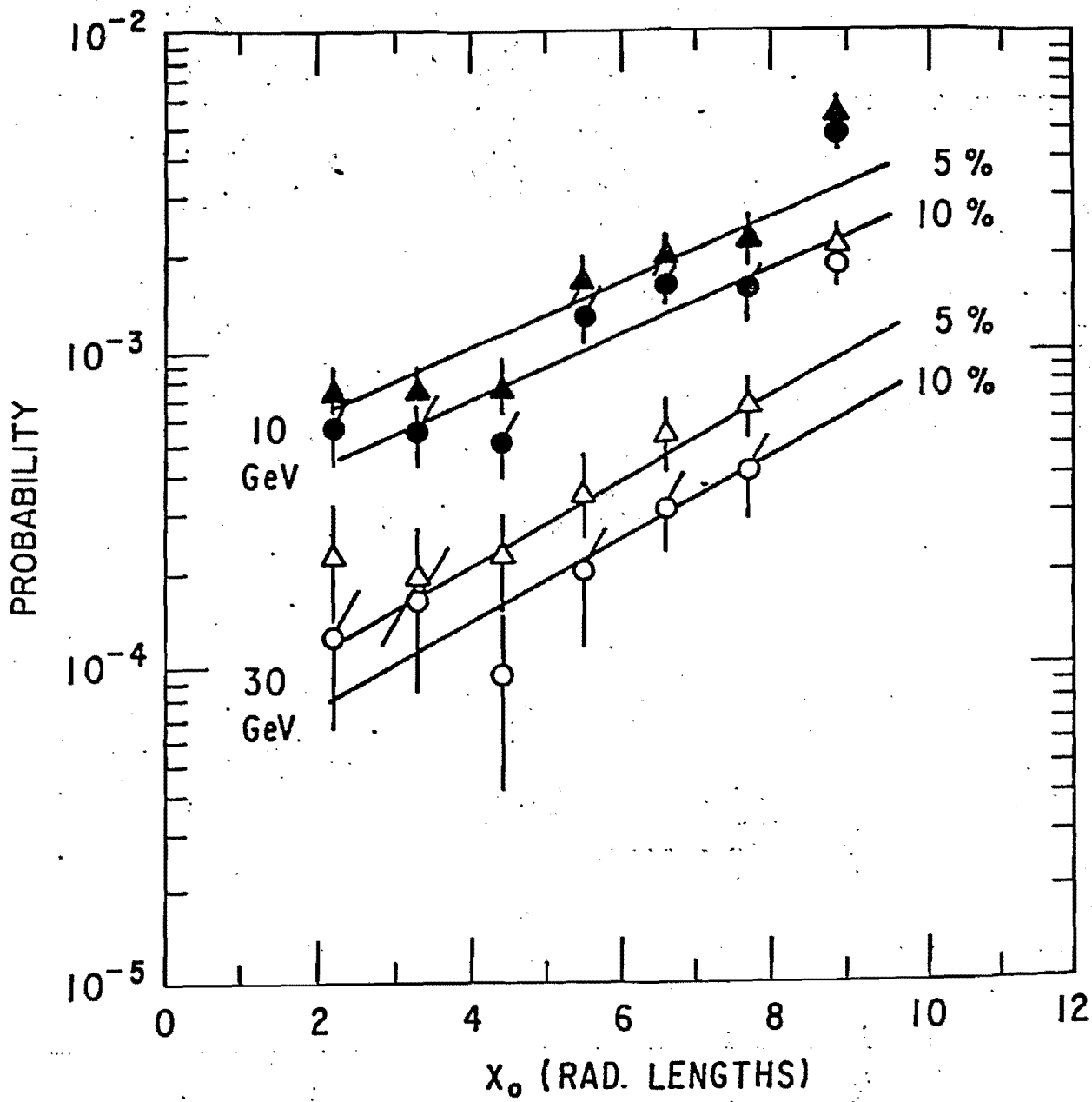


Fig 1

CDF GRANULARITY IN HADRON CALORIMETERS

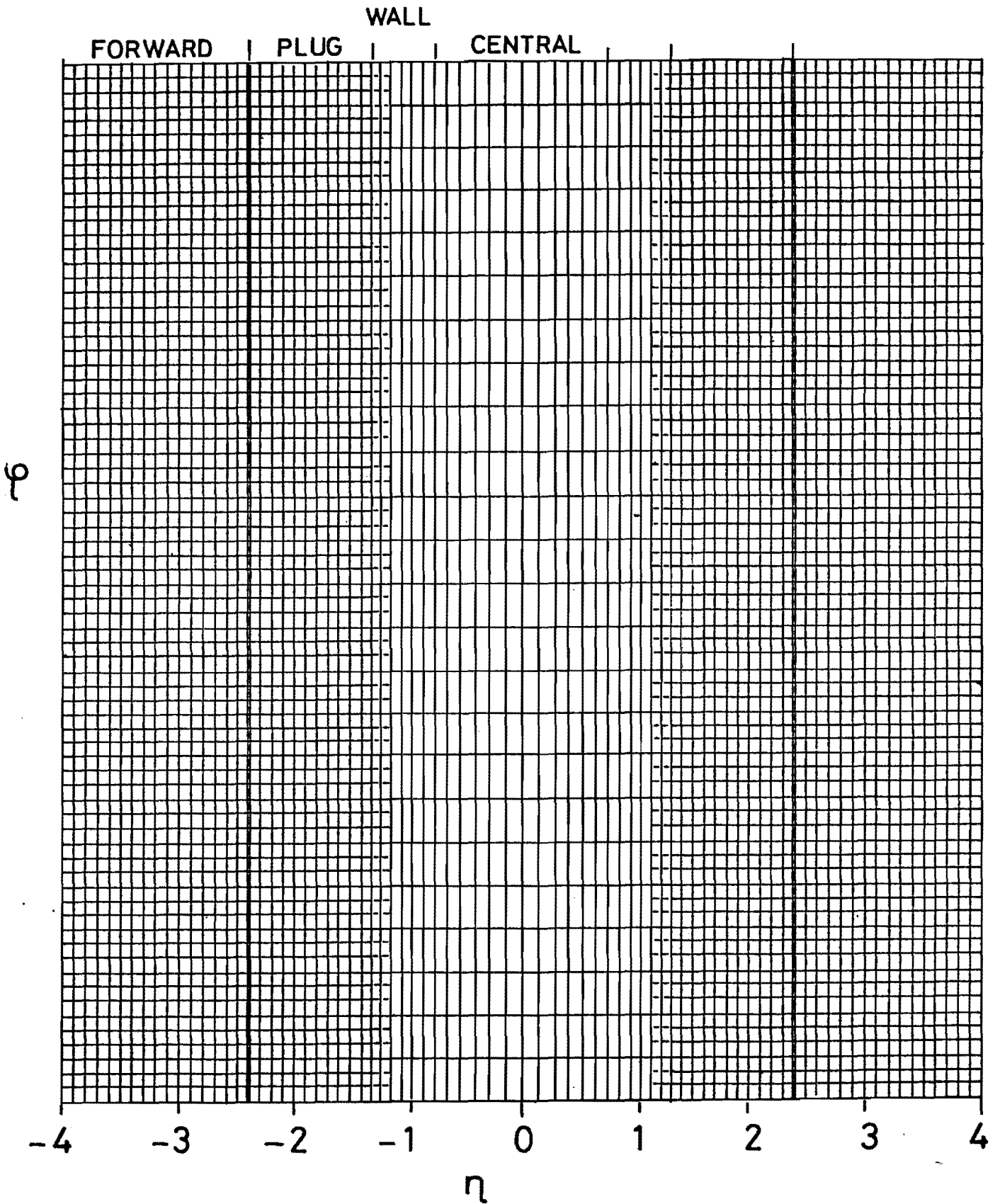


Fig. 2

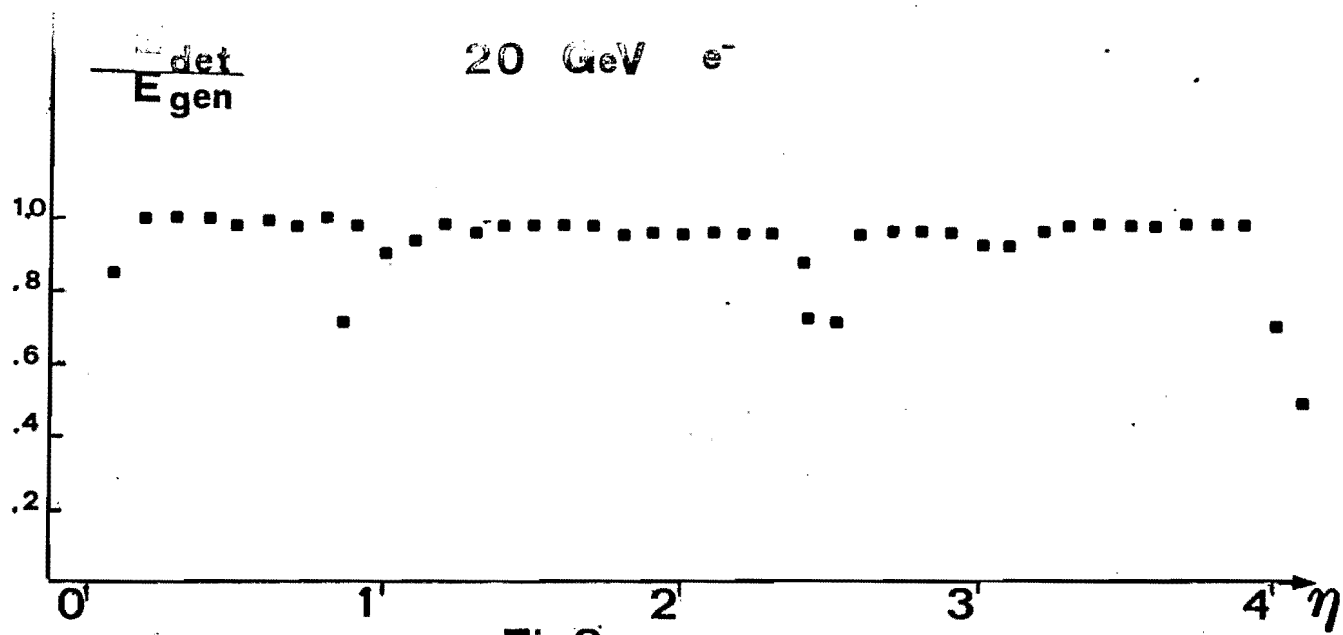


Fig 3 a

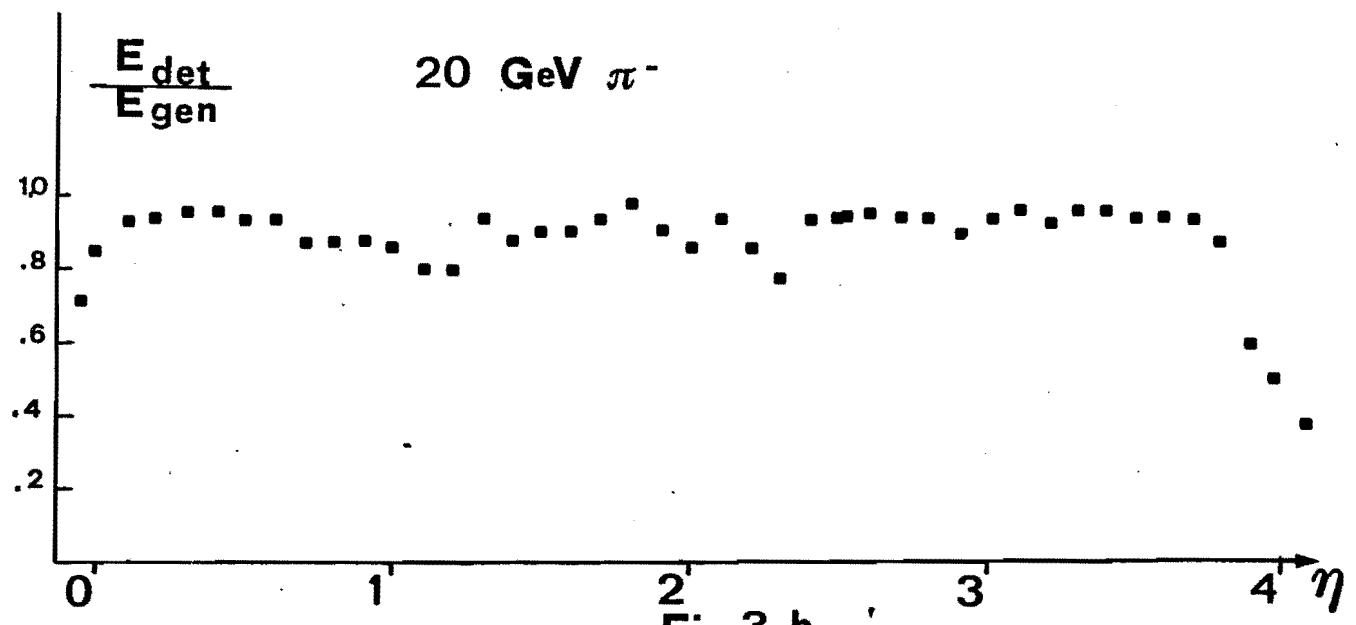
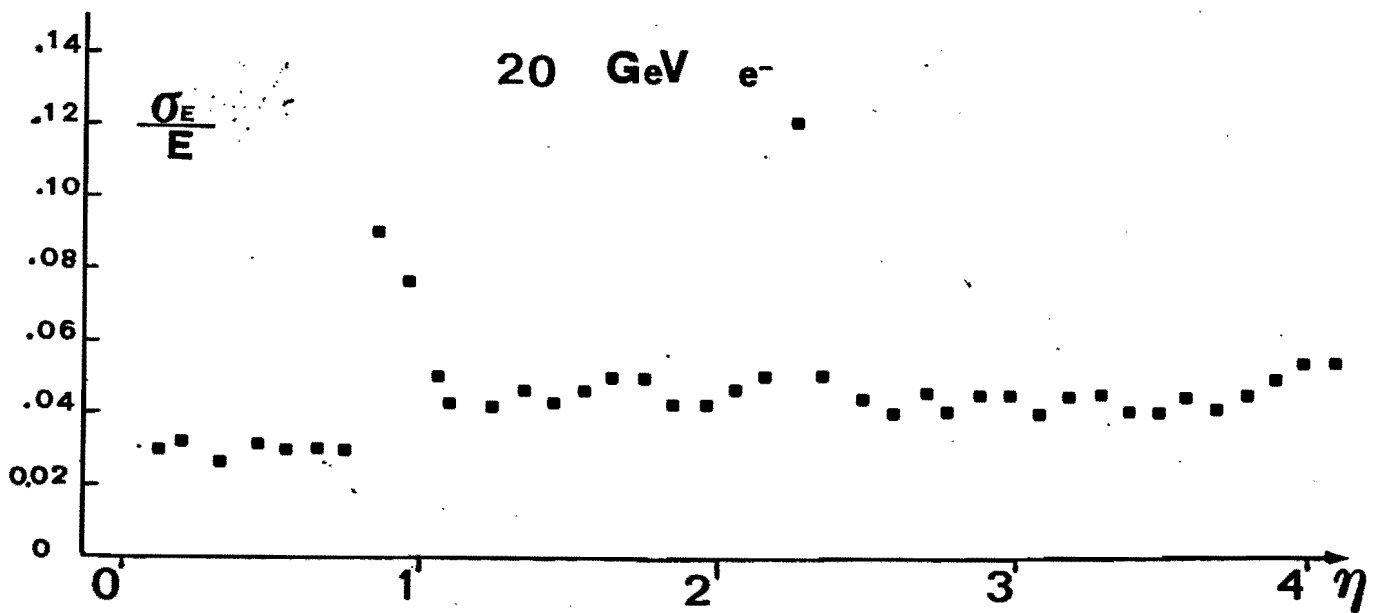


Fig 3 b



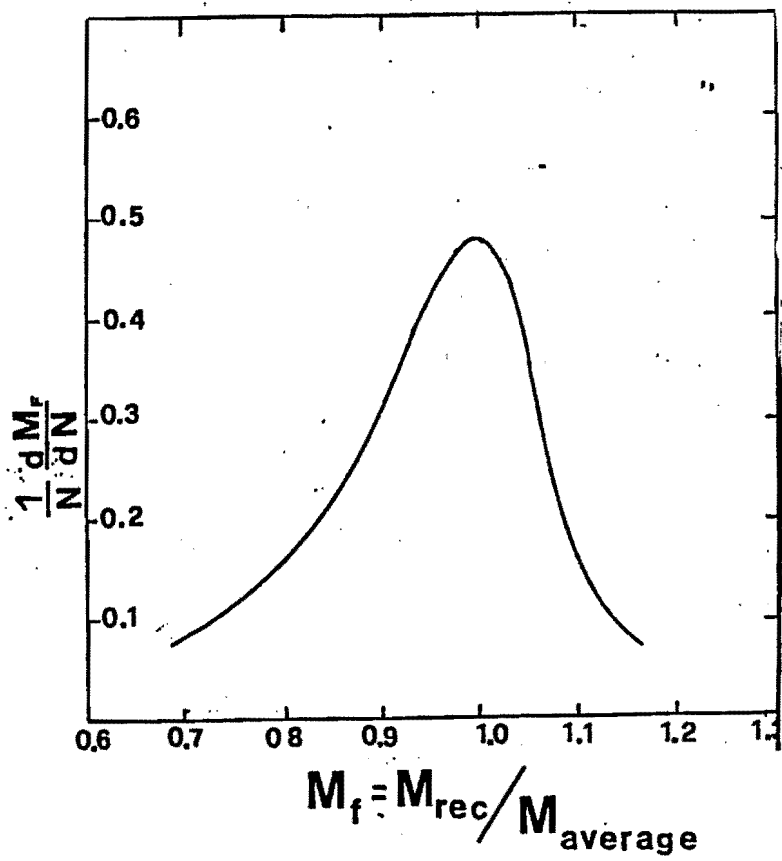


Fig 5

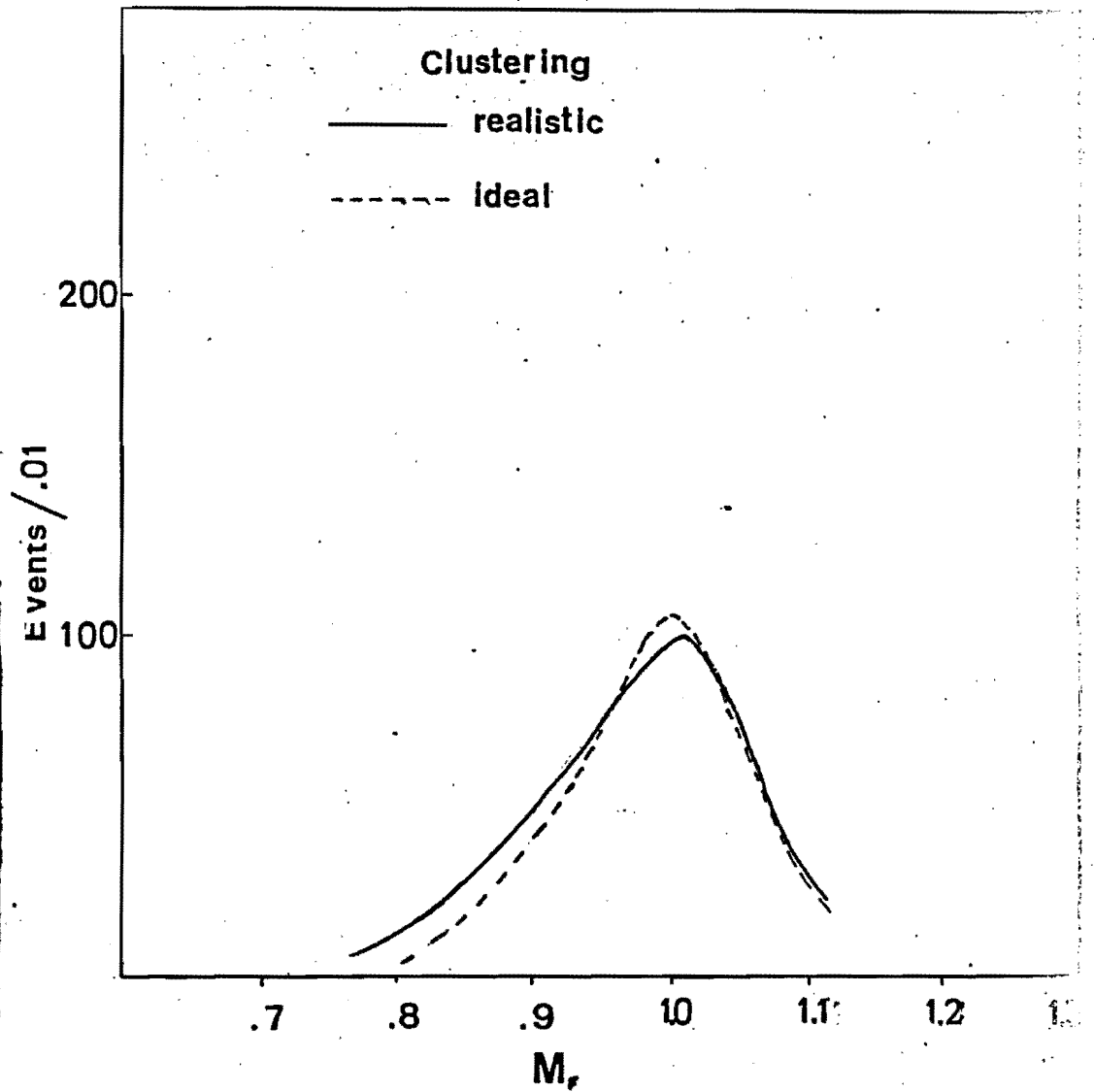


Fig 5b

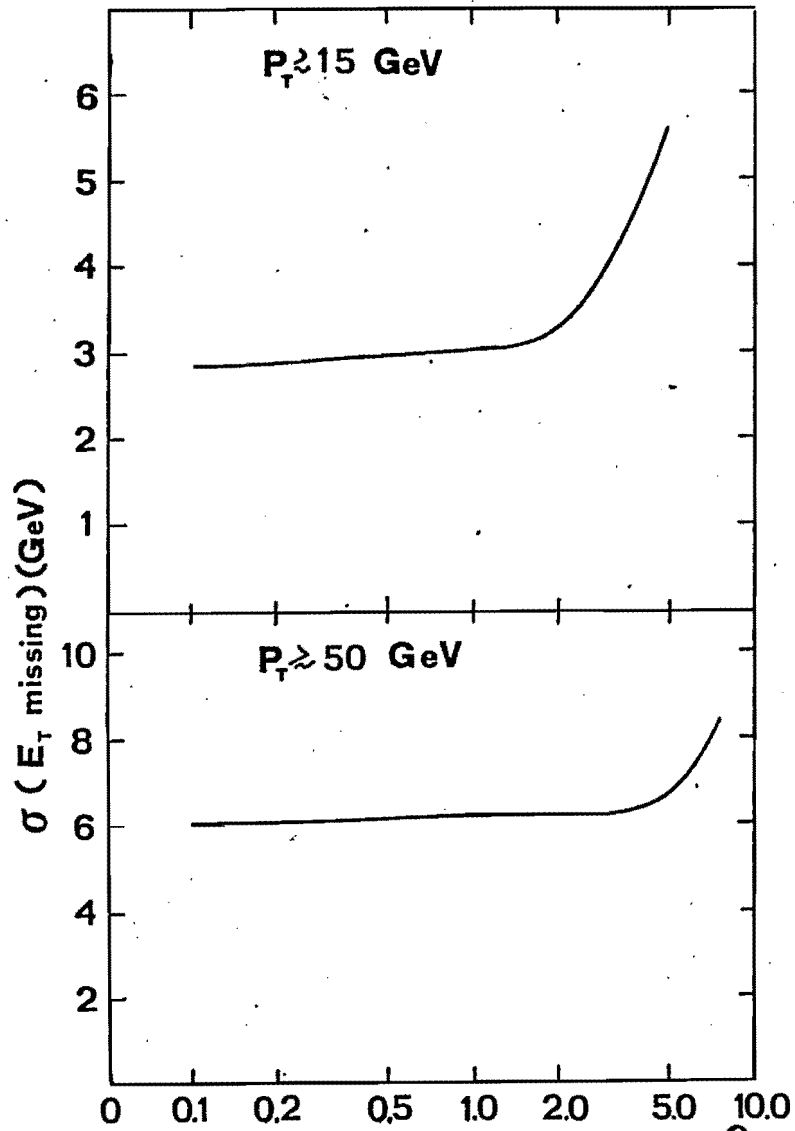


Fig 6

θ

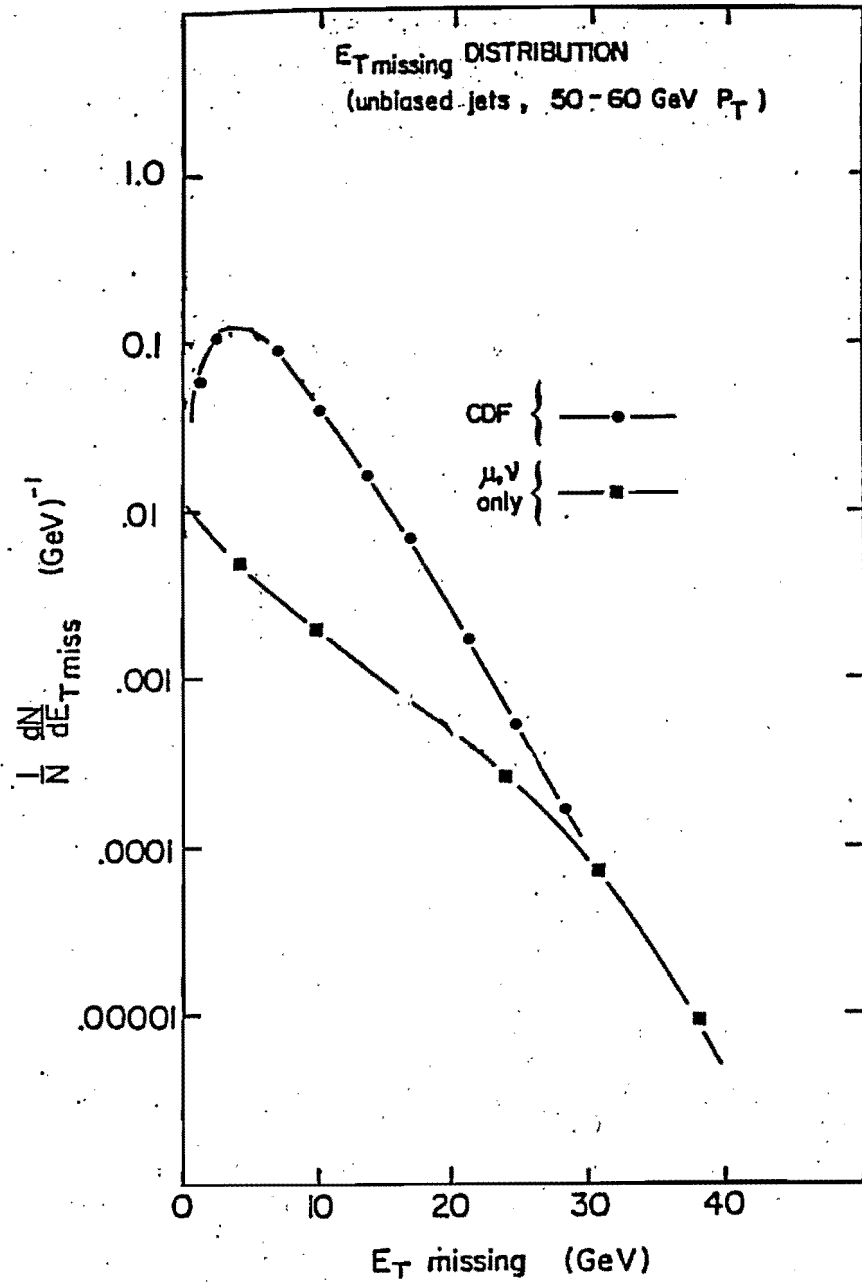


Fig 7

CHAPTER V

THE SILICON VERTEX DETECTOR (SVX)

The CDF Silicon Vertex Detector has been designed to allow CDF to tag heavy flavour production and decay. We illustrate in the first part of this Chapter how heavy flavours were tagged in a number of Collider experiments before CDF. In the second part we describe how the SVX was simulated and how its capability of finding secondary vertices was estimated.

V.1 HEAVY FLAVOUR TAGGING AT COLLIDERS

Since several years a number of attempts have been made both in $e e$ experiments and to a lesser extent at the SppS to disentangle heavy quarks jets from the bulk of the uninteresting hadronic processes. Despite of the difficulties these attempts were in part fruitful.

The most direct way to tag a jet initiated by a charm quark is to reconstruct charmed mesons in an invariant mass plot. The known $D^* - D^0$ mass difference can be imposed to isolate D^* decays into $D^0 \pi$ ($D^* \rightarrow D^0 + \pi, D^0 \rightarrow \pi^+ K^-$). This trick was used by the various experiments which attempted this search at PETRA as well as at PEP. Recently CLEO and HRS have been able to reconstruct the D^0 directly (V,1). These tags have been used as a starting point to study the properties of charmed jets, assuming the jet opposite to the one containing the reconstructed D^* to be dominantly a charmed jet.

In fig 1 the results of the TASSO collaboration at PETRA on the sphericity and charged multiplicity distribution of the prongs opposite to the tagging D are shown. Charmed jets do not have any striking difference with respect to normal jets. This is not a prove against the method, but does not strengthen the confidence on the validity of the method to study heavy quarks jets. If one subtracts the reconstructed D from the jet to which it belongs, the final properties of this rescaled jet are even closer to the ones measured for the average jet at the rescaled energy. These results are shown in fig. 2.

Recently results on the difference between beauty jets and average jets were obtained at PEP. In this case a large P_T lepton was requested, and the jet in the opposite hemisphere (relative to the lepton) was studied. A clear

difference, with respect to the average jet, in the rapidity distribution of charged tracks was seen (V,2). The beauty jet has also a broader angular distribution and a larger multiplicity (fig 3). Qualitatively one would expect b-jets to be also more spherical than the light ones, given that they originate from a more massive primary quark. One understands that any distinctive feature of heavy jets like this one, once firmly established and numerically quantified, might be exploited as an additional means of heavy flavour tagging.

The measurement of the lifetimes of beauty mesons and of the tau lepton in $e^+ e^-$ experiments was performed in a statistical way. Events with a large P lepton were selected the impact parameter distribution of the prongs in the transverse plane to the beam axis was studied. The experimental resolution on this parameter was $\sim 150-200 \mu\text{m}$, while a natural decay length $c\tau$ (τ = lifetime) of 30-300 μm was expected. The observed deviation from $\tau = 0$ was therefore small, but still sufficient to derive the average lifetime of beauty particles with $\sim 30\%$ error. This method cannot, as it is, serve as a tag of single beauty events. This will however be possible if an improvement in resolution of a factor 10 is achieved, and this is planned in CDF.

Recently TASSO (V,3) used another way to enrich the bb content of the sample. They selected events with large sphericity in both hemispheres, then each particle of each jet was boosted to the rest frame of a hypothetical particle travelling along the sphericity axis with $\beta = 0.7$. The jet sphericities S_1 and S_2 in this frame were calculated and $S_1 * S_2$ was requested to be $> .1$. The impact parameter distribution of the tracks of the accepted sample was consistent with a B lifetime $\tau = (1.8 \pm .38 \pm .37) * 10^{-12}$ sec (fig 4). It does not seem that this method might become applicable, even in perspective, to heavy flavour tagging at the pp colliders.

Jet studies at pp colliders are much more difficult, because one does not know the energy in the c.m.s. of the colliding partons and because of the longitudinal boost of the jet-jet system in the laboratory frame which distorts the event. UA1 studied a sample of 2-jet events and found a signal for charm production by looking at the decay of

$D^+ \rightarrow D^0 \pi^+ \rightarrow K \pi^+ \pi^+ + c.c.(V,4)$. For events with $146 \leq M(K\pi^+\pi^+) - M(K\pi^+) \leq 148$ MeV the $M(K\pi^+)$ spectrum exhibits a peak of 14 events (over a background of 6) at 1870 MeV, compatible with the D^0 mass (fig.5). The sample was isolated by requiring an electron trigger, namely at least 10 GeV of localized transverse energy deposited in the e.m. calorimeter, and more than 60 GeV of total E_T in the calorimeters at $|\eta| < 1.5$. Moreover in order to exploit at best the performances of the central tracking, a subset of 3400 well measured events out of a total of $1.2 \cdot 10^5$ satisfying the required trigger, was selected with a global efficiency of $\sim 0.2 \cdot 10^{-3}$.

This procedure appears to have an insufficient (and badly known) efficiency to be applied to a search for rare interesting events.

Summarizing, the only way exploited so far for direct identification of charmed jets was to look at the D decays. B mesons were not reconstructed through the identification of their decay prongs (because of the larger multiplicity, the combinatorial background is larger than for D's) but jets which were likely to originate from beauty were tagged by a large P lepton or signalled by a large sphericity in both hemispheres. Even if they are more indirect, because of the larger acceptance these methods are more likely to be exploited in the future searches for new heavy particle than D tagging.

The long lifetime of heavy mesons was not directly exploited so far, the main limitation being the poor resolution in impact parameter of the central tracking systems. Most new collider detectors are planning to overcome this limitation by implementing high precision vertex detectors, and so is doing also CDF. The design performances of the our SVX are discussed in the following.

V.2 The CDF Vertex Detector

We simulated a silicon vertex detector made of four shells of silicons multistrip detectors, surrounding the interaction region at B0 as near as possible to the beam pipe, as mentioned in III.5. The assumed geometry in our calculations was a dodecagonal shape for all shells. We do not expect any significant difference in performance between this configuration and to the dodecagonal-octagonal shape of

the actual design described in Chapter III.

V.2.1 Event files and detector simulation

Several input event files, containing 200 two jet events each, were generated with the following options:

- a) each jet is initiated by a charm (beauty) quark,
- b) beam jets are generated on top the hard scattering jets,
- c) $10 \text{ GeV} \leq P_{T,j} \leq 200 \text{ GeV}$.

ISAJET events were then traced through the detector to obtain a typical raw data output from the silicon vertex. The following effects were included in the simulation of the SVX:

- a) multiple scattering,
- b) particle decays and photon conversions,
- c) Landau fluctuations of the energy deposit in the silicon layers,
- d) smearing of the measured charge due to electronic noise ($\sigma_N = 7 \text{ KeV}$),
- e) transverse spread of the interaction region.

The longitudinal spread of the interaction region was set either to 0 or 20 cm to study its effect on the efficiency for finding secondary vertices.

V.2.2 Analysis

The output of the simulation is a list of fired electrodes and their measured charges Q_i . In order to account for ambiguities, we disregard sets of more than two contiguous signals, i.e. if two or more tracks cross adjacent cells the information is disregarded (this is a pessimistic attitude, we are at present studying how to exploit also this information).

We are then left with a list of what we call "clean hits". To each clean hit we can associate a position on the wafer by the charge division method:

$$x = (x_i Q_i + x_{i+1} Q_{i+1}) / (Q_i + Q_{i+1}).$$

where x_i are the electrode positions.

The track finding is done under the following

assumptions:

- a) perfect pattern recognition (i.e. we know exactly which hit belongs to which track),
- b) the track momentum has already been measured by the central tracking system with an accuracy ($\Delta P_T / P_T^2 = 1.0 \cdot 10^{-3} \text{ GeV}^{-1}$).

We will soon refine point b) by properly taking into account the angular dependence of momentum resolution.

We also require at least two clean hits per track. We fit all tracks in the reference frame of the wedge defined by the first wafer hit by the track (y axis through the symmetry axis of the wedge). The track equation in the cartesian coordinates, x,y in the R- φ plane can be written as follows :

$$\zeta = x + \frac{C R^2}{\sin \varphi_0 (1+2CD)} = y \cot \varphi_0 - \frac{(1+CD)D}{(1+2CD)\sin \varphi_0} = a + by$$

where $R^2 = x^2 + y^2$, $C = .225/P_T$ (m^{-1}) in a 15 Kgauss field (with P_T in GeV/c), φ_0 = angle between the track direction and the x-axis at the position of minimum approach to the beam axis. To get the reconstructed values of D and φ_0 , we fit iteratively a straight line of the forme $\zeta = by + a$, with starting values $D=0$, $\varphi_0 = 90^\circ$.

Much care was taken in estimating the measurement errors. Correlation between errors on different layers, induced by multiple scattering, had to be considered to calculate the correct values of σ_D and σ_{φ_0} (it is however to be expected some increase in these errors to occur when the deterioration of $\Delta P_T / P_T$ at small angles will be taken into account). Track parameters and their errors are rotated back to the laboratory frame after fitting. This procedure is found to converge quickly to best-fit values of D and φ_0 .

Once the tracks are reconstructed, we need to find out wether they are generated in one or more vertices. A vertex finding algorithm can be based on the following considerations : let $y = a_i + b_i \zeta$ be a set of tracks with a common vertex (ζ_v, y_v) , then for every i:

$$a_i = y_v - \zeta_v b_i$$

Thus, if we associate a point (b_i, a_i) in the a,b plane to each track, all points representing tracks originating from the same vertex lay on a straight line. The problem of

vertex finding is reduced in this way to a problem of pattern recognition of straight lines in the a, b plane. The slope and a -intercept of such straight lines would provide directly the parameters z_v, y_v of the vertex. In the neighborhood of the interaction point (say $R \leq 1$ cm) our tracks can be well approximated by straight lines (to within a few μm). We can therefore apply this principle to the reconstruction of the primary vertex and of the vertices originated by the decay of short lived particles by approximating the particle trajectories with straight tracks of impact parameter D and angle ψ_0 in the transverse R, ψ plane.

We now describe the algorithm used for the reconstruction of the primary vertex. This algorithm is based on the consideration that the large majority of tracks in each event originates from the primary vertex, and that the apparent transverse size of the interaction region is small ($\leq 50 \mu\text{m}$).

We then proceed through the following steps:

- a) select all tracks with $|D| < 200 \mu\text{m}$ and $P_T > .5$ GeV for primary vertex reconstruction, $P_T > 0.2$ GeV for secondary vertices.
- b) request at least 5 tracks
- c) fit a straight line in the a, b plane through the points representing the event tracks to get a first estimate of the vertex position.
- d) select all track in the event consistent with this estimate at a 2σ level.
- e) request again at least 5 tracks
- f) fit again to get the final value for the primary vertex position

Typical resolution for the x and y coordinates of the primary vertex are $\sim 20 \mu\text{m}$ as shown in fig 6, a and 6, b.

The origin of our reference frame is then moved to the reconstructed primary vertex. We refit all tracks with $P_T > 0.2$ GeV (in order to benefit from the vertex constraint) requesting also the hit in the innermost layer to be clean, and at least three clean hits in total. The straight line defined in this frame by the points representing tracks originating in the primary vertex is chosen as the b -axis ($x_v = y_v = 0$ in equation (1) implies $a_i = 0$ and leaves free the b_i values).

We also require $|D| < 1$ cm, to clear the sample from early decays of long lived particles (K^0 's, Λ 's). In comparison with points representing tracks from the primary vertex, which lay on the horizontal b-axis, a track originating from a secondary vertex is indicated by a representative point whose a-coordinate is significantly different from zero. We shall call λ the ratio a/σ_a . Values of λ in excess of 1 indicate candidate tracks of secondary vertices.

V.2.3 Secondary vertex reconstruction

At this point the problem of secondary vertex reconstruction is that of finding among these candidate tracks those whose representative points line up in parameter space. Given that there always exists a straight line through two points, we require at least three tracks to define a secondary vertex.

The algorithm used proceeds as follows :

- a) create two groups of tracks, A_2 containing all tracks with $\lambda > 2$, A_3 containing all tracks with $\lambda > 3$
- b) loop on all combinations of three different tracks belonging to the A group, for each triplet we fit a straight line and store the fit information each time $\chi^2 \leq 0.35$. Each stored triplet is called candidate vertex;
- c) loop on candidate vertices: for each candidate select all tracks in the A_2 group consistent with it at a 2σ level and such that the confidence level of the χ^2 obtained by adding the new track to the fit is still smaller than 50%. Store all tracks associated to each candidate vertex and the corresponding χ^2 .
- d) At this point we want to select true vertices out of our list of candidates. This is accomplished as follows:
 - I) look for the candidates with the largest number of tracks,
 - II) if there are two equivalent such candidates, define as true vertex the one with the best χ^2 ,
 - III) delete all tracks associated with this true vertex

from other candidates,

IV) restart from point I) with the remaining candidates and keep looping until no candidate is left.

V.2.4 Discussion of the results

We will first discuss inclusive distributions, and then turn to detailed reconstruction of vertices in single events. A very important parameter to judge the performance of the vertex tracking system is the error on the reconstructed impact parameter D . Due to multiple scattering on the beam pipe and the silicon wafers, this error is strongly dependent on the track momentum; at constant P_T , however, it is roughly independent of the polar angle. The dependence of D on P_T at 90° emission angle is shown in fig 7. One sees that as long as $P_T > 2$ GeV, the resolution on D saturates at $\sigma \sim 45 \mu\text{m}$ due to the combined effects of detector resolution and distance from beam axis. Fig 8 shows how the resolution depends on pipe radius (assuming a distance of 4 mm between the beam pipe and the first silicon layer). Any reduction of beam pipe radius would be very useful since one should consider using tracks of low momentum (steeper slope of broken line in fig. 8). This would provide higher track multiplicity and thus better vertex finding efficiency. The P_T distribution of particles originated by charm and beauty decay are very similar, as shown in fig. 9 and fig. 10. One sees that a cut at $P_T > 0.2$ GeV is already a significant one. It must be stressed that the distance of the first layer from the interaction region will have a very strong influence on σ_D . An ultimate goal might be a 1.5 pipe diameter and no outer coating (internal baking wires in a carbon fiber beam pipe). In this case there would be an improvement on over what shown in fig. 7 and 8 by approximately 25 %.

As stated previously, the value of λ is critical to distinguish tracks originating from a secondary vertex from those originating in the event vertex. This calls for an accurate determination of the error in the a, b plane. Fig 11 shows the distribution of $a_{\text{gen}} - a_{\text{rec}}$ (f.w.h.m. of about 200 μm) and fig. 12 shows the distribution of $(a_{\text{gen}} - a_{\text{rec}}) / \sigma_a$. The distribution of fig. 12 is very nearly a gaussian with

$\lambda = 1$, which shows that the errors were correctly propagated in computing σ_a . The distribution of particles originating from the primary vertex is shown in fig. 13. Fig. 14 shows the same distribution for charmed meson decay prongs. Similar distributions for the run with beauty are shown in Figs. 15 and 16. It is quite clear that particles coming from the primary vertex are well confined within $\lambda \lesssim 3$, while particles coming from heavy mesons show a wider distribution, with very significant large λ tails in the beauty case (fig. 16) than for charm (fig. 14). This is due both to the longer lifetime of beauty mesons (we assumed $\tau = 1.4$ ps) and to the larger multiplicity of the decay.

Searching for parameters indicative of the efficiency in selecting interesting events, we have performed the following analysis. For each event we selected all tracks inconsistent with the primary vertex to the $n\sigma$ level ($\lambda \geq n$). We then counted the number of events with at least m tracks inconsistent with the primary vertex at the $n\sigma$ level. The results are shown in Tab 1 and 2 for various values of n and m . Tab. 1 displays the results of the run with charm and Tab. 2 those of the run with beauty. The four sub-tables in the figures correspond to different number of tracks missing the primary vertex ($m \geq 1$ to $m \geq 4$). The first row of each sub-table shows the number of events satisfying the criterion to the quoted statistical precision (columns 1 to 4 corresponding to $\lambda \geq 1$ to $\lambda \geq 4$), viz. the number of events containing candidate tracks. The second row shows the number of events where at least one of the candidate tracks comes from charm (beauty). The third row shows the number of events where no good tracks (from charm or beauty) is present among the candidates, while at least one of the candidates come from K^0 's or Λ 's. This line therefore gives an idea of the physical background. The fourth row shows the number of events where all candidates originate from the primary vertex. This line give an idea of the reconstruction errors which create misaligned tracks. Fig. 17 and 18 display in the b - a plane two events with beauty jets. Two clearly reconstructed vertices, one containing six tracks and one containing four tracks are found by the program in fig. 17. In fig. 18 only one secondary vertex is found (with multiplicity four).

We find plots like these extremely encouraging. We now

present our preliminary results on vertex finding efficiency for charm and beauty events.

V.2.5 Vertex finding efficiencies

We investigated the dependence of our vertex finding efficiency on the $R-\psi$ separation of the electrodes and on the length of the interaction region. Data of charm and beauty jets were analyzed with different assumptions, $\sigma_b = 0$ and $\sigma_b = 20$ cm, and different electrode pitches: $\Delta R\psi = 0$ i.e. perfect double track separation on all layers in one case, and $\Delta R\psi = 200 \mu\text{m}$ on the first layer and $250 \mu\text{m}$ on the other ones (present electrode geometry), and finally $400 \mu\text{m}$ on the first layer and $500 \mu\text{m}$ on the other three layers (degraded detector).

The results are given in Tab.3, Tab.4 in terms of the fraction of events with at least 1 reconstructed vertex.

One sees that a finite length of the interaction region with $\sigma_b = 20$ cm does not affect severely our efficiency, showing that we have enough geometric coverage.

The dependence of the efficiency on electrode density is much stronger, indicating that much would be gained in terms of efficiency by increasing the detector granularity.

In a separate study (V,5) we investigated the possibility to improve our resolution in track parameters using the overall information of the central tracking system (i.e. CTC, VTPC and SVX, see Chapter III). We found that at 90° , for large P_T tracks, the resolution in impact parameter saturates at $\sim 16 \mu\text{m}$, being about $50 \mu\text{m}$ already at P_T of 1 GeV (fig 19). Moreover we found an improvement in the P_T resolution by about a factor 2 above 5 GeV of P_T , while very little is gained by adding the VTPC information to the SVX (fig 20). Finally the impact parameter resolution of the SVX alone is clearly inadequate ($\sigma_b \sim 110 \text{ m}$), showing that the SVX needs to be backed by a large volume tracking system, in order to allow a significant search for secondary vertices of heavy flavour decay.

We conclude that the tagging of beauty events can be done with an efficiency of the order of 30 % (Table 3), and that our method would reject charm by an additional factor of ~ 15 (Table 4). This already justifies serious hopes and the applicability of the method to beauty tagging. It is clear,

however, that the rejection power of the method against any jet other than beauty or against spurious vertices of any sort should be better quantified in a realistic physics situation. This is what is attempted in the next Chapter.

$$\bar{p}p \rightarrow \bar{c}c + \text{beam jets}$$

events with ≥ 1 track inconsistent with primary vertex ($m \geq 1$)

	1σ	2σ	3σ	4σ
<u>NEV</u>	198	186	130	123
<u>at least 1D</u>	124	70	47	38
<u>only others</u>	47	76	81	85
<u>only primary</u>	27	40	2	0

events with ≥ 2 tracks inconsistent with primary vertex ($m \geq 2$)

	1σ	2σ	3σ	4σ
<u>NEV</u>	197	131	68	54
<u>at least 1D</u>	124	62	38	28
<u>only others</u>	47	56	30	26
<u>only primary</u>	26	13	0	0

events with ≥ 3 tracks incompatible with primary vertex ($m \geq 3$)

	1σ	2σ	3σ	4σ
<u>NEV</u>	195	86	30	20
<u>at least 1D</u>	124	46	19	14
<u>only others</u>	47	34	11	6
<u>only primary</u>	24	6	0	0

events with ≥ 4 tracks incompatible with primary vertex ($m \geq 4$)

	1σ	2σ	3σ	4σ
<u>NEV</u>	195	55	9	4
<u>at least 1D</u>	124	32	7	3
<u>only others</u>	47	20	2	1
<u>only primary</u>	24	3	0	0

Table 1

$$200 \bar{c}c, 10 < p_t < 200 \text{ GeV}/c, \sigma_2 = 20 \text{ cm}$$

from $\bar{p}p \rightarrow \bar{b}b + \text{beam jets}$

events with ≥ 1 track incompatible with primary vertex ($m \geq 1$)

	1σ	2σ	3σ	4σ
<u>NEV</u>	197	190	176	172
<u>at least 1B</u>	170	158	142	135
<u>only others</u>	16	25	33	37
<u>only primary</u>	11	7	1	0

events with ≥ 2 track incompatible with primary vertex ($m \geq 2$)

	1σ	2σ	3σ	4σ
<u>NEV</u>	196	164	136	128
<u>at least 1D</u>	170	148	125	115
<u>only others</u>	15	14	11	11
<u>only primary</u>	11	2	0	0

events with ≥ 3 tracks incompatible with primary vertex ($m \geq 3$)

	1σ	2σ	3σ	4σ
<u>NEV</u>	195	139	106	91
<u>at least 1D</u>	170	132	103	89
<u>only others</u>	14	7	3	2
<u>only primary</u>	11	0	0	0

events with ≥ 4 tracks incompatible with primary vertex ($m \geq 4$)

	1σ	2σ	3σ	4σ
<u>NEV</u>	191	115	68	50
<u>at least 1D</u>	170	110	67	49
<u>only others</u>	13	5	1	1
<u>only primary</u>	8	0	0	0

Table 2

$200 \bar{b}b_{10} < p_t < 200 \text{ GeV}/c, \sigma_2 = 20 \text{ cm}$

Table 3

$$\bar{p}p \rightarrow \bar{b}b + \text{beam jets}, \quad p_{T,\text{jet}} \geq 10 \text{ GeV}$$

σ_z (cm) $\Delta R\varphi(\mu)$	\emptyset	200, 250	400, 500
0	69 %	35 %	14 %
20		29,5 %	

Event tagging efficiency (at least one secondary vertex found).

Statistics on 200 events

Table 4

$$\bar{p}p \rightarrow \bar{c}c + \text{beam jets}, \quad p_{T,\text{jet}} \geq 10 \text{ GeV}$$

σ_z (cm) $\Delta R\varphi(\mu)$	\emptyset	200, 250	400, 500
0	10 %	3,5 %	.5 %
20	9 %	2 %	

Event tagging efficiency (at least one secondary vertex found).

Statistics on 200 events

FIGURE CAPTIONS (Chap. 5)

- 1) a) dN/dy distribution
 b) sphericity distribution
 for charmed jets opposite to the tagged D
 (full circle) and average jets (histogram) (V,1)
- 2) dN/dy distribution for the jets of
 the tagged D (full circle), for the
 average jet at the same energy (histogram),
 for the average jet at the rescaled energy)
 (dotted line)
- 3) Preliminary results of DELCO, dN/dy
 distribution for B jet (full circle)
 and the average jet (histogram) (V,2).
- 4) Impact parameter distribution of charged prongs
 in the B region (from TASSO) (V,3).
- 5) D signal in the $K\pi$ invariant mass (from UA1)(V,4).
- 6) Distributions of errors on/reconstructed transverse xy
 coordinate of production vertex for tracks accepted
 for the secondary vertex search.
- 7) Standard error on the reconstructed impact parameter, as
 a function of the track transverse momentum. As mentioned
 in the text, perfect pattern recognition and $\Delta p_T/p_T = .1\% \cdot p_T$
 is assumed to be provided by the CTC.
- 8) Dependence of the standard error of the impact parameter
 beam pipe radius, for two values of the track transverse
 momentum.
- 9) Transverse momentum distribution of tracks of charm
 jets (ISAJET events, $10 \text{ GeV} < p_{T,j} < 200 \text{ GeV}$).
- 10) Transverse momentum distribution of tracks of beauty
 jets (ISAJET events, $10 \text{ GeV} < p_{T,j} < 200 \text{ GeV}$).
- 11) Distributions of errors on the reconstructed a-parameter
 of tracks.
- 12) Distributions of errors on the reconstructed a-parameter
 of tracks, normalized for each track to the computed
 resolution.
- 13) λ -distribution of tracks of decay prongs of charmed
 particles in events with two $\bar{c}c$ jets.
- 14) λ -distribution of tracks of decay prongs of charmed
 particles in events with two $\bar{c}c$ jets.
- 15) λ -distribution of tracks originating in the
 primary in events with two $\bar{b}b$ jets.
- 16) λ -distribution of decay prongs of beauty
 particles in events with two $\bar{b}b$ jets.
- 17) Example of a $\bar{b}b$ event in the b, a representative plane.

Two secondary vertex are found in this event.

- 18) Example of a $b\bar{b}$ event in the b, a representative plane. one secondary vertex is found.
- 19) Momentum resolution of the tracking system at 90° :
CTC only, CTC + VTPC together, CTC, VTPC, SVX
altogether.
- 20) Impact parameter resolution of the tracking system
for tracks at 90° : CTC only, CTC + VTPC and CTC, VTPC,
SVX altogether.

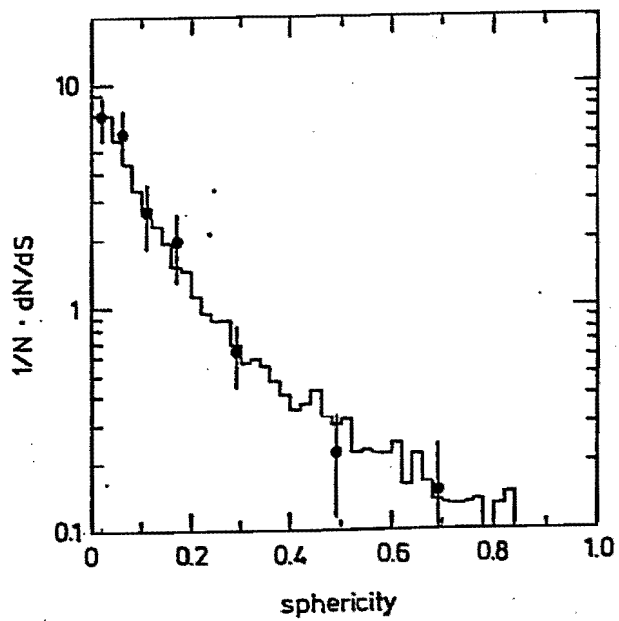
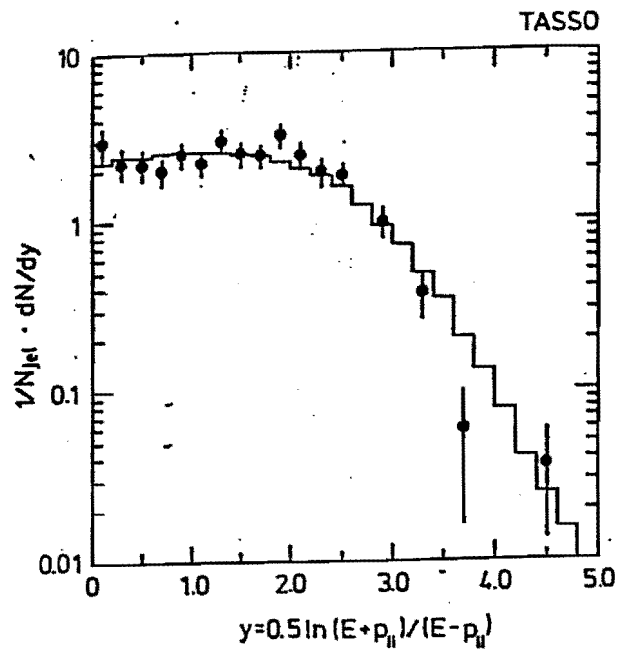


Fig 1

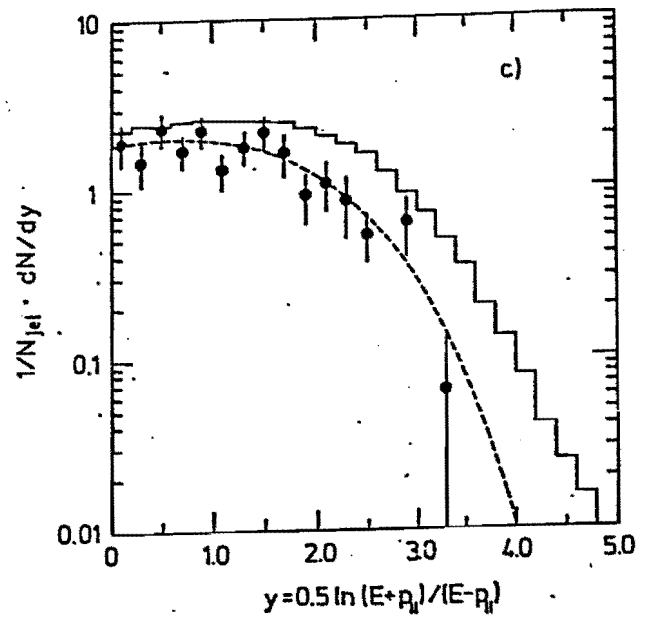


Fig 2

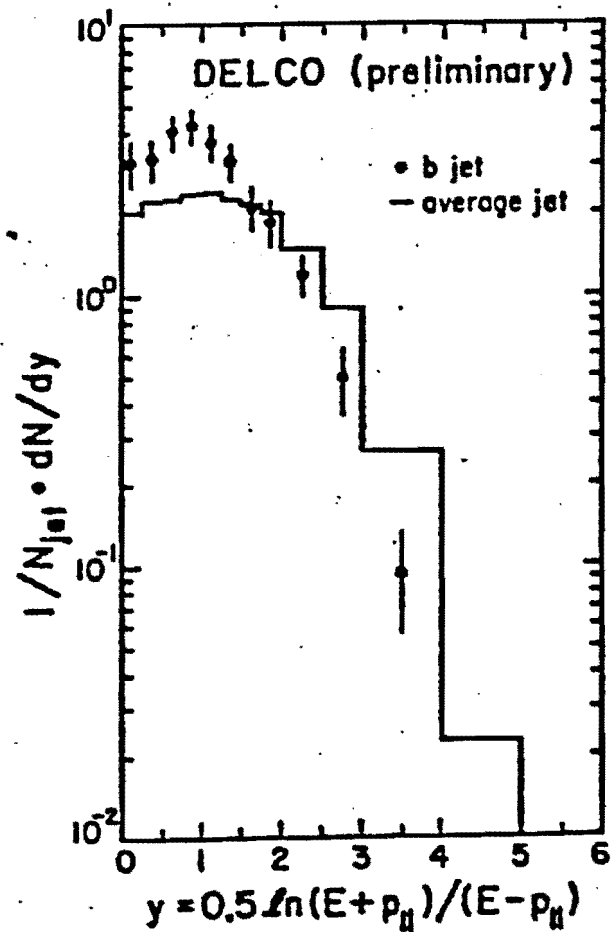


Fig 3

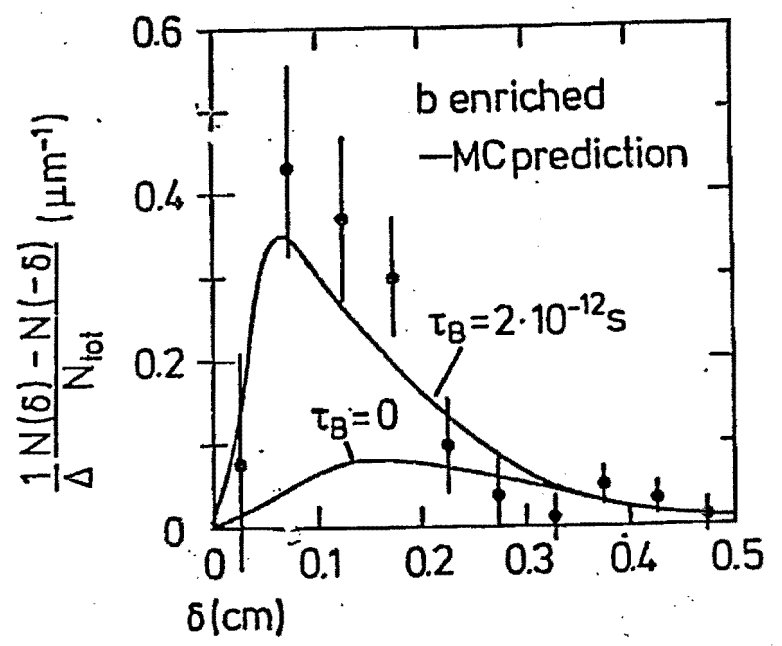


Fig 4

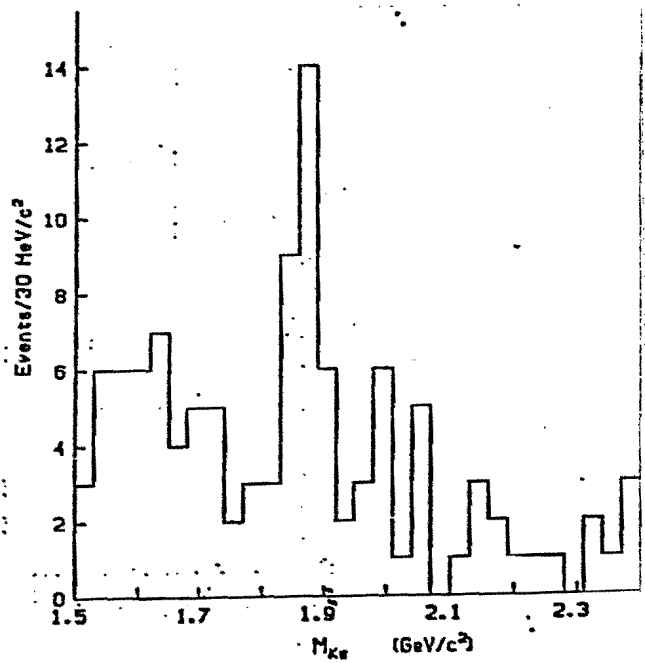


Fig 5

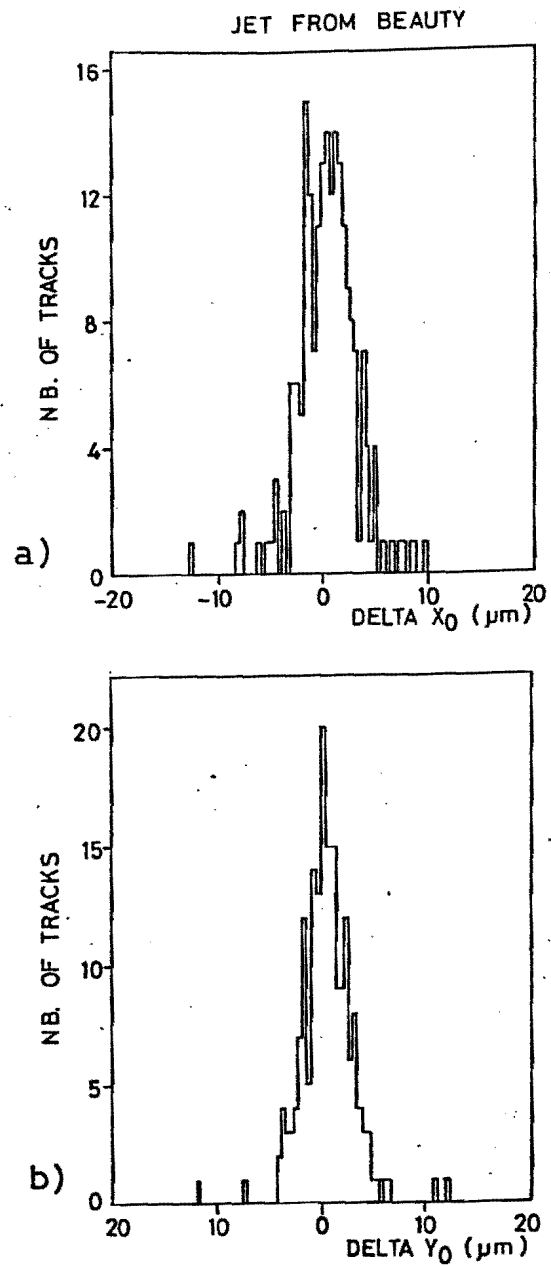


Fig.6

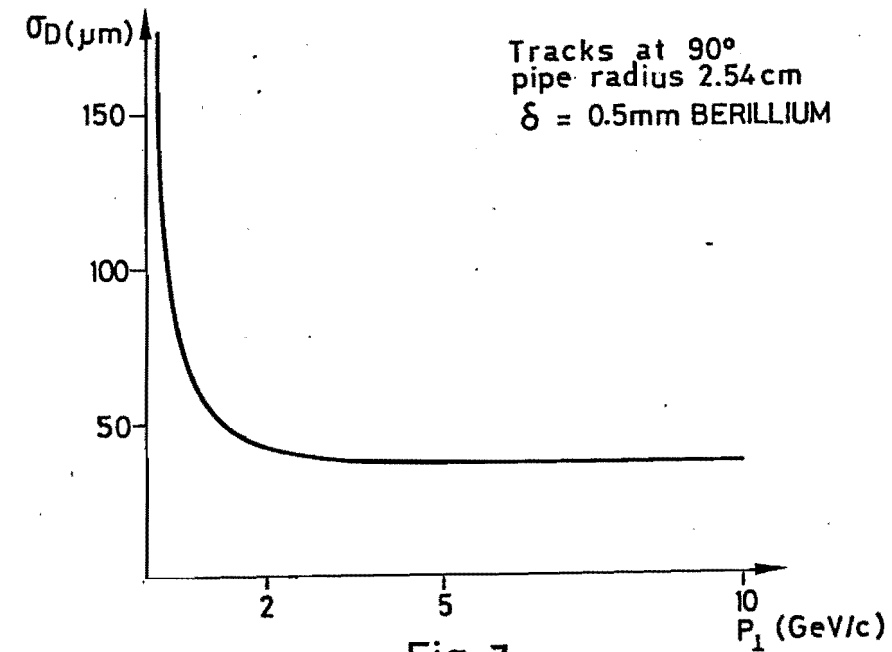


Fig. 7

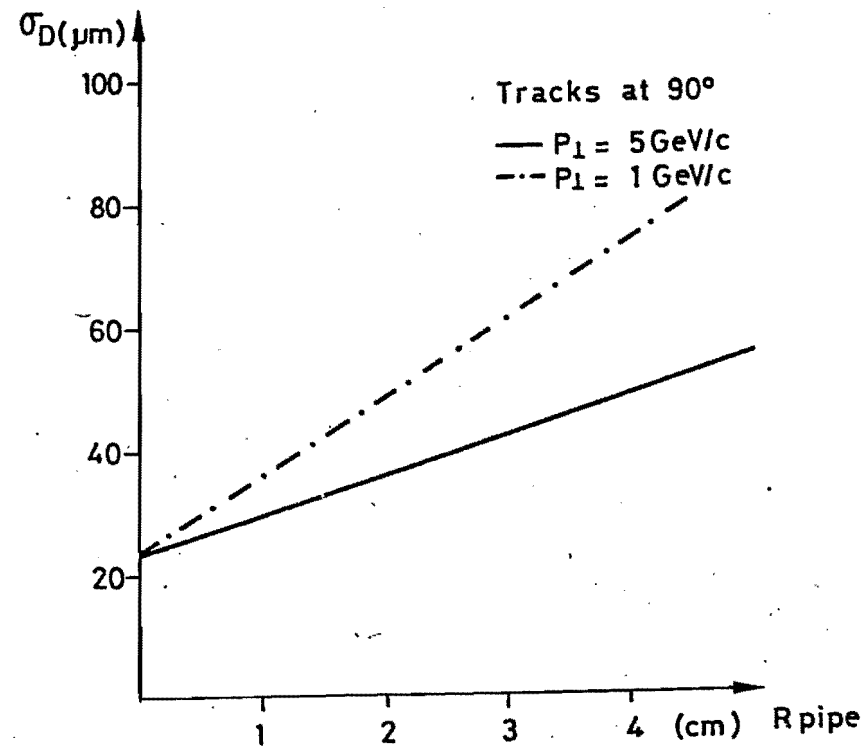


Fig. 8

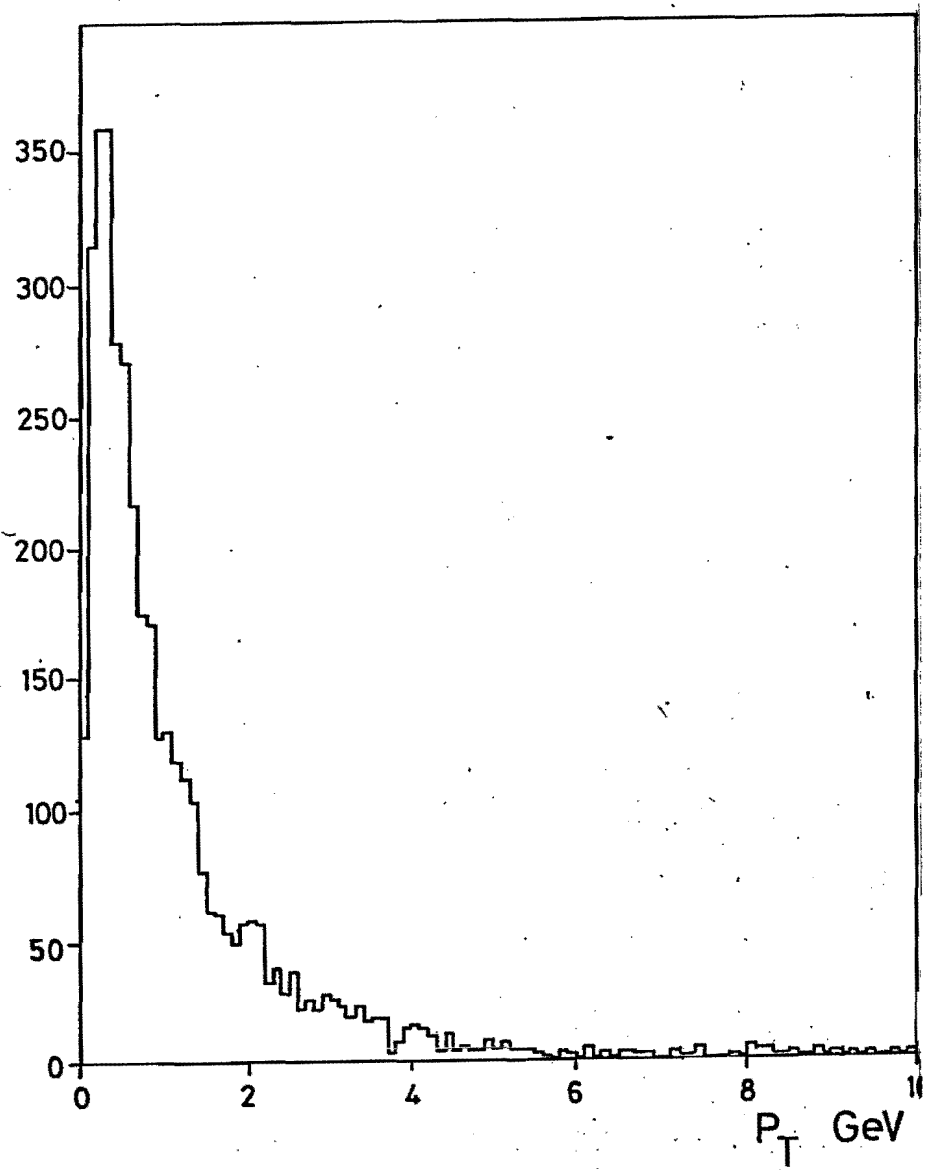


Fig. 9

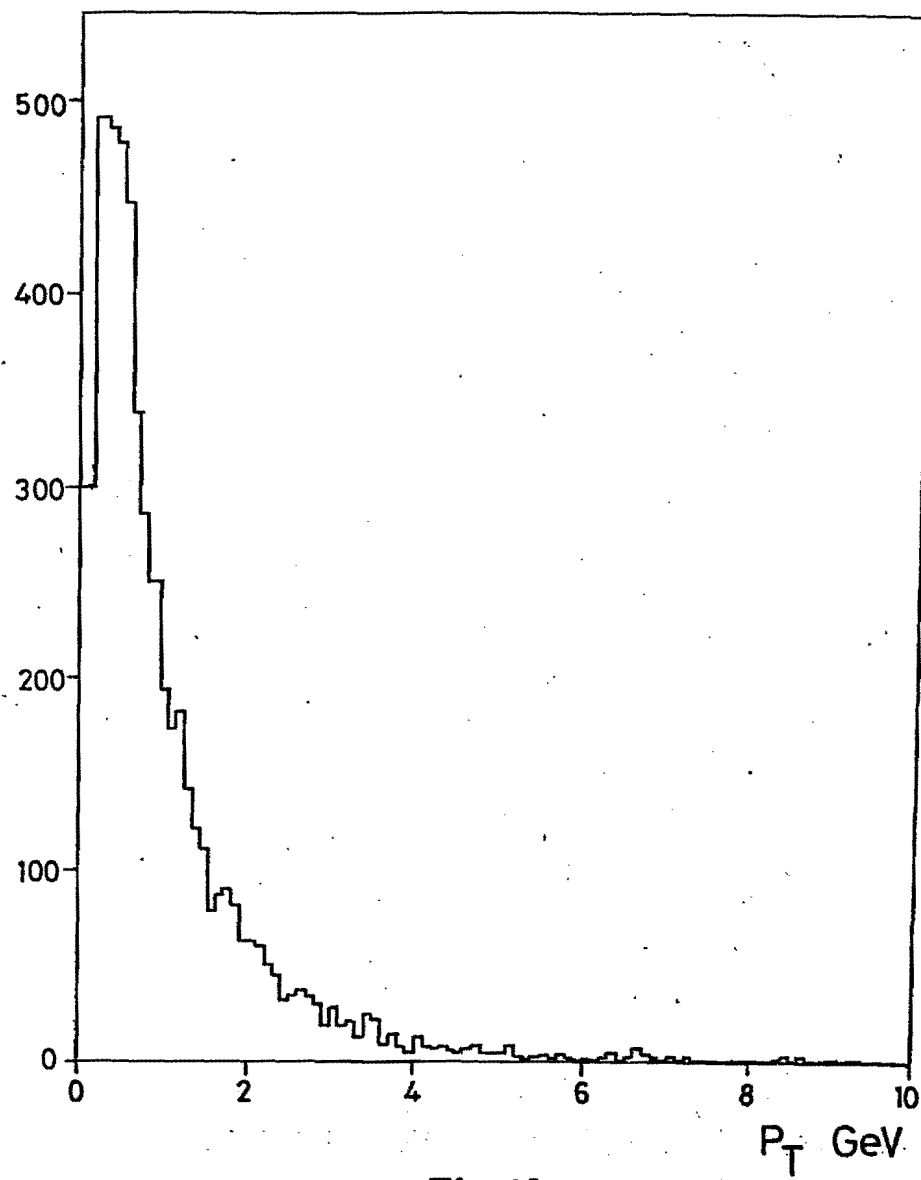


Fig.10

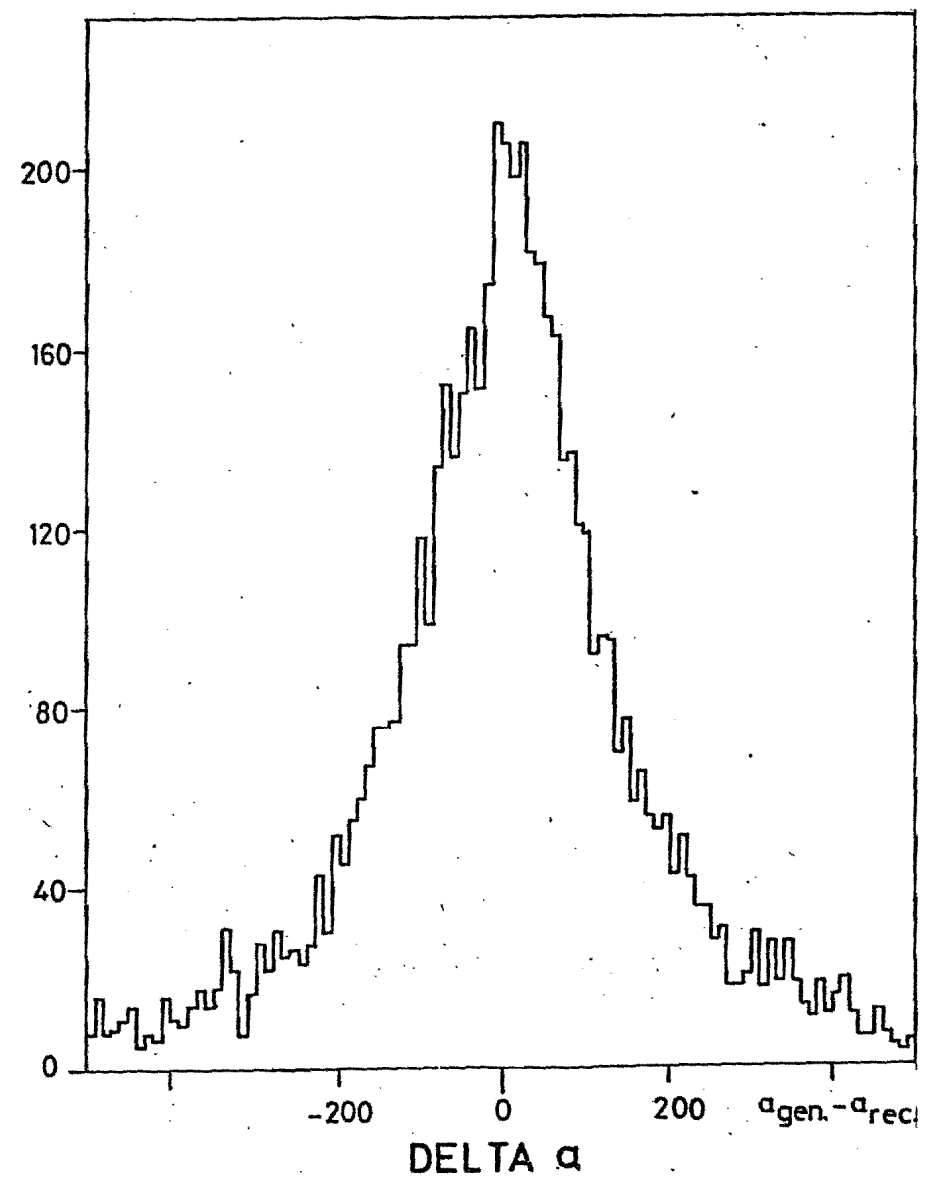


Fig.11

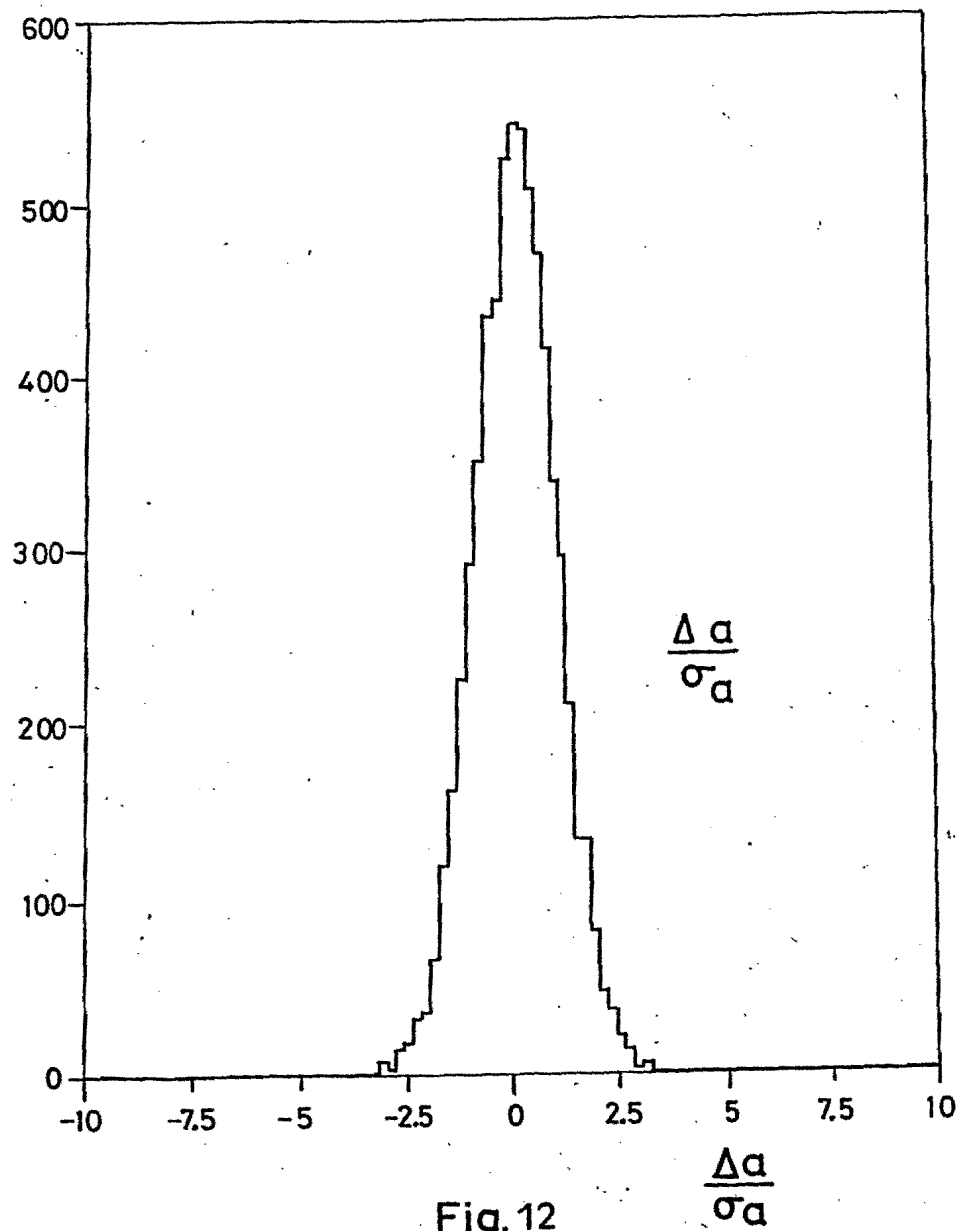


Fig.12

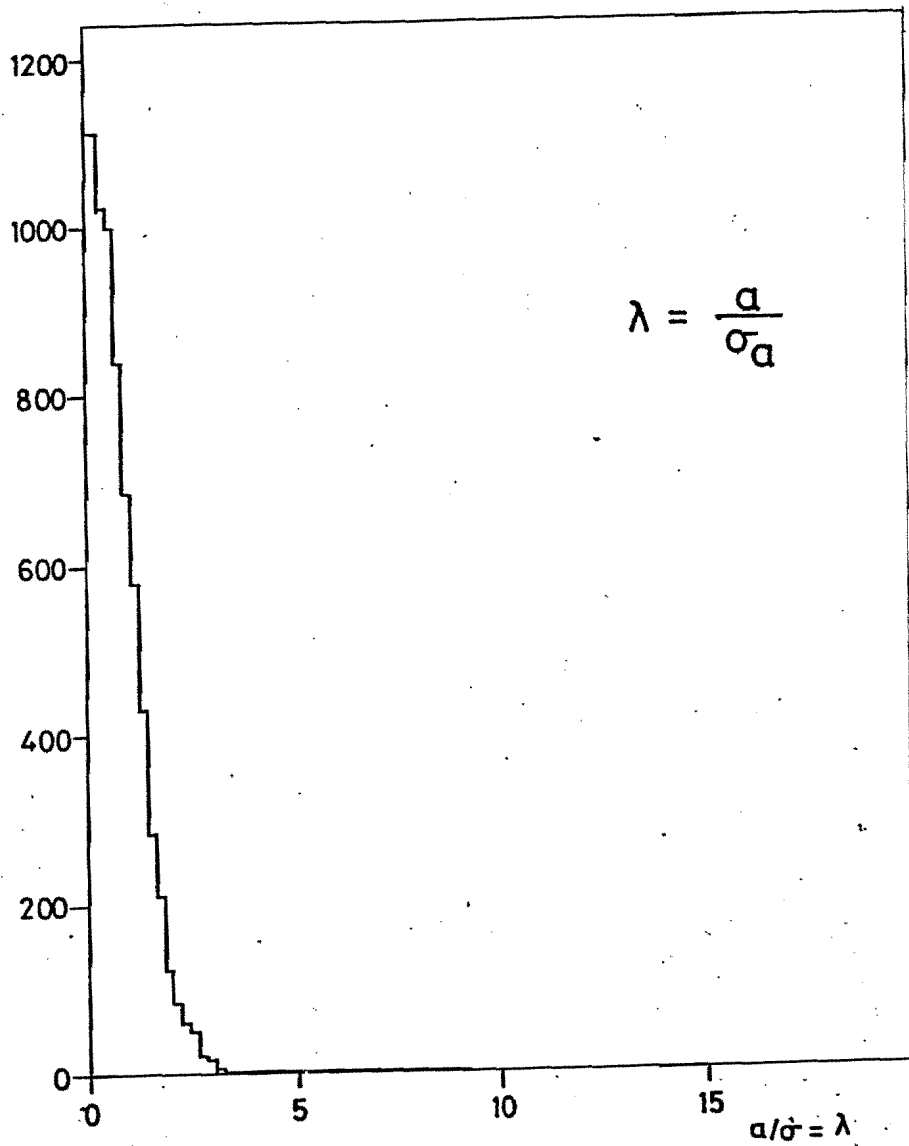


Fig.13

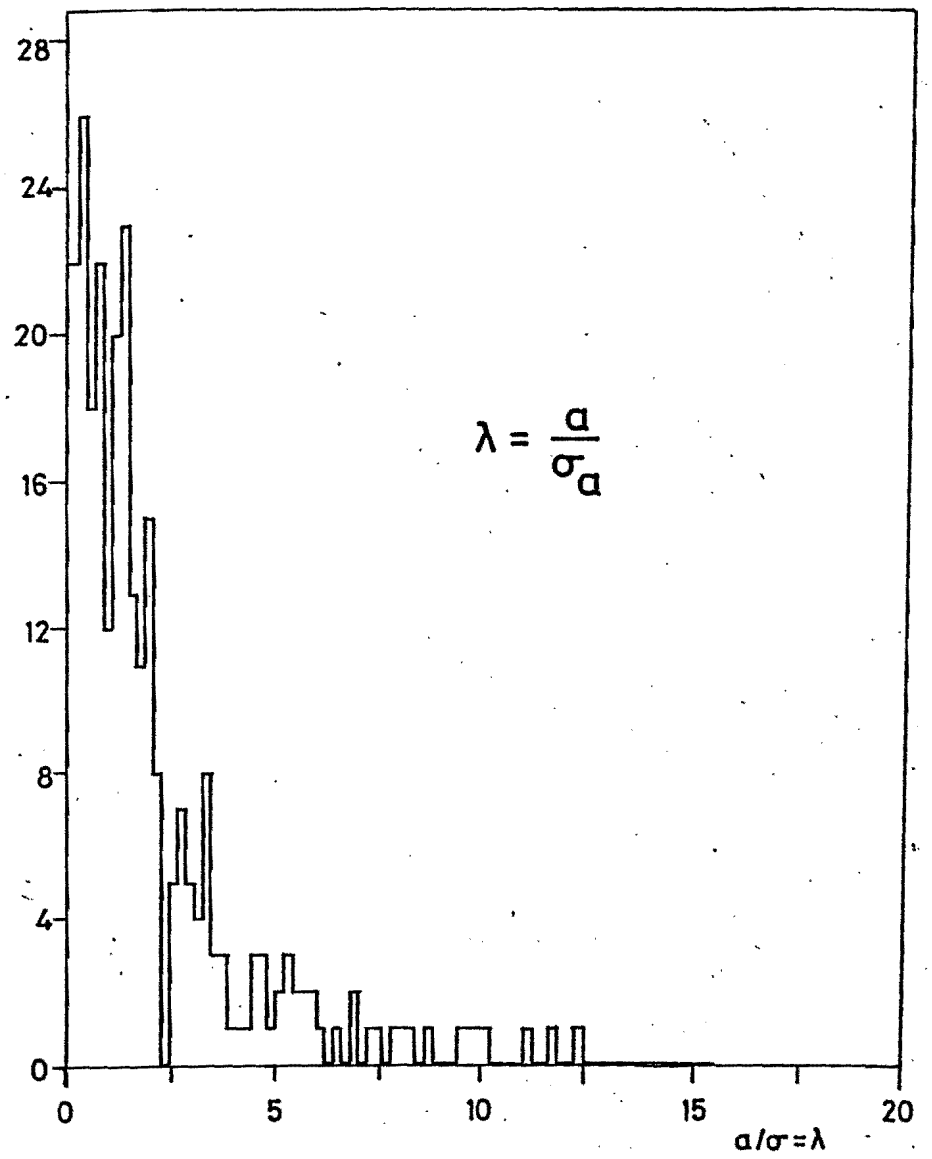


Fig.14

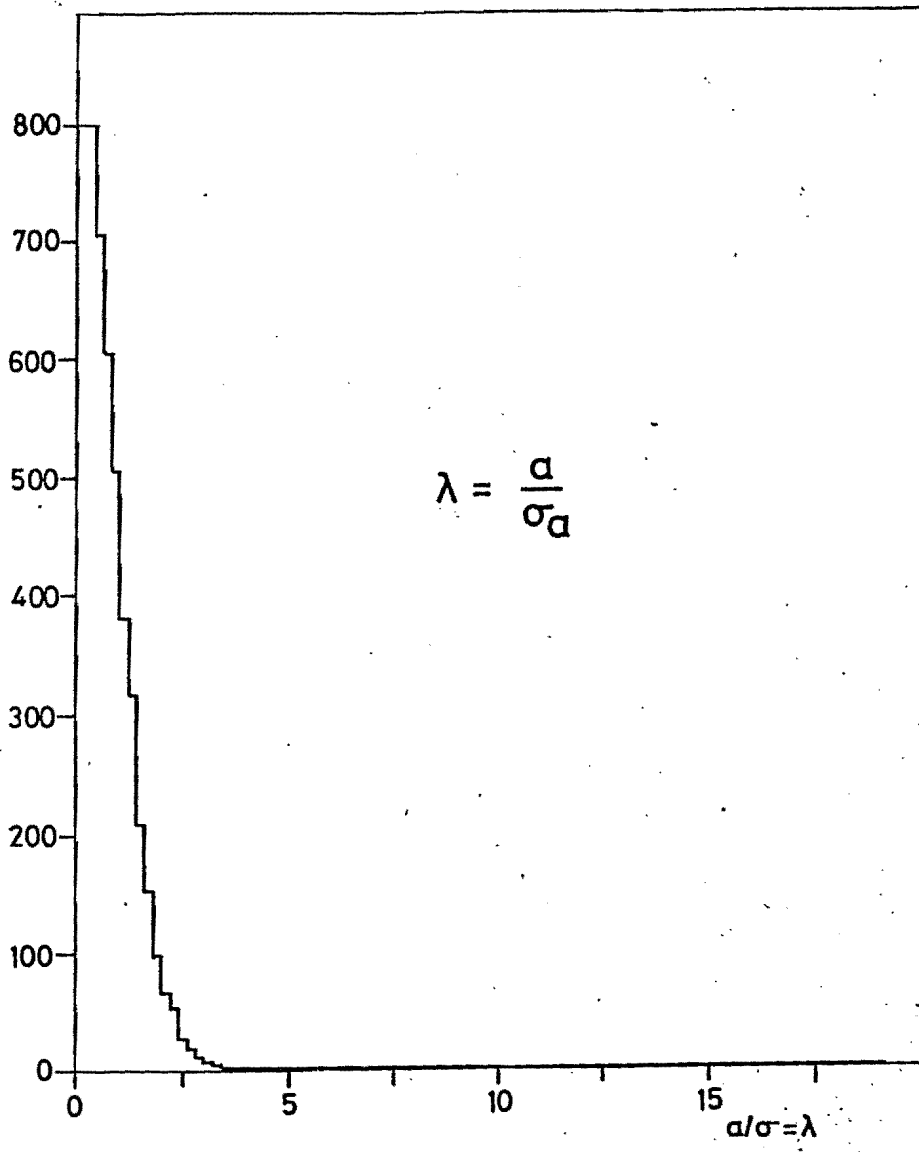


Fig.15

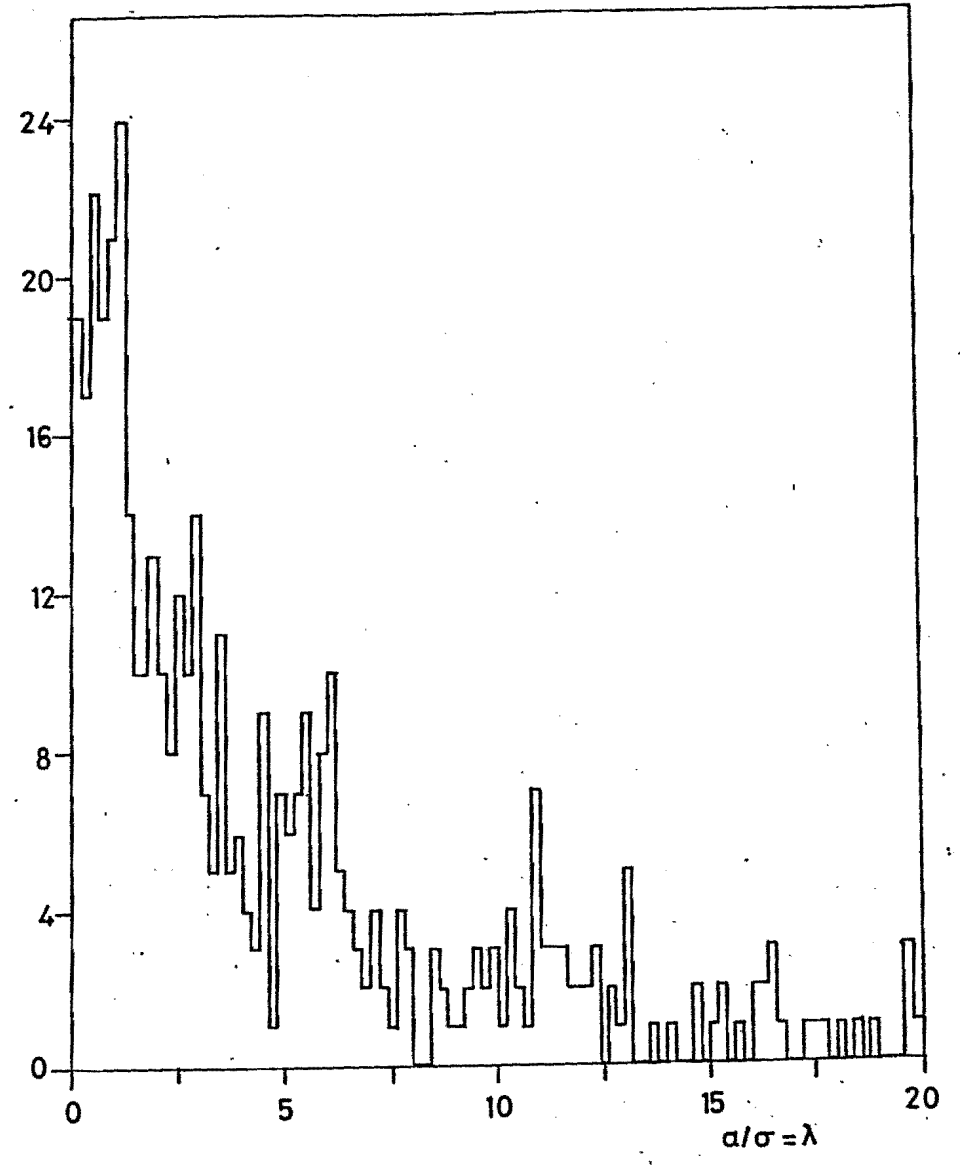


Fig.16

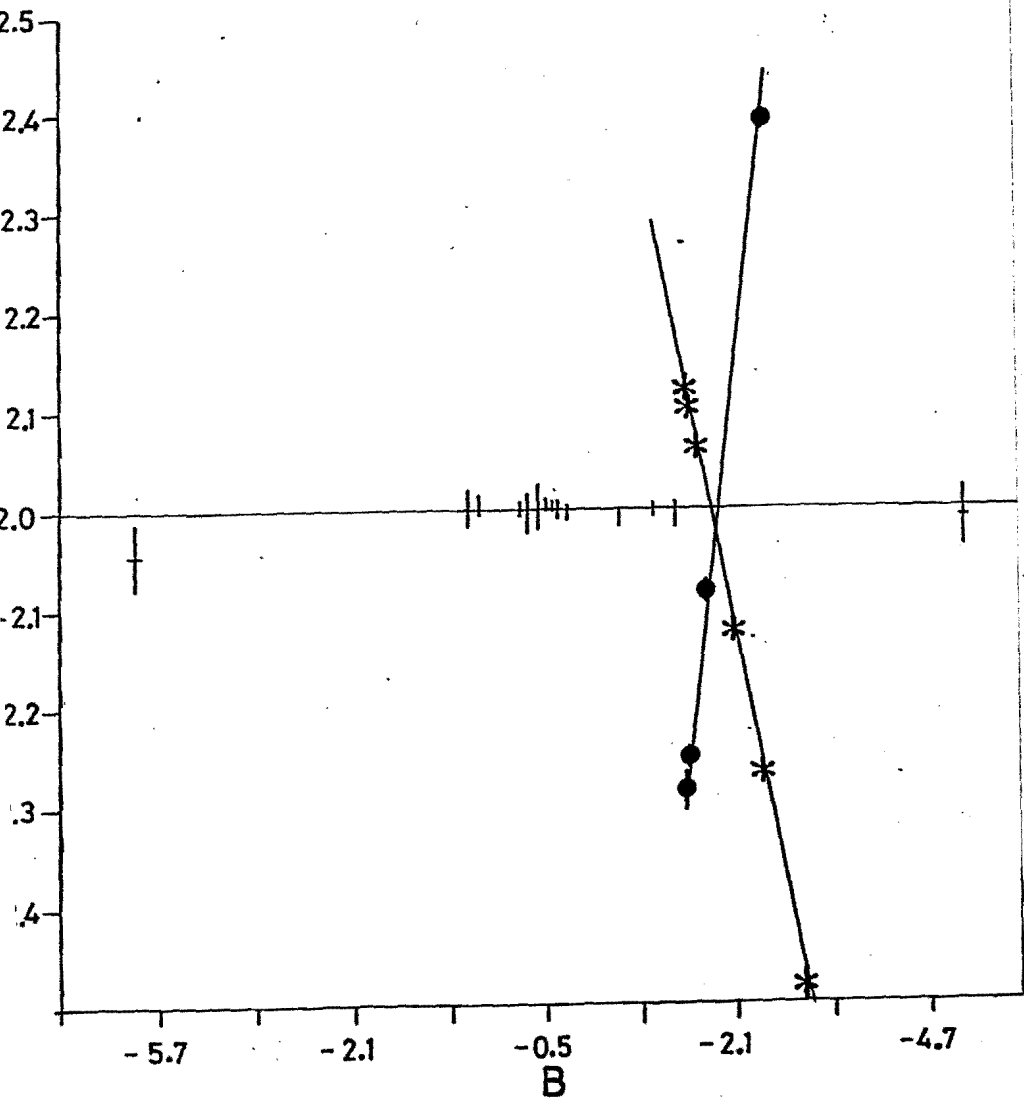


Fig.17

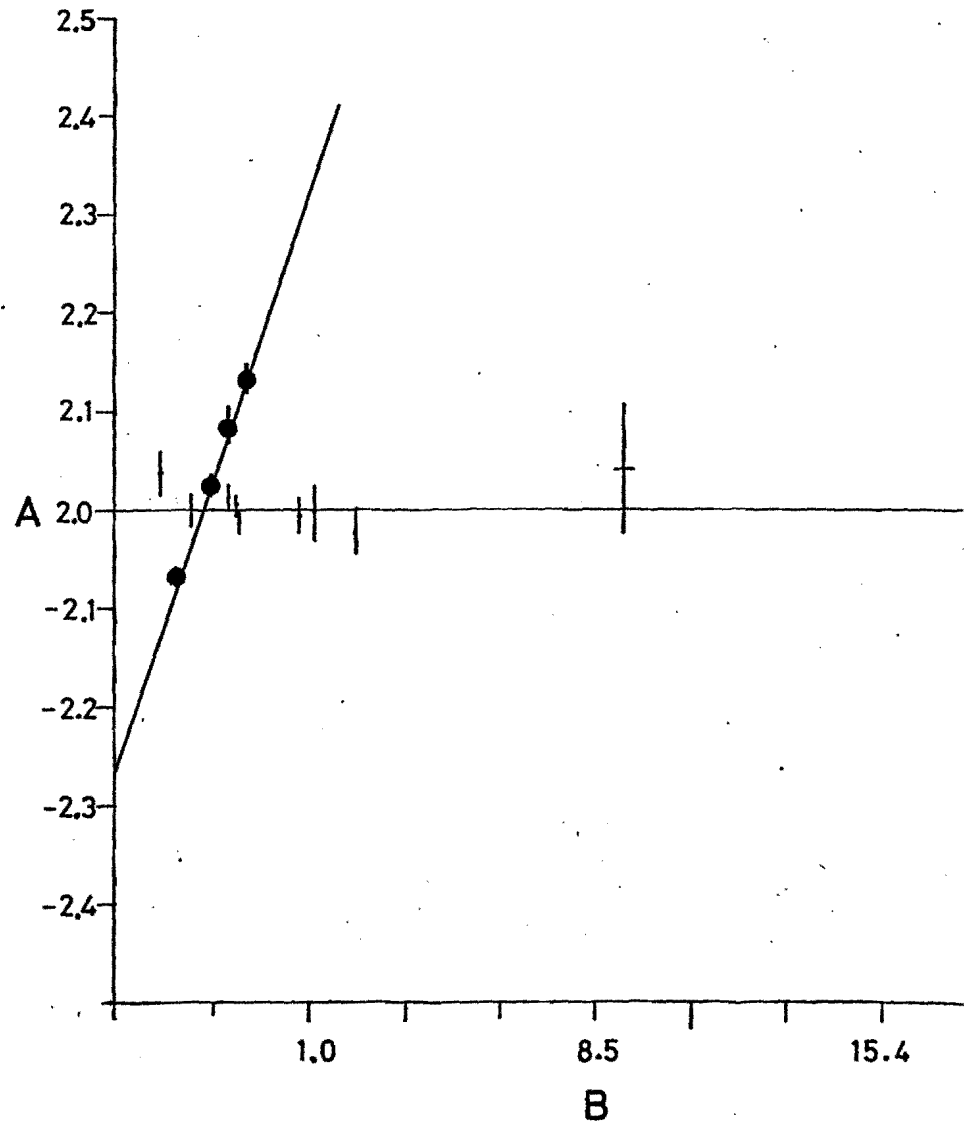


Fig.18

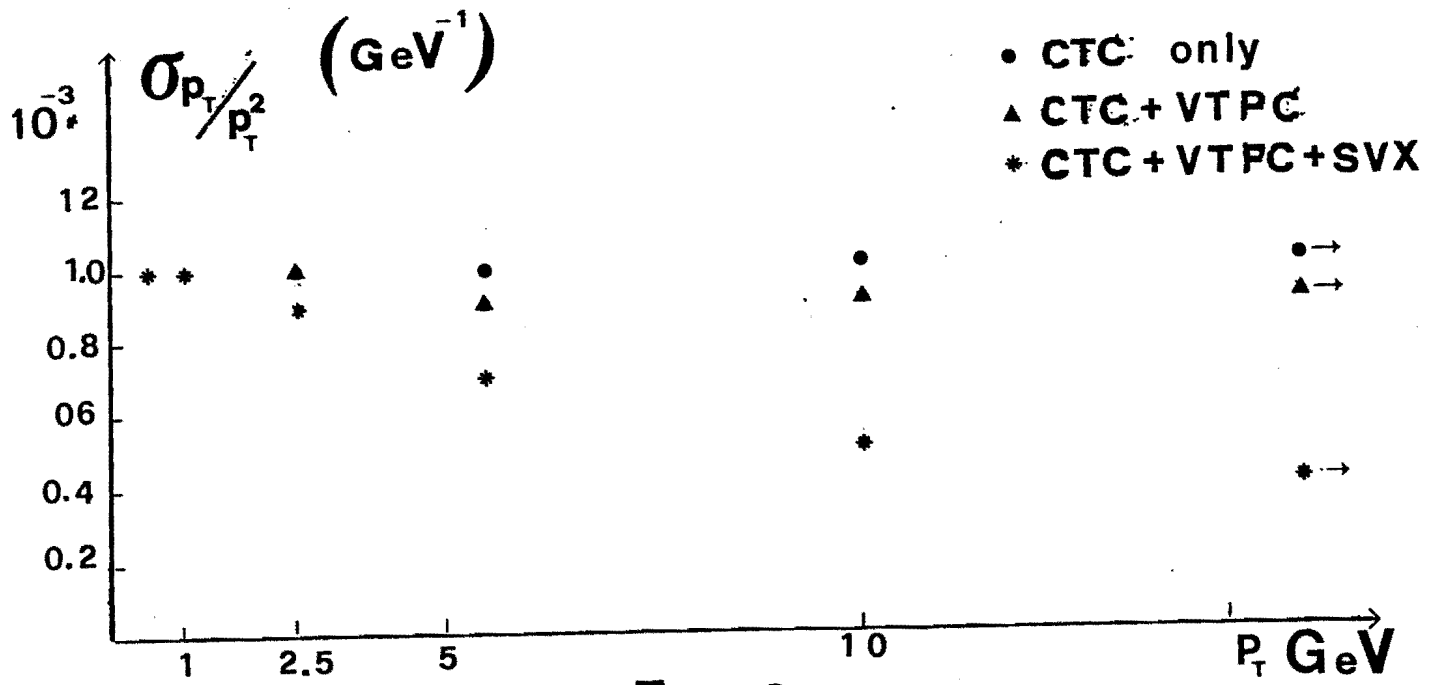


Fig 19

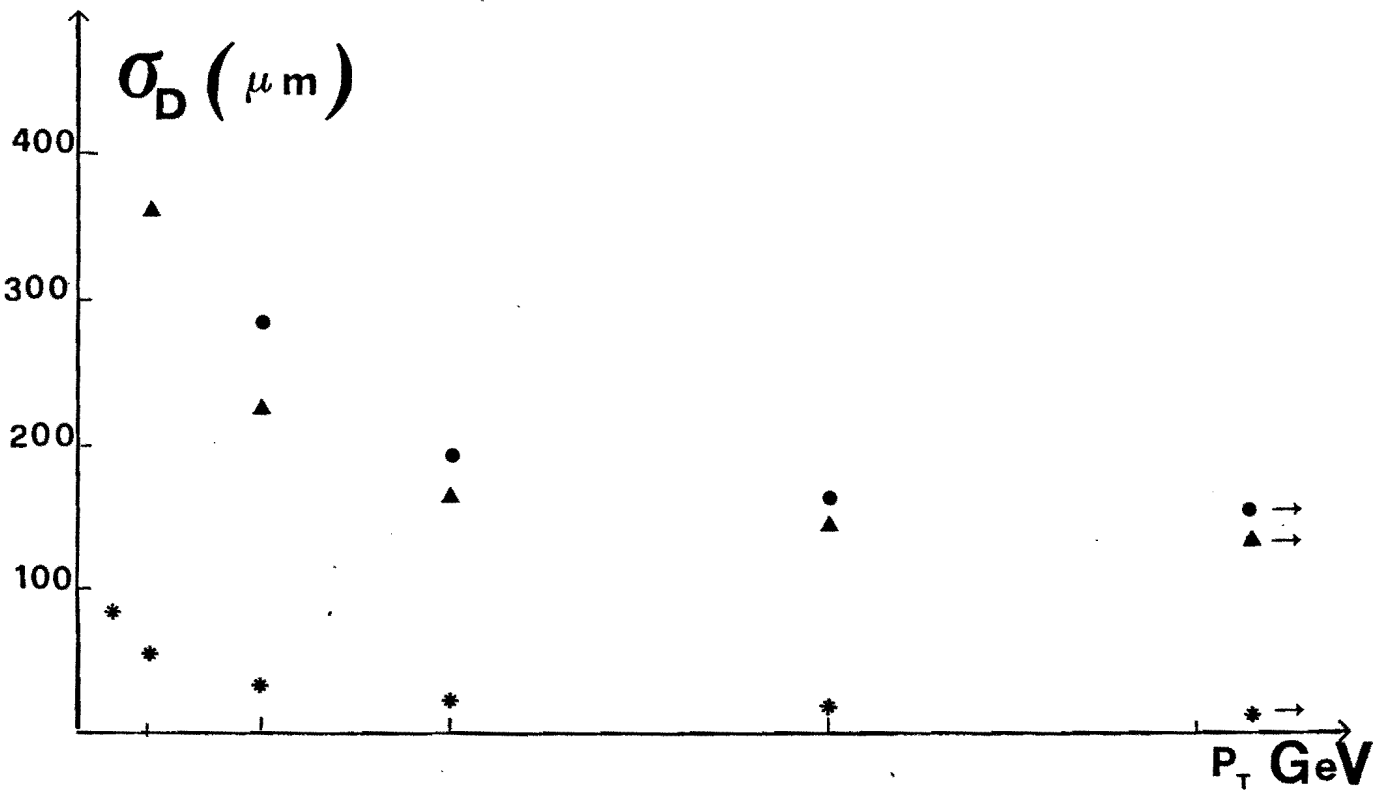


Fig 20

CHAPTER VI

SHARPENING UP THE W--T+B SIGNAL

In order to assess the capability of SVX to perform useful physics by tagging beauty particles one needs to show that not only the method would preserve the signal (as proved in the previous Chapter) but would also improve the signal/background ratio. To understand how and to what extent this can be made we have chosen a specific problem: would the method allow to discover a peak in the jet-jet mass distribution by tagging $W \rightarrow tb \rightarrow$ jet-jet, while this peak would not be visible in the inclusive M_{jj} spectrum? Furthermore we estimated the efficiency in tagging events where a Higgs boson is produced in association with heavy flavours.

VI.1 Vertex finding efficiency

The programs described in Chapt.V were used to compute the tagging efficiencies of a number of different channels as a function of the number of required reconstructed tracks per vertex. We analyzed several processes which produce secondary vertices, i.e. $W \rightarrow t+b$, $W \rightarrow c+s$, parton-parton $\rightarrow b\bar{b}$, $c\bar{c}$, and also a large sample of parton-parton \rightarrow light jets (u,d,s,glue) -which are the dominant contribution to the di-jet cross section. The events were simulated selecting jets with $15 < P_T < 50$ GeV and $|\eta| < 2$. The results are shown in Tab. 1 where, for each process, the fraction of events with at least 1 reconstructed secondary vertex, having multiplicity of at least 3 (4) identified charged prongs, is given. It should be stressed that these efficiencies represent the overall efficiency of the reconstruction program after properly allowing for the various decay channels of all unstable particles (as done by ISAJET) and using the complete simulation package of CDF.

Events in which the heavy mesons decay with a final number of charged tracks less than three cannot be reconstructed. For comparison in Table 2 this unavoidable effect was removed. On comparing Table 2 with Table 1, one can estimate with which efficiency the SVX is able to tag the events that can possibly be tagged. One sees that the efficiency for B mesons is higher than for charmed particles by a factor of about 11, consistent with what discussed in

Chapt.V.

In Tab. 1 a difference by a few % is seen between the efficiencies for tagging QCD $b\bar{b}$ jets and $W \rightarrow tb$ jets. This effect is due to the different P_T spectrum in the two processes. The applied cut $P_T > 15$ GeV gives an inclusive sample with $\langle P_T \rangle \sim 20$ GeV, while the P_T spectrum of jets originating from W is peaked at $\sim M_W/2$. Thus heavy mesons from $W \rightarrow tb$ in average have higher momentum than in the accepted QCD jets, and their decay prongs will be closer to each other reducing the overall reconstruction efficiency of secondary vertices. Work is in progress to estimate the effect of a harder P_T cut.

In Tab. 3 we give the fraction of light jets (u,d,s,glue) with at least one reconstructed secondary vertex. In row 1 beauty particles produced in the fragmentation process of these jets were removed. The detected vertices are therefore due to errors or decays of (mostly) K^0 's and Λ 's. The second row shows that ϵ_4 would give a rejection of ~ 250 against light jets. However, by studying the events we discovered that the residual efficiency of light jets is nearly all due to beauty particles produced in the fragmentation process. The light jets are mostly gluons. ISAJET might overestimate or underestimate their beauty content, since experimental information is lacking and perturbative QCD cannot be applied in this case. Whatever this beauty content in gluon fragmentation might be, the beauty particles would be soft and this difference can be exploited, as one can exploit in general all differences between the overall topology of beauty and light jets. In view of these uncertainties and hopes, we will adopt the efficiency quoted in row 1 of Tab.3 in the considerations that follow.

Requesting three or more tracks per vertex, the numbers of Table 1 and 3 indicate that the $W \rightarrow tb$ process can be tagged with $\epsilon_3 \sim 30\%$ and a rejection against light dijets by $30/.55 \approx 55$. Using ϵ_4 , these numbers become $\sim 17\%$ and $17/.05 \approx 340$ respectively. An inspection of the tables shows that inclusive production of beauty jets (tt would be practically the same) can be tagged with approximately the same quality factors. One understands that ultimately the problem might be whether in the M_{jj} distribution a $W \rightarrow tb$ peak can be sorted out over a background dominated by $b\bar{b}$

(and $t\bar{t}$) QCD dijets.

To study this problem we needed a large statistics both for the signal and for the background processes. Since it was unpractical and unnecessary to run that many events through the full CDF Monte Carlo package, a simpler method of jet smearing was adopted, as we explain in the following section.

VI.2 Expected Mjj distributions

The p_T and Y distributions of QCD jets and of jets from W decay were first studied in order to attribute suitable cuts to the generator. One sees in fig.1 that jets from W decay are produced mainly in the central region. We chose a cut $|Y| < 2$ which retains most of the signal. We also took $p_T > 15$ GeV, which affects very little the signal (fig 2). We note, however, that this cut is probably not the best one to reduce the background (see for example the study of Horgan and Jacob, II, 9). It appears that a higher $p_{T,j}$ cut could be applied without affecting appreciably the signal while improving the signal/background ratio. As already mentioned, this problem is at the present under study.

We divided the dijet background into light jets (u, d, s, g), charm ($c\bar{c}$) and heavy flavour $b\bar{b}$ ($t\bar{t}$ is a small addition which we did not take into account), and generated with ISAJET 10,000 events of each type in the range $15 < p_T < 80$ GeV, $|Y| < 2$. An additional set of 10,000 events were generated for $80 < p_T < 200$ GeV. To generate realistic Mjj distributions, we used a simple parametrization to smear the jet. The energy of each particle in the jet is smeared according to $\sigma(E) = .55 \cdot E^{1/2}$, an average resolution for the combined E.M.-Hadronic CDF calorimeters. No other effect causing imperfect clustering was accounted for. Under these simplifying but adequate assumptions, we obtained a resolution in invariant mass (see fig 3) close to what had already been found in more detailed simulation studies of CDF response to jets (IV, 4).

Each set of generated data was then weighted with its own cross section and multiplied by the appropriate SVX efficiency factor to simulate the final data. To improve rejection against accidentals and errors, we decided to

require at least four reconstructed prongs for each accepted vertex. Accordingly the efficiencies were as follows:

0.05	% for glue,u,d,s jets
22.4	% for $b\bar{b}$ jets
00.4	% for $c\bar{c}$ jets
16.8	% for $W \rightarrow tb$
00.1	% for $W \rightarrow cs$

The total data collected with an integrated luminosity of $L_1 = \int Ldt = 10^{36} \text{ cm}^{-2}$ and of $L_2 = \int Ldt = 10^{37} \text{ cm}^{-2}$ was calculated. The properly normalized Mjj spectra from the various contributions are shown in fig 4 and 5.

A search for a W signal was done by fitting the data in the region $M_{jj} < 70$ and $M_{jj} > 90$ GeV with the function $f(x) = \exp(a+bx+cx^2+dx+ex^4)$

The fitted curve was then subtracted from the total data, giving the residuals shown in fig 6 where the fit with a gaussian is also shown.

A small signal is seen in the unbiased data (no SVX), again a small signal with the L_1 data (fig b) and a nice signal is seen in the L_2 data (fig c).

We take as a figure of merit:

$$\lambda = \frac{A_S - A_B}{\sigma_D}$$

where A_S = integrated signal, A_B = integrated background in the signal region, σ_D = standard error in $A_S - A_B$.

Different values of λ are shown in Tab.4 for various choices of ϵ_e , the rejection factor against light jets. Fig 6,b correspond to $\epsilon_e = 5 \cdot 10^{-4}$. Fig 7 corresponds to $\epsilon_e = 10^{-4}$. This figure is of interest as an estimate of the ultimate situation that might be reached if the use additional rejection factors (coming from a more favourable choice of kinematical ranges, from cuts on event topology, etc.) would kill the light jet background completely. One sees in fig 6,b that the information from the SVX alone, although slightly improving λ (see Tab.4), would not be sufficient to generate a significant Mjj peak in a nominal CDF year run ($L_1 = 10^{36} \text{ cm}^{-2}$). However, if the luminosity could be increased up to L the statistical significance of the peak would increase to $\sim 8 \lambda$, fig.6,c.

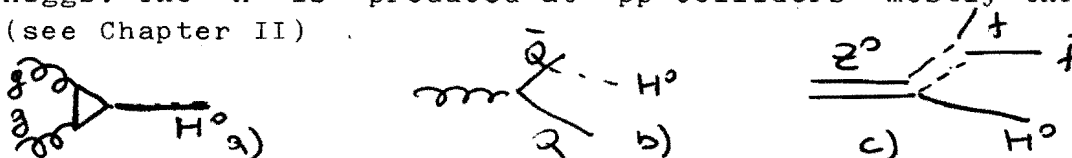
Conversely, one understands that the search for a peak due to a new particle decaying into two heavy flavours and invisible in the inclusive Mjj distributions for a given integrated luminosity, could be successful in the SVX tagged

distribution provided the initial background/signal ratio is more favourable than in the adopted example $W \rightarrow tb$. The merits of the method stand solidly on the large factor by which the light quark background is reduced, and by its efficient selection of a heavy quark pair sample. We therefore conclude that our preliminary study of $W \rightarrow t+b$ tagging indicates the feasibility of a search for new heavy particles based on tagging of secondary vertices.

One understands that the possibility to tag special events depends on the total number of heavy quarks in the event. More favourable cases are those in which more than two beauty particles are produced. We discuss one such case in the next Section.

VI.3 Searching for the Higgs Boson

It has been already observed (II,1.4) that a tag of heavy mesons could be decisive in the search for the neutral Higgs. The H is produced at pp colliders mostly through (see Chapter II)



where $Q\bar{Q}$ is a heavy quark pair and f is a fermion. Thus, if f is a b quark, in both diagrams b) and c) the Higgs boson is produced in association with two heavy quarks. Moreover, if $M_H > 2 m_b$, another pair of heavy quarks is present in most final states and thus typically four secondary vertices are produced close to the interaction region. Other processes could also give a similar topology, for example the production of a pair of superheavy quarks (see II.2.1) or of a pair of technipions (II.2.2). A technipion would decay into a fermion pair with a width proportional to the squared fermion mass, and thus most of the times it would decay into the heaviest fermion pair allowed. However, these processes are equally important to discover as the Higgs is.

It is straightforward to tag these processes by the reconstruction of at least two (out of four) of the existing secondary vertices. We give in Tab.5 the efficiencies to reconstruct one or more vertices in events where 2,3,4 vertices are generated.

In front of a rather small fraction of $b\bar{b}$ events with two fully reconstructed vertices and of the enormous rejection factor ($\sim 3 \cdot 10^{-4}$) for light jet events, a considerable fraction ($\sim 18\%$) of events with 4 generated vertices is expected to have at least two reconstructed vertices. Given the relatively large Higgs production cross section (Chapter II.4) we thus believe that one can seriously hope to be able to tag the Higgs particle by studying the four jet sample and requiring two secondary vertices.

We wish that this would be just one of the great discoveries of CDF.

TABLE 1

	ϵ_3	ϵ_4
$W \rightarrow tb$	31.5	16.8
$W \rightarrow cs$	2.	
QCD $b\bar{b}$ jets	35.2	22.4
QCD $c\bar{c}$ jets	1.6	

ϵ_3 = fraction of events with at least
three tracks per reconstructed vertex

ϵ_4 = fractions of events with at least
four tracks per reconstructed vertex

TABLE 2

	ϵ_3
QCD $b\bar{b}$ jets	42.2
QCD $c\bar{c}$ jets	3.6

N.B. Only SVX inefficiencies are accounted for .

TABLE 3

	ϵ_3	ϵ_4
B subtracted	.55	.05
B included	1.1	.4

Fraction of light jet events tagged by a secondary vertex .

TABLE 4

ϵ_4	λ_1	λ_2
$5 \cdot 10^{-4}$	1.5 σ	8 σ
10^{-4}	2.8 σ	12 σ

$$\lambda = \frac{A_S - A_B}{\sqrt{A_S + A_B}}$$

$$\lambda_1 \Rightarrow L_1 = 10^{36-2} \text{ cm}$$

$$\lambda_2 \Rightarrow L_2 = 10^{37-2} \text{ cm}$$

TABLE 5

		$n_{\text{reconstructed}}$				
		0	1	2	3	4
$n_{\text{generated}}$	2	64.8	31.4	3.8		
	3	52	38.	9.2	.8	
	4	42	41.	15.	1.8	2

Fraction of events reconstructed in multi-vertices events

(at least three reconstructed tracks per vertex).

FIGURE CAPTIONS (Chap. 6)

- 1) Rapidity distribution of jets from W decay.
- 2) P_T distribution of jets from W decay.
- 3) Mass resolution obtained with our parametrization:
r.m.s. $\sim .07 \cdot M$.
- 4) $d\sigma/dM_{jj}$ for a one year run ($\int L dt = 10^{36} \text{ cm}^{-2}$).
Various contributions (light jets, $c\bar{c}$, $b\bar{b}$, W jets)
are shown separately.
- 5) Same as above for an integrated luminosity of $L_2 = 10^{37} \text{ cm}^{-2}$.
- 6,a) Two jet mass distribution obtained in absence of
the SVX after one year of running (L_1). A hardly
appreciable ($\lambda \sim 1$) $W \rightarrow jj$ signal is obtained.
- 6,b) Two jet mass distribution obtained with the SVX having
a rejection efficiency of $5 \cdot 10^{-4}$ against light jets.
- 6,c) The same as in b), but for $\int L dt = 10^{37} \text{ cm}^{-2}$.
- 7) $W \rightarrow tb$ signal with a SVX having a 10^{-4} rejection
power against light jets, for L_1
(upper figure) and L_2 (lower).

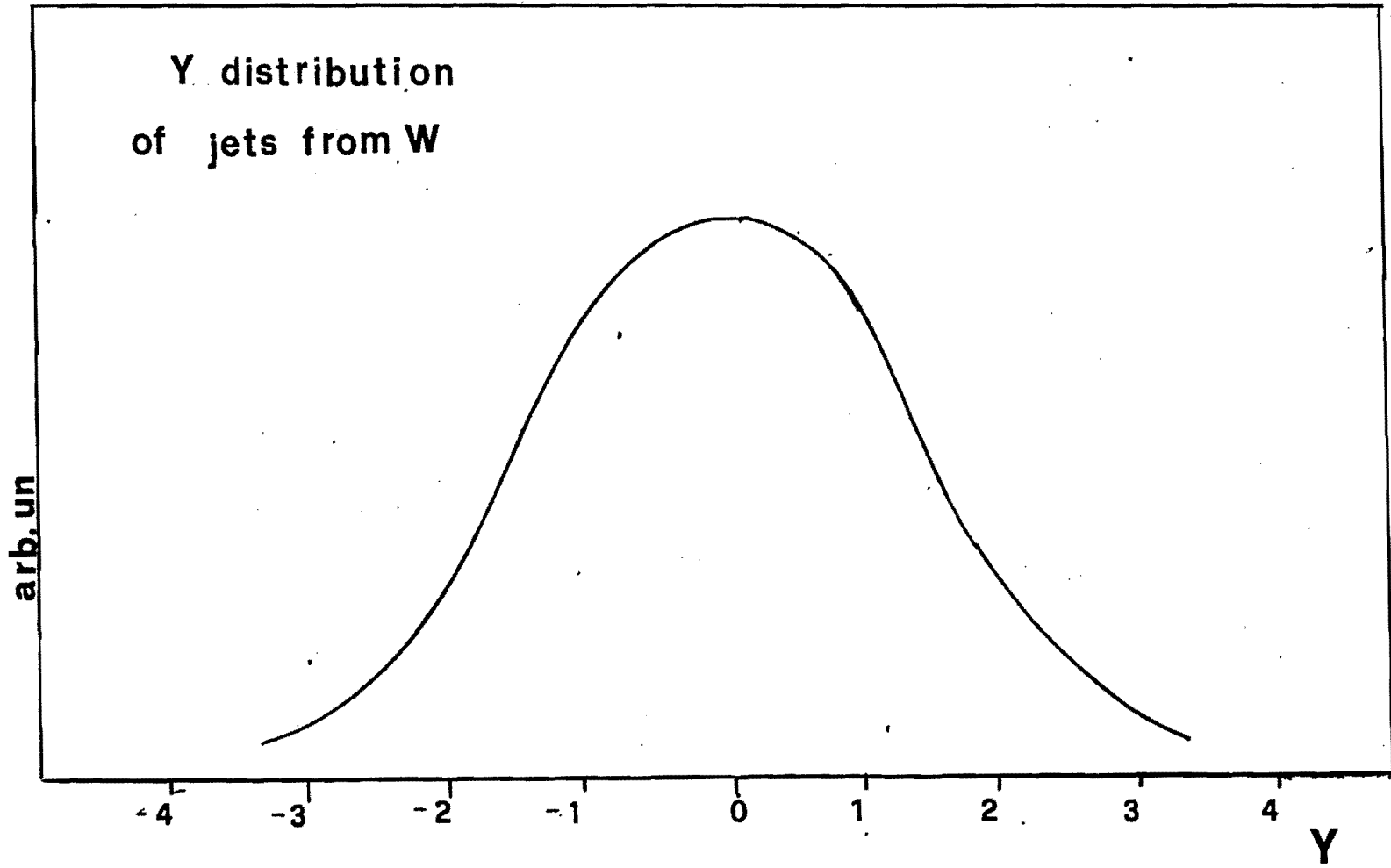


Fig.1

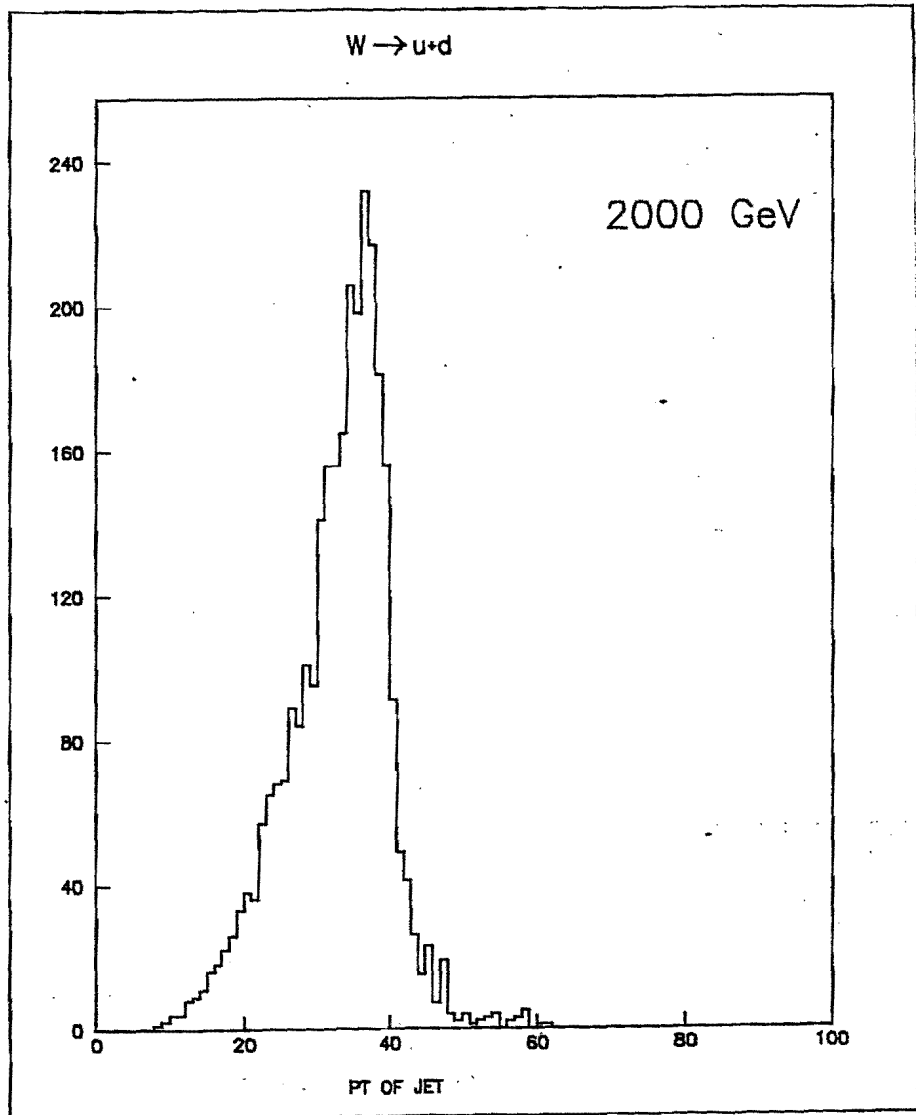


Fig 2

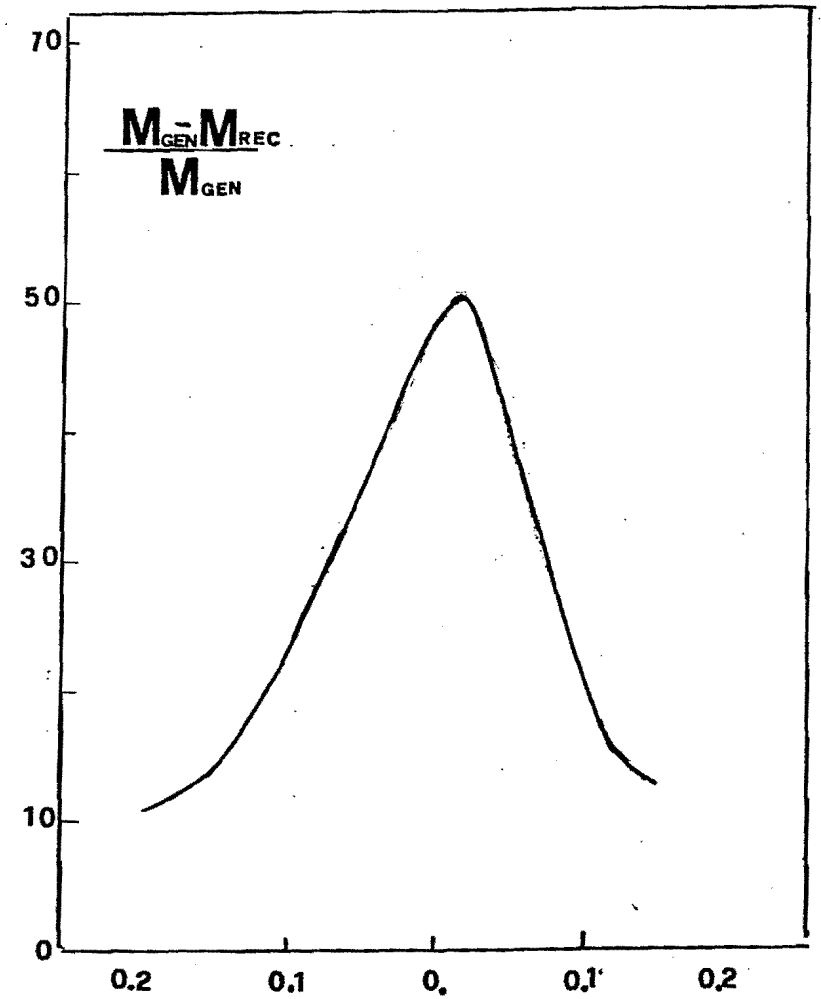


Fig 3

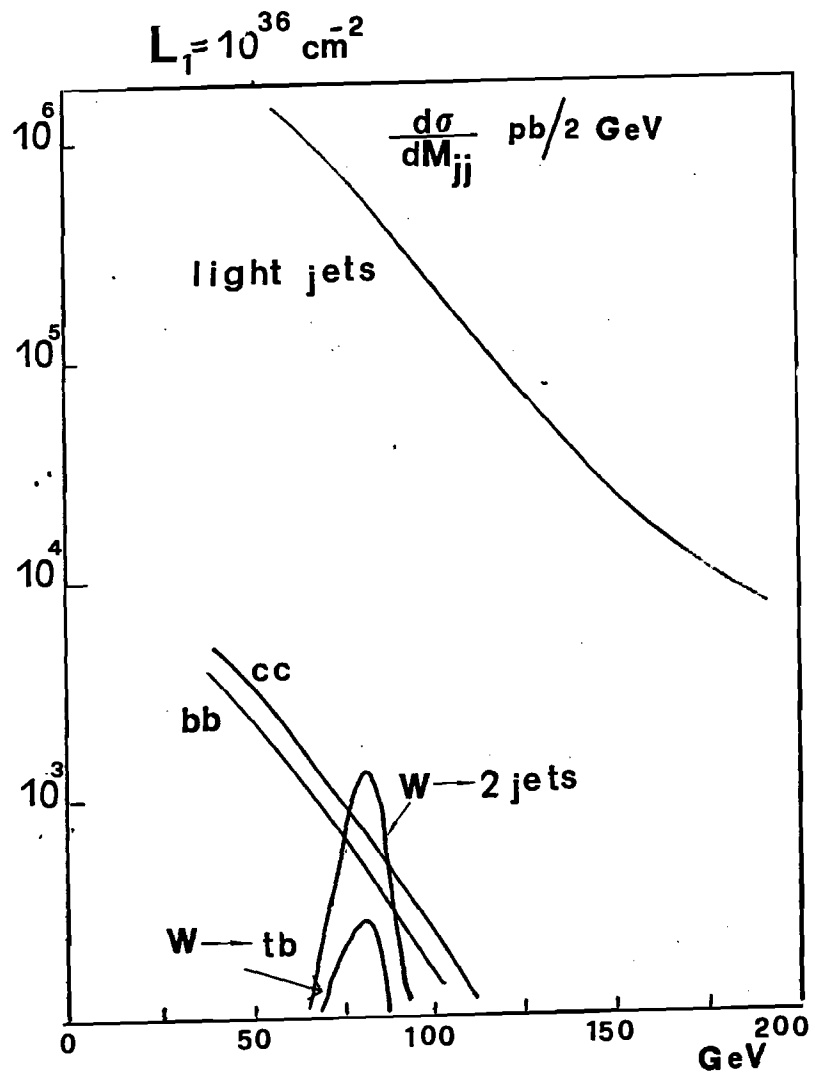


Fig 4

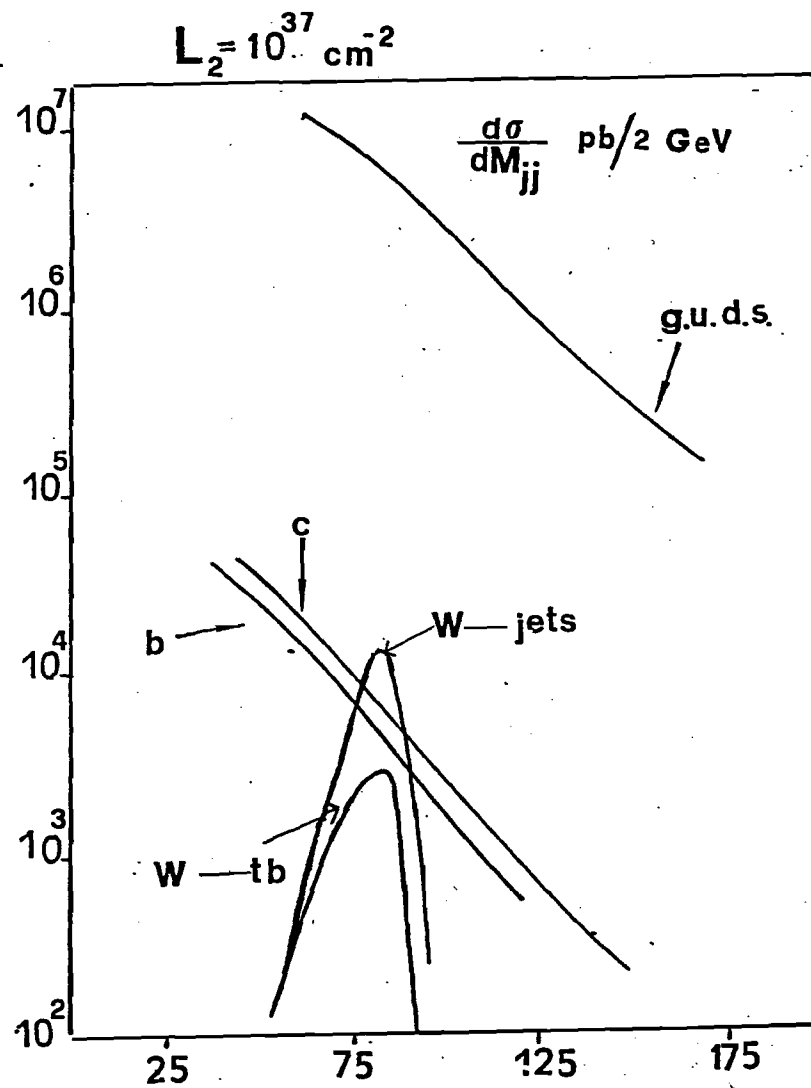
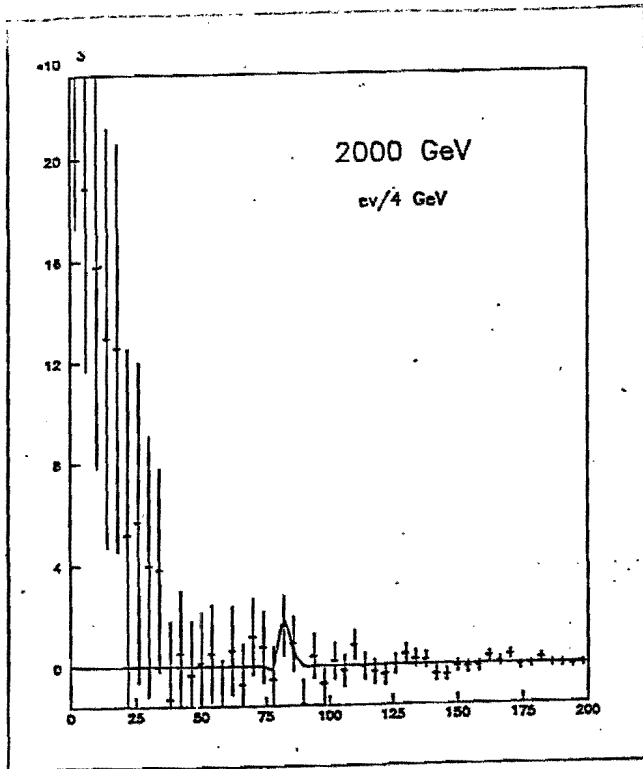
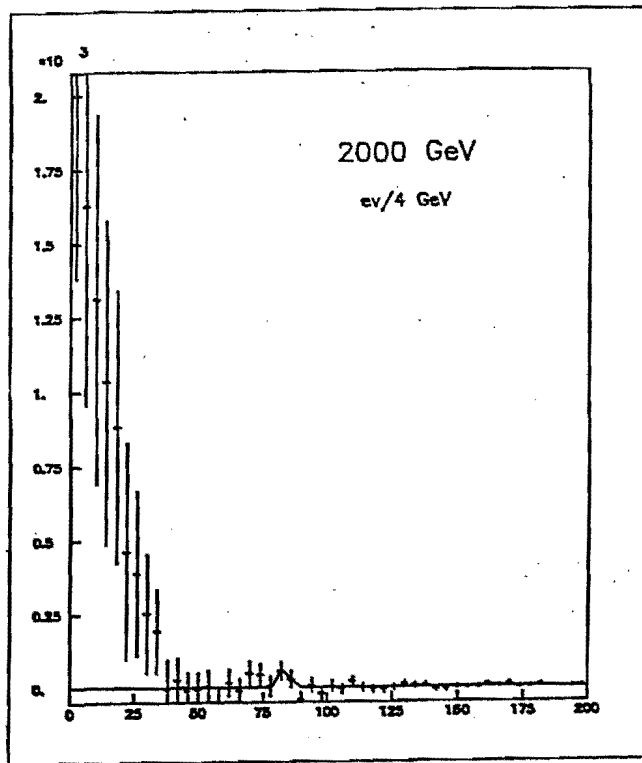


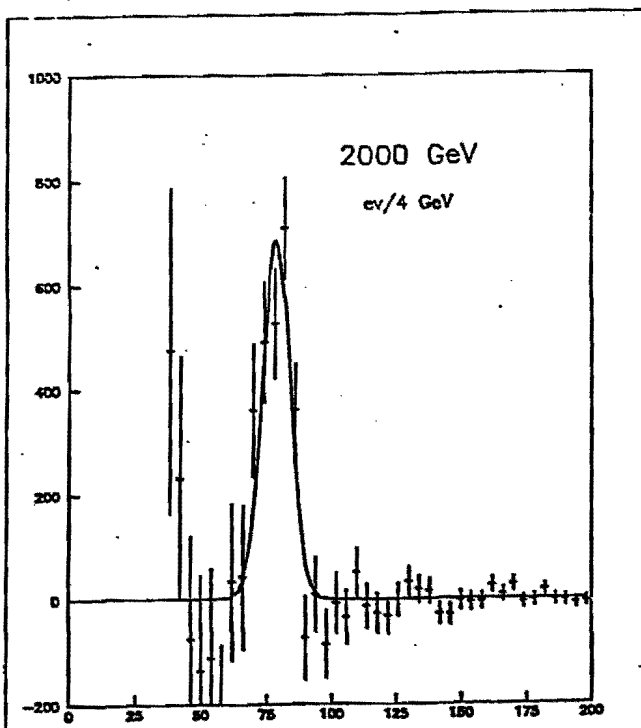
Fig 5



a)



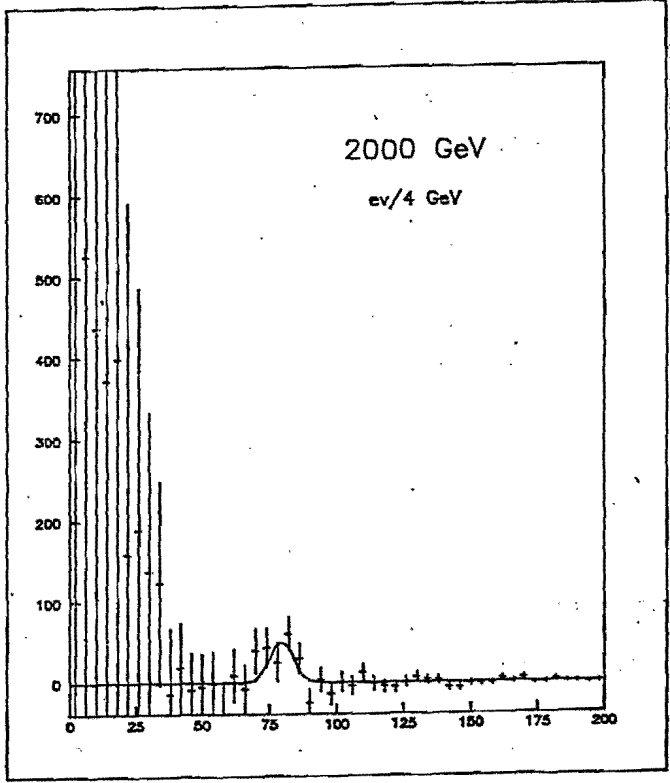
b)



c)

Fig 6

a)
 L_1



b)
 L_2

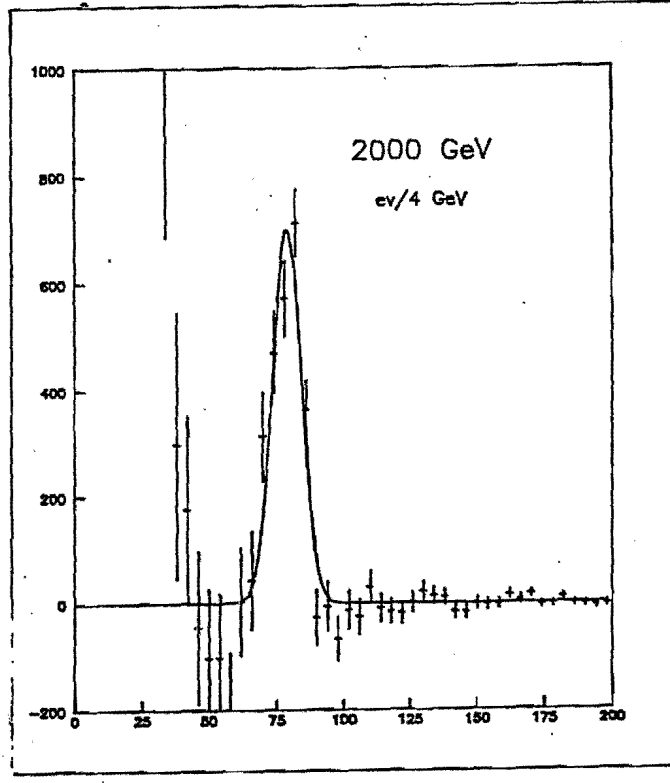


Fig 7

CHAPTER I

- 1) The Fermilab Antiproton Source, Fermilab 1982

CHAPTER II

- 1) R.Horgan, M.Jacob, Nucl.Phys B179, 441 (1981)
- 2) Abolins et al., Proceedings Snowmass Conference Fermilab, 1982
B.Humpert, Phys.Lett. 140B, 105 (1984)
- 3) M.Jacob, CERN-Th.-3515/83
M.Jacob, CERN-Th.-3693/83
M.Jacob, CERN-Th-3953/84
- 4) UA2 Collaboration, talks given at V Workshop on pp Collisions, St.Vincent, March 1985
- 5) G.Altarelli et al., Fermilab-Pub- 84/107-T
G.Altarelli et al., CERN-Th-3851/84
C.Quigg, Rev.Mod.Phys. 49, 297 (1977)
- 6) G.Arnison et al., Phys.Lett. 122B, 103 (1983)
M.Banner et al., Phys.Lett. 122B, 476 (1983)
G.Arnison et al., Phys.Lett 126B, 398 (1983)
P.Bagnaia et al., Phys.Lett. 129B, 130 (1983)
- 7) G.Altarelli, CERN-Th-3983/84
- 8) Gordon et al., Proceedings Snowmass Conference,
- 9) Kane, Proceedings of Aspen Winter Physics Conference series, January 1985
R.Horgan, M.Jacob, CERN-Th-3682/83
T.Rizzo, Phys.Rev. D 20, 706 (1979)
T.Rizzo, Phys.Rev. D 20, 713 (1979)
- 10) V.Barger et al., Phys.Rev. D 24, 1428 (1981)
V.Barger et al., Phys.Rev. D 25, 112 (1982)
R.Horgan, M.Jacob, CERN-Th-3164/81
- 11) Pakvasa et al., Phys.Rev. D 24, 1428 (1981)
V.Barger et al., Phys.Lett. 125B, 343 (1983)
Hagiwara, Long, Phys.Lett. 132B, 202 (1983)
V.Barger et al., Phys.Lett. 129B, 341 (1983)
V.Barger et al., Phys.Rev. D 29, 1923 (1984)
- 12) V.Barger, R.Martin, CERN-Th-3972/84
V.Barger et al., Phys.Rev. D 29, 887 (1984)
- 13) V.Barger, MAD/PH/201
- 14) G.Arnison et al., Phys.Lett. 147B, 493 (1984)
- 15) J.Ellis et al., Nucl.Phys. B106, 292 (1976)
- 16) Georgi et al., Phys.Rev.Lett. 40, 692 (1978)

- 17) Gordon et al., Proceedings of Snowmass Conference,
- 18) J.N.Ng, P.Zakarauskas Phys.Rev. D 29,876 (1984)
- 19) S.L.Glashow et al., Phys.Rev. D 18,1724 (1978)
Finjord et al., Phys.Lett. 89B,99 (1979)
V.Barger et al., Phys.Lett. 120B,323 (1982)
- 20) C.Quigg, Fermilab-CONF-84/88-t
H.Harari in Proceedings of the Heisenberg Symposium,
Heidelberg 1981
M.K.Gaillard, ibidem
R.D. Peccei, MPI-PAE/pth/70/84
- 21) R.D. Peccei, DESY-84-096
H.Baer et al., CERN-Th-4059/84
A.Rohlf, UA1 Collaboration CERN-EP/84-126
C.Rubbia in Proceedings of Bern Conference on pp
Collisions, CERN 84-09
- 22) V Workshop on pp Collisions, St.Vincent, March 1985
- 23) P. Schacht, MPI-PAE/Exp.E1-139
- 24) F.Halzen, F.Herzog, MAD/Ph/195
- 25) Barger et al., Phys.Rev. D 30,947 (1984)
- 26) T.Rizzo, Phys. Rev. D 20,706 (1979)
- 27) Ellis, Predazzi Introduction to gauge theory, London 1982
- 28) V.Barger et al., Phys.Lett. 133B,449 (1983)
- 29) C.Rubbia and D.Cline, CERN-EP-83/61
- 30) P.Aurenche and R.Kinnunen, Lapp.-Th-108
- 31) V.Barger et al., Phys.Rev. D 29,2020 (1984)
P.Aurenche and R.Kinnunen, Lapp.-th-104
- 32) G.Altarelli, La Rivista del Nuovo Cimento, 3, 1984
M.E. Peskin in Proceedings of Snowmass Conference,
Fermilab, 1982
- 33) S.Weinberg, Phys.Rev.D 19,1277
Susskind, Phys.Rev. D 20,3404
- 34) Fahri and Susskind, Phys.Rev. D 20,3404
- 35) Kane in Proceedings of Snowmass Conference,
Fermilab, 1982
- 36) M.E.Peskin, cit.
- 37) G.Altarelli, La Rivista del Nuovo Cimento, 3 (1984)
- 38) Eichten et al., Rev. Mod. Phys. 56,579 (1984)
- 39) C.Baltay and M.Gordon, Proceedings of Snowmass
Conference, Fermilab 1982
- 40) Nanopoulos, CERN-Th.3995/84
K.Lane, Proceedings of Snowmass Conference
Fermilab, 1982

- 41) A.De Rujula et al., Phys.Lett. 140B,253 (1984)
- 42) K.Enqvist et al., Phys.Lett. 135B,329 (1984)
G.Pancheri LNF-84/33(P)
- 43) C.H.Llewellyn Smith,Phys.Rep. 105,53 (1984)
- 44) C.H.Llewellyn Smith ,cit.
- 45) A.Savoy Navarro,Phys.Rep. 105,91 (1984)
- 46) J.Ellis,H.Kowalski, DESY 84-045
- 47) M.Mangano, CERN-Th.3717/83
R.Barbieri et al.,Phys. Lett. 127B,458 (1983)
- 48) A.Savoy Navarro ,cit.

CHAPTER III

- 1) S.Miozzi, University of Roma Thesis, May 1985
- 2) G.Blocker et al., CDF 271
- 3) M.Atac et al., CDF 178
- 4) M.Atac et al., CDF 231
- 5) M.Dell'Orso and J.Freeman, CDF 255
- 6) M.Atac and G.Chiarelli, CDF 193
- 7) H.Fritsch, CDF 242
- 8) S.Majewski , Workshop on Vertex Detectors, FNAL 1984
- 9) B.Sadoulet, Proceedings of SLAC workshop on
instrumentation for colliding beam experiment
SLAC 1982.
- 10) M.Lutz, Workshop on Vertex Detector, FNAL 1984
- 11) D.Buchol, Workshop on Vertex Detectors, FNAL 1984
- 12) S.R. Amendolia et al., presented at the Third
European Symposium on Semiconductors Detectors,
Munich,1983
- 13) S.Bertolucci et al., CDF 285
- 14) G.Bellettini, Proceedings of the Aspen
Winter Physics Conference series,January 1985

CHAPTER IV

- 1) G.Blocker et al.,CDF 271
- 2) M.Atac et al., CDF 178
- 3) M.Atac et al., CDF 231
- 4) M.Dell'Orso,J.Freeman, CDF 255
- 5) M.Atac and G.Chiarelli, CDF 193
- 6) H.Fritsch , CDF 242
- 7) S.Majewski,Workshop on Vertex Detectors,FNAL 1984
- 8) B.Sadoulet ,Proceedings of SLAC workshop on
instrumentation for colliding beam experiment
SLAC 1982
- 9) M.Lutz , Workshop on Vertex Detector,FNAL 1984

- 11) S.R. Amendolia et al., presented at the Third European Symposium on Semiconductors Detectors, Munich, 1983
- 12) S. Bertolucci et. al, CDF 278
G. Belleltini, Proceedings of the Aspen Winter Physics Conference series, January 1985

CHAPTER IV

- 1) Design Report of CDF, Fermilab August 1981
- 2) U. Bottigli, private comm.
- 3) J. Yoh, CDF 179
- 4) J. Freeman et al., CDF 225
- 6) J. Freeman, invited talk at IV Workshop on pp Collisions, Bern, March 1984
- 5) S. Tarem, CDF 200

CHAPTER V

- 1) P. Avery et al., Phys Rev. Lett. 51, 1139 (1983)
H. Albrecht CLEO Collaboration, DESY 84-073
TASSO Collaboration, DESY 83-114
- 2) DELCO Collaboration as quoted in M. Jacob, CERN-Th-3953/84
- 3) TASSO Collaboration, as quoted in G. Wolf, SLAC-PUB-3446
- 4) R. Frey UA1 Collaboration, Proceedings of the IV workshop on pp collisions, Bern March 1984
- 5) F. Bedeschi, G. Chiarelli, CDF 284